NTNU

Norwegian University of
Science and Technology

Isogeometric Analysis of Thermo-Hydro-Mechanically Coupled Processes in Soil

Daniel Ryghseter

Civil and Environmental Engineering
Submission date: June 2016
Supervisor: Steinar Nordal, BAT
Co-supervisor: Yared Bekele, BAT

Norwegian University of Science and Technology
Department of Civil and Transport Engineering

NORWEGIAN UNIVERSITY OF SCIENCE AND TECHNOLOGY
DEPARTMENT OF CIVIL AND TRANSPORT ENGINEERING

Report Title:	Date: 09/06-2016			
Isogeometric Analysis of Thermo-Hydro-Mechanically Coupled Processes in Soil	Number of pages (incl. appendices): 134			
	Master Thesis	x	Project Work	

Name:
Daniel Ryghseter

Professor in charge/supervisor:
Professor Steinar Nordal, NTNU

Other contacts/supervisors:
PhD Yared W. Bekele, NTNU

Abstract:

This thesis conducts numerical studies with two THM (Thermo-Hyrdo-Mechanical) models with isogeometric elements. One is for fully saturated porous media, and the other is for ground freezing. Both are developed at NTNU.

The first model is used to investigate the performance of isogeometric analysis with discontinuities, where conventional analysis often fall short. Without any alteration, the isogeometric analysis has been found to give similar results as the modified conventional finite element analysis for the problems investigated.

The second model is used to investigate the possibilities and problems related to modeling of frost heave for transportation/infrastructure projects. As the model is brand new, preliminary work was necessary. A parametric study was carried out to investigate the different parameters effect on the solution. A laboratory test was attempted to be recreated, and a small scale simulation with seasonal temperature variations was conducted. Finally the model was used in an attempt to back calculate two railroad sections damaged by frost heave. The results of the parametric study has given a clear indication towards which parameters are the most important in the model. The simulations of seasonal temperature variation, clearly show how the ground freezing affects the temperature profiles and surface heave. The attempts to recreate laboratory and field results only partially succeeds. Some aspects of the problems are simulated better than others, and a main contributor to this problem is assumed to be the linearly elastic material model.

Keywords:

1. Isogeometric analysis
2. THM models
3. Ground freezing
4. Disconttinuities

Daniel Ryghseter

Problem Formulation

January 15, 2016

Thermo-hydro-mechanical (THM) processes in soils couple the flow of fluid and heat with solid deformation. The interaction between these different physical processes results in a more complex behaviour of the soil. Understanding the physical processes and accurate numerical modeling of such THM coupled phenomena is essential for different applications in geomechanics. Example applications areas include geothermal energy extraction, safety assessment of nuclear waste repositories, oil and gas reservoir engineering, underground energy storage, CO_2 sequestration and ground freezing.

The current thesis work will examine the standard practice in THM numerical modeling based on literature review and relevant application areas in the industry. A commonly used approach is sequential coupling of the thermal problem with hydro-mechanical (coupled fluid flow and deformation) simulation. In reality, the heat flow, fluid flow and deformation (THM) processes occur simultaneously and the best way to solve such problems is in a fully coupled manner. The numerical modeling work will focus on fully coupled solution approaches for THM problems. Numerical simulations will be performed based on in-house developed tools and other relevant software. Some of the applications areas that may be addressed include non-isothermal consolidation problems and frost heave phenomena, such as in road construction.

Daniel Ryghseter	Steinar Nordal	Yared W. Bekele
MSc Student	Professor	PhD. Candidate

Preface

This master thesis was conducted at the geotechnical department at the Norwegian University of Science and Technology (NTNU), as part of a MSc in geotechnical engineering. This thesis is credited 30 ECTS, and span over 20 weeks in the spring semester of 2016. The thesis is related ongoing research at THM (Thermal-Hydro-Mechanical)-models at NTNU, and the problem was formulated collaboration with code author and PhD. candidate Yared W. Bekele. Yared completed his PhD in may 2016.

Trondheim, 2016-06-09

Daniel Ryghseter

Daniel Ryghseter

Acknowledgment

I want to express my gratitude to Yared Worku Bekele, PhD, for technical and professional help and guidance. He has also been a great motivator, and has always taken the time to answerer my questions. I also want to thank my supervisor Professor Steinar Nordal, for great help throughout the semester.

I also want to express my gratitude towards all the external support received during the project. A special thanks to Jean Sébastien L'Heureux at NGI for the insite in current practice and for the case studies. A general thanks to SINTEF and the IFEM staff for supplying the program prior to the release. Jernbaneverket has also kindly provided several reports and ground investigations for the case study.

D.R.

Summary and Conclusions

This thesis conducts numerical studies on THM (Thermo-Hydro-Mechanically) coupled problems, using isogeometric elements and two models created at NTNU. One model is for fully saturated porous media, and the second is expanded to represent ground freezing.

Discontinuities and singularities has proven difficult to represent in THM-modeling using the conventional FEM (Finite Element Method), leading to the development of the XFEM (Extended Finite Element Method). The XFEM relays on replacing the basis functions near a discontinuity, which in some cases can be quite tiresome. This thesis has applied the isogeometric THM-model for fully saturated soil to recreate simulations conducted using the XFEM. Without any alteration to the basis functions, the isogeometric model yields results comparable to the XFEM simulations. The simulations includes a crack in thermal loading, a dam seepage problem and a fully coupled problem.

For the second part of the thesis, the THM-model with ground freezing was utilised for simulations of the frost heave phenomena. Since the model is new, and still under development, a parametric study is first presented. Then a laboratory test with a frost heave cell was attempted recreated, and the effect of seasonal temperature variation was investigated. Finally, the THM-model with ground freezing was used in an attempt to recreate two stretches of railway damaged by frost heave. The parametric study indicates that besides the phase change parameters, the stiffness and hydraulic conductivity probably affects the solutions the most. The simulations of seasonal temperature variation, clearly shows how the ground freezing affects the temperature profiles and surface heave. The attempts to recreate laboratory and field results only partially succeeds. Some aspects of the problems are simulated better than others, and a main contributor to this problem is assumed to be the linearly elastic material model. The thesis show that there is need for further research, but also illustrates the potential and strength in a fully couped THM analysis.

Contents

List of Figures

List of Tables

Chapter 1

Introduction

1.1 Application of THM-modeling

There are several application areas for THM (Thermo-Hydro-Mechanical) modeling, and the most common is presented in this section.

Nuclear waste disposal

Nuclear waste is stored in containers deep under ground. The waste is still degenerating, generating heat. Both water and solids in the surrounding material expands, but the increase in water volume is usually greater than the increase in pore volume (Lewis and Schrefler (1998)). The pore pressure will increase, and the effective stress will decrease as much. This effect may cause a propagating failure around the container.

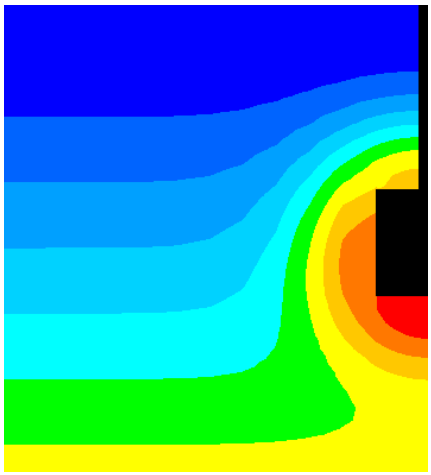

Figure 1.1: Pore pressure around a hot cylinder, red is higher pore pressure.

Geothermal reservoirs

Energy flowing from the earth's interior, is sometimes stopped and contained in certain natural reservoirs. Depending on the reservoir type, the energy is stores in solids, water or vapour. Modeling the mass/heat transfer can determine the potential, and improve the management of the reservoir.

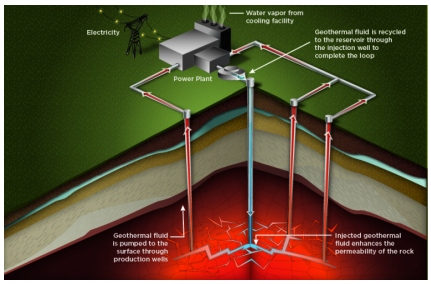

Figure 1.2: Geothermal Reservoir. Source: Energy.gov

CO_2 sequestration

Sequestration and storing of CO_2 under ground is highly dependent on temperature, flow and deformation. The Sleipner project (Arts et al. (2008)) at Utsira successfully pumped and stored CO_2 in the aquifer blow the seabed. The modeling is complex, and the CO_2 is both gas and super critical fluid while flowing in the aquifer.

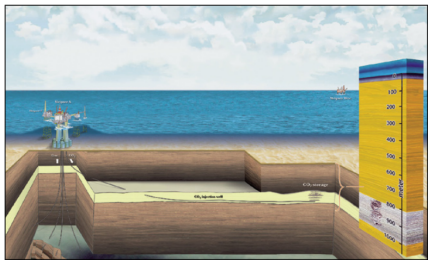

Figure 1.3: CO2 Sequestration. Source: Arts et al. (2008)

Underground energy storage

Underground energy storage is injecting energy into a aquifer or soil during summer, and extracting in the winter. The result is a cooling effect in summer, and heating effect in the winter. The effect and energy seepage of the storage area can be calculated using a THM-model.

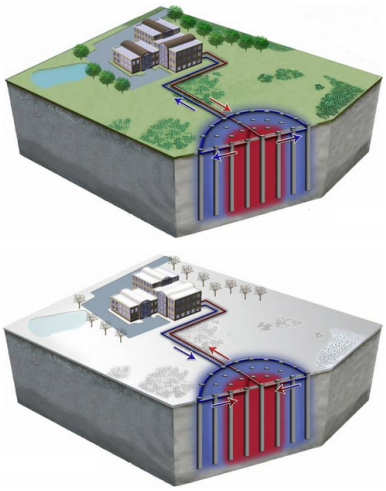

Figure 1.4: Geothermal Storage. Source: Underground-energy.com

Artificial ground freezing

Soil experiences a increase in strength and decrease in permeability when freezing. This can be exploited by artificially freezing the ground. Common applications areas is strengthening in tunnels during constructions, or to create a water tight plug in a water tunnel. THM-models can be used to predict strength, seepage and other related information in the ground freezing process.

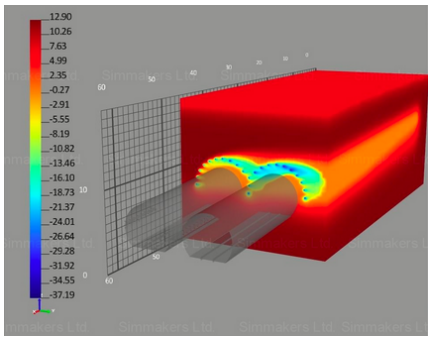

Figure 1.5: Ground Freezing in tunnel. Source: Simmakers.com

Natural ground freezing

Water expand by about 9% when freezing. In soil however, freezing creates a suction which results in an inflow of water. The contribution of inflowing water to the total heave, is much greater than the 9% expansion. A THM-model can represent the inflowing water, making it possible to predict the total heave.

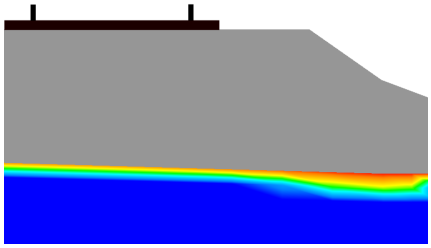

Figure 1.6: Ice forming below the frost protection layer for a railway. Blue is water, red is ice.

1.2 Background

In cold regions as in Norway, heave damage on roads is a common site. Due to damages on several new highways from 2009 to 2011, the Norwegian road department assessed the situation (Norwegian Road department (2012)). The conclusion points towards a cold winter, and lacking experience and competence in the industry, but also emphasising that the current guidelines are based on research made in the 1970's. The current standard in the industry is based on tables and hand calculation, and in some cases thermal models (more common) and *sequential* (T)HM-models are used.

This thesis is related to ongoing research on fully coupled THM-models at NTNU. This thesis focus is on discontinuity in THM-models, and on the ground freezing application. By preforming a case study, the thesis will investigate the possibilities and problems related to using fully coupled THM-models with phase change as an alternative to the current standard. There exist some commonly available software able to simulate frost heave (such as OpenGeoSys), however the codes developed at NTNU is used.

1.3 Objectives

The main objectives of this thesis are

1. Numerical studies on THM-modeling of saturated porous media using isogeometric analysis to illustrate discontinuities.

2. Parametric study on the THM model with ground freezing.

3. Frost heave cell simulation.

4. Seasonal temperature variation simulation.

5. Case study of frost heave.

1.4 Clarification on Software

This thesis uses two THM-model, one for THM modeling of saturated porous media without phase change and one for ground freezing, as presented in chapter 2 and 3. The two codes are written by PhD. Yared Worku Bekele (NTNU), based on IFEM by SINTEF. IFEM is an object oriented program for implementing linear and nonlinear partial differential equations with finite element solvers using B-splines and NURBS(Non-Uniform Rational B-Splines) as basis functions. IFEM is developed at the Department of Applied Mathematics, SINTEF ICT in Trondheim. The geometry and mesh is generally created using python and a geometry module. Meshing, parsing, material properties, time stepping, non-linearity settings and output points can be specified in the input file. An example input file is presented in appendix F. The post-processing is preformed in Matlab and GLview.

1.5 Limitations

The codes used in this thesis is still under development, and is prone to minor bugs, and has limited features. The calculations are performed on a regular laptop, and some important efficiency features are not implemented in the codes. To perform calculations within a reasonable time, the model is sometimes limited with respect to size, mesh and time stepping.

1.6 Structure of the Thesis

The thesis contains 7 chapter, where the first one is an introduction. Chapter 2 contains theory related to the fully saturated THM-model used in this thesis. Chapter 3 contains theory related to the THM-model with phase change, but is based on chapter 2. Chapter 4 contains theory on splines and isometric element analysis. Chapter 5 contains all the simulations carried out using the fully saturated THM-model, with one thermal consolidations and three discontinuity simulations. Chapter 6 contains all simulations carried out using the THM-model with phase change, including a parameter study, frost heave cell recreation, varying

temperature load and a case study. Each simulation and the relevant results is discussed after presenting the results, and the final conclusion and recommendations for further work is presented in chapter 7.

Chapter 2

THM Model for Saturated Soils: Theory

This chapter introduces the THM (Thermo-Hydro-Mechanical) model for fully saturated porous media.

2.1 General statements

2.1.1 Stress and Strain Relations

This section introduces relations between total stress, effective stress, strain and deformation. The relations can be find in a similar form in Lewis and Schrefler (1998). Effective stress is a function of total stress, pore pressure and gas pressure. This thesis only consider fully saturated materials, which yields the relation in equation 2.1.

$$\boldsymbol{\sigma}' = \boldsymbol{\sigma} - \alpha \mathbf{m} p \tag{2.1}$$

Where $\boldsymbol{\sigma}'$ and $\boldsymbol{\sigma}$ denotes effective and total stress respectively. α is Biot's coefficient, which is described in chapter 1.3 in Verruijt (2014), and p is the pore water pressure. $\mathbf{m}^T$=[1 1 1 0 0 0] is used several times in this thesis, either to remover shear strain/stress or to calculate the sum of a vector.

The stress-strain relation for elastic and non-elastic behavior is shown in equation 2.2 and 2.3 respectively.

$$\boldsymbol{\sigma}' = \mathbf{D}_e(\boldsymbol{\epsilon} - \boldsymbol{\epsilon}_0 - \boldsymbol{\epsilon}^T) \tag{2.2}$$

$$d\boldsymbol{\sigma}' = \mathbf{D}_T(d\boldsymbol{\epsilon} - d\boldsymbol{\epsilon}_0 - d\boldsymbol{\epsilon}^T) \tag{2.3}$$

Where $\mathbf{D}_e$ and $\mathbf{D}_T$ is the stiffness matrix for linear and non-linear behaviour. $\boldsymbol{\epsilon}$, $\boldsymbol{\epsilon}_0$ and $\boldsymbol{\epsilon}^T$ is total strain, initial strain and temperature strain respectively.

$$\boldsymbol{\epsilon}^T = \mathbf{m}\frac{\beta_{sw}}{3}T \tag{2.4}$$

T is temperature, n is porosity, and $\beta_{sw} = (\alpha - n)\beta_s + n\beta_w$ is the thermal expansion coefficient.

Total strain can be related to deformation by equation 2.6.

$$\boldsymbol{\epsilon} = \mathbf{L}\mathbf{u} \tag{2.5}$$

$$L^T = \begin{bmatrix} \frac{\delta}{\delta x} & 0 & 0 & \frac{\delta}{\delta y} & 0 & \frac{\delta}{\delta z} \\ 0 & \frac{\delta}{\delta y} & 0 & \frac{\delta}{\delta x} & \frac{\delta}{\delta z} & 0 \\ 0 & 0 & \frac{\delta}{\delta z} & 0 & \frac{\delta}{\delta y} & \frac{\delta}{\delta x} \end{bmatrix} \tag{2.6}$$

Where $\mathbf{u}$ is deformation.

The model used in this program is based on the plain strain assumption. The stress-strain for plane strain is shown in equation 2.7, also found in for example Bell (2013).

$$\begin{bmatrix} \sigma_{xx} \\ \sigma_{yy} \\ \sigma_{xy} \end{bmatrix} = \frac{E}{(1+\nu)(1-2\nu)} \begin{bmatrix} 1-\nu & \nu & 0 \\ \nu & 1-\nu & 0 \\ 0 & 0 & \frac{1-2\nu}{2} \end{bmatrix} \begin{bmatrix} \epsilon_{xx} \\ \epsilon_{yy} \\ \epsilon_{xy} \end{bmatrix} \tag{2.7}$$

Where E is Young's modulus, and ν is Poisson's ratio. This is a very simple model, but it is possible to develop and implement more advanced models (for example: Nishimura et al. (2009) and Alonso et al. (1990)) with further research.

2.1.2 Darcy's Law

A common formulation of Darcy's law is shown i equation 2.8 (also seen in Emdal (2013)). It may be rewritten with respect to liquid flow and pressure as shown in equation 2.9 (as seen in Verruijt (2014)).

$$v = ki = -k\frac{\Delta H}{\Delta L} \tag{2.8}$$

$$q_x = -\frac{k_x}{\gamma_w}\frac{\delta p}{\delta x} \qquad q_y = -\frac{k_y}{\gamma_w}\frac{\delta p}{\delta y} \qquad q_z = -\frac{k_z}{\gamma_w}(\frac{\delta p}{\delta z} - \rho_f g) \tag{2.9}$$

Where k is hydraulic conductivity. For use in the partial differential equations, $\nabla \cdot \mathbf{q}$ in relation to darcy's law is shown in equation 2.10.

$$-\nabla \cdot \mathbf{q} = -\frac{\delta q_x}{\delta x} - \frac{\delta q_y}{\delta y} - \frac{\delta q_z}{\delta z} = \nabla \cdot (\frac{\mathbf{k}}{\gamma_w}\big(\nabla p - \rho \mathbf{g}\big)) \tag{2.10}$$

It is also common to see the hydraulic conductivity as κ/μ, where κ is intrinsic permeability and μ is viscosity.

2.1.3 Fourier's Law

Fourier's law can be used to describe the heat flow in porous medium. The thermal conductivity is greatly dependent on the saturation and porosity of the soil, the effective thermal conductivity is therefor introduced as shown in figure 2.11, taken from Lewis and Schrefler (1998).

$$\mathbf{q}_F = -\boldsymbol{\chi}_{eff} \nabla T \tag{2.11}$$

Where $\mathbf{q}_F$ is the heat flux, T is temperature and the effective thermal conductivity is defined by the geometric mean, as shown in equation 2.12.

$$\chi_{eff} = \chi_w^n \chi_s^{1-n} \tag{2.12}$$

2.1.4 Heat Capacity

Heat capacity is a material property, expressing the energy required to heat the material. Formulation of heat capacity and the more relevant specific heat capacity is shown in equation 2.13 and 2.14.

$$C = \frac{\delta Q}{\delta T} \tag{2.13}$$

$$c = \frac{\delta C}{\delta m} \tag{2.14}$$

Where Q is energy, T is temperature and m is mass. Since the energy will be evaluated over a volume, the energy will be on the form ρc. The heat capacity for soil depend on both heat capacity for solid and water, as shown in equation 2.15.

$$(\rho c)_{sw} = (1-n)\rho_s c_s + n\rho_w c_w \tag{2.15}$$

2.2 Governing Equations

2.2.1 Linear Momentum Balance Equation

Moment equilibrium in three directions yields equation 2.16 to 2.18.

$$\frac{\delta \sigma_{xx}}{\delta x} + \frac{\delta \sigma_{yx}}{\delta y} + \frac{\delta \sigma_{zx}}{\delta z} = 0 \tag{2.16}$$

$$\frac{\delta \sigma_{xy}}{\delta x} + \frac{\delta \sigma_{yy}}{\delta y} + \frac{\delta \sigma_{zy}}{\delta z} = 0 \tag{2.17}$$

$$\frac{\delta \sigma_{xz}}{\delta x} + \frac{\delta \sigma_{yz}}{\delta y} + \frac{\delta \sigma_{zz}}{\delta z} - \rho g = 0 \tag{2.18}$$

Where $\sigma_{i,j}$ is total stress, i and j denotes directions, ρg is gravity forces, and $\sigma_{i,j}$=$\sigma_{j,i}$. In matrix form, denoted as shown in equation 2.19.

$$L^T \boldsymbol{\sigma} + \rho \mathbf{g} = 0 \tag{2.19}$$

The density is dependent on the porosity, and is formulated as in equation 2.20.

$$\rho = (1-n)\rho^s + n\rho^w \tag{2.20}$$

Applying relations from section 2.1.1 for non-linear materials to equation 2.19 results in equation 2.22.

$$\frac{1}{\delta t}(\mathbf{L}^T\left(\mathbf{D}_T(\delta \boldsymbol{\epsilon} - \delta \boldsymbol{\epsilon}_0 - \delta \boldsymbol{\epsilon}^T) - \alpha \mathbf{m} \delta p\right) + \delta \rho \mathbf{g}) = 0 \tag{2.21}$$

$$\frac{1}{\delta t}(\mathbf{L}^T\left(\mathbf{D}_T(\delta L\mathbf{u}-\delta\boldsymbol{\epsilon}_0-\mathbf{m}\delta\frac{\beta_s T}{3})-\alpha\mathbf{m}\delta p\right)+\delta\rho\mathbf{g})=0 \tag{2.22}$$

2.2.2 Mass Balance Equation

Assuming no internal source, such as condensation, the amount of liquid mass is always constant. The mass balance equation for the liquid fraction can be described as in equation 2.23, taken from Verruijt (2014).

$$\frac{\delta(n\rho_f)}{\delta t}+\frac{\delta(n\rho_f v_x^w)}{\delta x}+\frac{\delta(n\rho_f v_y^w)}{\delta y}+\frac{\delta(n\rho_f v_z^w)}{\delta z}=0 \tag{2.23}$$

Where n is porosity, ρ_f is fluid density and v^w is fluid velocity.

Similarly, the equation for the solid fraction is shown in equation 2.24.

$$\frac{\delta((1-n)\rho_s)}{\delta t}+\frac{\delta((1-n)\rho_s v_x^s)}{\delta x}+\frac{\delta(1-n)n\rho_s v_y^s)}{\delta y}+\frac{\delta(1-n)n\rho_s v_z^s)}{\delta z}=0 \tag{2.24}$$

Where ρ_s is the grain density and v^s is the grain velocity

Subtracting equation 2.24 from 2.23, dividing by density and performing the product rule for derivatives yields equation 2.25.

$$n\frac{\delta\rho_f}{\rho_f\delta t}+\cancel{\frac{\delta n}{\delta t}}+\nabla\cdot n\mathbf{v}^s-\left((1-n)\frac{\delta\rho_s}{\rho_s\delta t}+\cancel{\frac{\delta(1-n)}{\delta t}}+\nabla\cdot(1-n)\mathbf{v}^s\right)=0 \tag{2.25}$$

Applying the relations for ρ_s and ρ_f from Lewis and Schrefler (1998), yields equation 2.26.

$$\begin{aligned}\frac{n}{\rho_{f0}e^{-\beta_w T+\frac{1}{K_f}(p-p_0)}}\frac{\delta\rho_{f0}e^{-\beta_w T+\frac{1}{K_f}(p-p_0)}}{\delta t}+\frac{\alpha-n}{K_s}\frac{\delta p}{\delta t}-\beta_s(\alpha-n)\frac{\delta T}{\delta t}-\\ (1-\alpha)\nabla\cdot\mathbf{v}^s+\nabla\cdot(1-n)\mathbf{v}^s+\nabla\cdot n\mathbf{v}^w=0\end{aligned} \tag{2.26}$$

Further simplifications results in equation 2.27.

$$\hat{S}\frac{\delta p}{\delta t}-\beta_{sw}\frac{\delta T}{\delta t}+\alpha\nabla\cdot\mathbf{v}^s+\nabla\cdot n\mathbf{v}^{ws}=0 \tag{2.27}$$

Where $\beta_{sw}=(\alpha-n)\beta_s+n\beta_w$, $\mathbf{v}^{ws}=\mathbf{v}^w-\mathbf{v}^w$, and $\hat{S}$=n/K_f+(α-n)/K_s.

$\mathbf{q}$=$n\mathbf{v}^{ws}$ is the specific discharge, and $\delta\epsilon/\delta t=\nabla\cdot\mathbf{v}^s$. Applying darcy's law and strain relations for section 2.1 yields the final equation for the mass equilibrium:

$$\alpha \mathbf{m}^T \mathbf{L} \frac{\delta \mathbf{u}}{\delta t} + \hat{S} \frac{\delta p}{\delta t} - \beta_{sw} \frac{\delta T}{\delta t} = -\nabla \cdot \left(\frac{k}{\gamma_w} \left(\nabla p - \rho \mathbf{g} \right) \right) \tag{2.28}$$

2.2.3 Energy Balance Equation

The energy balance equation is defined by three processes: Heat capacity (section 2.1.4), the heat capacity in the water flow (advection), and Fourier's law(section 2.1.3). With no internal energy source, the equilibrium is defined as in equation 2.29 and 2.30.

$$(\rho c)_{sw} \frac{\delta T}{\delta t} + \rho_w c_w \mathbf{q} \nabla T + \nabla \cdot \mathbf{q}_F = 0 \tag{2.29}$$

$$(\rho c)_{sw} \frac{\delta T}{\delta t} + \rho_w c_w \left(\frac{\mathbf{k}}{\gamma_w} (-\nabla p + \rho \mathbf{g}) \right) \nabla T + \nabla \cdot (\boldsymbol{\chi}_{eff} \nabla T) = 0 \tag{2.30}$$

2.2.4 Initial Conditions

A initial field for all degrees of freedom must be obtained in order to solve the partial differential equations. The initial deformation field, $\mathbf{u} = \mathbf{u}_0$, may be set to 0 or taken from an already existing field. The initial pore pressure field, $p = p_0$, may for example be hydrostatic, based on steady state flow or dependent on the layering. The initial temperature field, $T = T_0$, may for instance be found using a steady state solution. The temperature field is however in reality not linear with depth, as explained by introducing sinusoidal functions and trumpet curves in Andersland and Ladanyi (2004). A realistic initial field can be found by running a temperature simulation for the last several years.

2.2.5 Boundary Conditions

A Dirichlet boundary condition specifies the solution along a given boundary, and for this thesis the Dirichlet boundary conditions are:

$$\begin{aligned} \mathbf{u} &= \hat{\mathbf{u}} \quad on\ \Gamma_D^u \\ \mathbf{p} &= \hat{\mathbf{p}} \quad on\ \Gamma_D^p \\ \mathbf{T} &= \hat{\mathbf{T}} \quad on\ \Gamma_D^T \end{aligned} \tag{2.31}$$

A Neumann boundary condition specifies the derivative of the solution along a given boundary, and for this thesis the Neumann boundary conditions are:

$$\begin{aligned} \boldsymbol{\sigma}\mathbf{n} &= \bar{\mathbf{t}} \quad on\ \Gamma_N^u \\ \rho^w \frac{\mathbf{k}}{\gamma_w}(-\nabla p + \rho^w \mathbf{g}) \cdot \mathbf{n} &= \mathbf{q}^w \quad on\ \Gamma_N^p \\ (-\chi_{eff}\nabla T)^T \cdot \mathbf{n} &= \mathbf{q}^T \quad on\ \Gamma_N^T \end{aligned} \tag{2.32}$$

Where **n** is the normal outwards unit vector.

2.3 Finite Element Discretization

2.3.1 Development of the Weak Form

A partial differential equation can be solved with a strong or a weak form. The strong form requires point wise equilibrium, while the weak form requires equilibrium over a domain. Equation 2.33 and 2.34 describes the development of a weak formulation.

$$\mathbf{AX} + \mathbf{B}\dot{\mathbf{X}} - \mathbf{C} = 0 \tag{2.33}$$

$$\int_\Omega w^T(\mathbf{AX} + \mathbf{B}\dot{\mathbf{X}} - \mathbf{C})d\Omega = \int_\Gamma w^T \mathbf{f} d\Gamma \tag{2.34}$$

Where Γ is the boundary, **f** is some boundary action, and w^T is the weighing function.

Linear Momentum balance equation

Applying the weak form on equation 2.21 yields equation 2.35

$$\int_\Omega (Lw)^T \left(\mathbf{D}_T(\delta L\mathbf{u} - \delta\boldsymbol{\epsilon}_0 - \mathbf{m}\delta\frac{\beta_s T}{3}) - \alpha\mathbf{m}\delta p\right)d\Omega = \int_\Omega w^T \rho\mathbf{g}d\Omega + \int_\Gamma w^T \mathbf{t}d\Gamma \tag{2.35}$$

Mass balance equation

Applying the weak form on equation 2.28 yields equation 2.36

$$\int_\Omega (w_p^T \alpha \mathbf{m}^T \mathbf{L} \frac{\delta \mathbf{u}}{\delta t} - w_p^T \beta_{sw} \frac{\delta T}{\delta t} + w_p^T S \frac{\delta p}{\delta t})\, d\Omega = -\int_\Omega (\nabla w_p)^T \frac{k}{\gamma_w} (\nabla p - \rho \mathbf{g}) d\Omega + \int_\Gamma w_p^T \frac{q^w}{\rho^w} d\Gamma \tag{2.36}$$

Energy balance equation

Applying the weak form on equation 2.30 yields equation 2.37.

$$\int_\Omega w_T^T (\rho c)_{sw} \frac{\delta T}{\delta t} d\Omega + \int_\Omega w_T^T \big(\rho_w c_w \frac{\mathbf{k}}{\gamma_w} (-\nabla p + \rho \mathbf{g}) \nabla T\big) + (\nabla w)_T^T (\chi_{eff} \nabla T) d\Omega = -\int_\Gamma \mathbf{q}^{Te} d\Gamma \tag{2.37}$$

Where $\mathbf{q}^{Te}$ is flow of energy due to temperature.

2.3.2 Discretization in Space

Using basis functions, N, described in chapter 4 and a set of nodes, a general field can be describes for a given values. This paper is based on deformation, pore pressure and temperature as the dependent variable. The fields are represented as shown in equation 2.38.

$$\mathbf{u} = \mathbf{N}_u \bar{\mathbf{u}} \qquad p = \mathbf{N}_p \bar{\mathbf{p}} \qquad \mathbf{T} = \mathbf{N}_T \bar{\mathbf{T}} \tag{2.38}$$

Where $\mathbf{N}$ is the basis functions, $\bar{\mathbf{u}}$, $\bar{\mathbf{p}}$ and $\bar{\mathbf{T}}$ is the nodal values. A common way to select the the weighing functions for the weak form, is to set the weighing functions equal to the basis functions. This method is called Galerkin's method, and is applied in this thesis.

Linear momentum balance equation

Applying spatial discretization and Galekin's method to equation 2.35 yields equation 2.39.

$$\int_\Omega \mathbf{B}_u^T \mathbf{D}_T \mathbf{B}_u d\Omega \frac{\delta \bar{\mathbf{u}}}{\delta t} - \int_\Omega \mathbf{B}_u^T \mathbf{D}_T d\boldsymbol{\epsilon}_0 d\Omega - \int_\Omega \mathbf{B}_u^T \mathbf{D}_T \mathbf{m} \frac{\beta_{sw}}{3} \mathbf{N}_T d\Omega \frac{\delta \bar{\mathbf{T}}}{\delta t} - \int_\Omega \mathbf{B}_u^T \alpha \mathbf{m} d\Omega \frac{\delta \bar{\mathbf{p}}}{\delta t} = \int_\Omega N_u^T \frac{\delta}{\delta t} \rho \mathbf{g} d\Omega + \int_\Gamma N_u^T \frac{\delta}{\delta t} \mathbf{t} d\Gamma \tag{2.39}$$

Where $\mathbf{B} = \mathbf{L}\mathbf{N}_u$

Mass balance equation

Applying spatial discretization and Galekin's method to equation 2.36 yields equation 2.40.

$$\begin{aligned}\int_\Omega N_p^T \alpha \mathbf{m}^T \mathbf{B} d\Omega \frac{\delta \bar{\mathbf{u}}}{\delta t} + \int_\Omega N_p^T \hat{S} \mathbf{N}_p d\Omega \frac{\delta \bar{\mathbf{p}}}{\delta t} + \int_\Omega -N_p^T \beta_{sw} \mathbf{N}_T d\Omega \frac{\delta \bar{\mathbf{T}}}{\delta t} = \\ -\int_\Omega (\nabla N_p)^T \frac{k}{\gamma_w} \nabla \mathbf{N}_p d\Omega \bar{\mathbf{p}} + \int_\Omega (\nabla N_p)^T \frac{k}{\gamma_w} \rho \mathbf{g} d\Omega + \int_\Gamma N_p^T \frac{q^w}{\rho^w} d\Gamma\end{aligned} \tag{2.40}$$

Energy balance equation

Applying spatial discretization and Galekin's method to equation 2.37 yields equation 2.41.

$$\begin{aligned}\int_\Omega \mathbf{N}_T^T (\rho c)_{sw} \mathbf{N}_T d\Omega \frac{\delta \bar{\mathbf{T}}}{\delta t} + \int_\Omega \Big(\mathbf{N}_T^T \big(\rho_w c_w \frac{\mathbf{k}}{\gamma_w} (-\nabla p + \rho_w \mathbf{g}) \mathbf{N}_T \big) + \mathbf{N}_T^T (\chi_{eff} \nabla \mathbf{N}_T \Big) d\Omega \, \bar{\mathbf{T}} = \\ -\int_\Gamma \mathbf{N}_T^T \mathbf{q}^{Te} d\Gamma\end{aligned} \tag{2.41}$$

2.3.3 Discretization in Time

In order to remove the time differentiated vector, a time step Δt is introduced. When introducing the time step, one must also choose the variable vector to represent the time interval. θ denotes the chosen scheme, and can take any value from 0 to 1. The three most common schemes are:

- $\theta = 0$: This is an explicit scheme, also known as forward Euler method.
- $\theta = 1$: This is an implicit scheme, also known as backwards Euler method.
- $\theta = 0.5$: This is known as the Crank-Nicolson scheme, where the current and next solution is equally weighted.

Applying θ to the variable vector yields equation 2.42 and 2.43

$$\mathbf{X}_{n+\theta} = (1-\theta)\mathbf{X}_n + \theta \mathbf{X}_{n+1} \tag{2.42}$$

$$(\frac{d\mathbf{X}}{dt})_{n+\theta} = \frac{\mathbf{X}_{n+1} - \mathbf{X}_n}{\Delta t} \tag{2.43}$$

Applying equation 2.42 and 2.43 , with equation 2.33 yields equation 2.44.

$$\mathbf{A}\big((1-\theta)\mathbf{X}_n + \Theta\mathbf{X}_{n+1}\big) + \mathbf{B}\frac{\mathbf{X}_{n+1}-\mathbf{X}_n}{\Delta t} - \mathbf{C} = 0 \tag{2.44}$$

Linear moment balance equation

Applying time discretization on equation 2.39, and multiplying with Δt yields equation 2.45.

$$\int_\Omega \mathbf{B}_u^T\mathbf{D}_T\mathbf{B}_u d\Omega\big(\frac{\mathbf{u}_{n+1}+\mathbf{u}_n}{\Delta t}\big) - \int_\Omega \mathbf{B}_u^T\mathbf{D}_T\mathbf{m}\frac{\beta_{sw}}{3}\mathbf{N}_T d\Omega\big(\frac{\mathbf{T}_{n+1}+\mathbf{T}_n}{\Delta t}\big) - \int_\Omega \mathbf{B}_u^T\alpha\mathbf{m}d\Omega\big(\frac{p_{n+1}+p_n}{\Delta t}\big) = \frac{1}{\Delta t}\Big(\int_\Omega N_u^T\rho d\mathbf{g}d\Omega + \int_\Gamma N_u^T d\mathbf{t}d\Gamma - \int_\Omega \mathbf{B}_u^T\mathbf{D}_T\boldsymbol{d\epsilon}_0 d\Omega\Big) \tag{2.45}$$

Mass balance equation

Applying the time discretization on equation 2.40 yields equation 2.46.

$$\int_\Omega N_p^T\alpha\mathbf{m}^T\mathbf{B}d\Omega\frac{\bar{\mathbf{u}}_{n+1}-\bar{\mathbf{u}}_n}{\Delta t} + \int_\Omega N_p^T\hat{S}\mathbf{N}_p d\Omega\frac{\bar{\mathbf{p}}_{n+1}-\bar{\mathbf{p}}_n}{\Delta t} + \int_\Omega -N_p^T\beta_{sw}\mathbf{N}_T d\Omega\frac{\bar{\mathbf{T}}_{n+1}-\bar{\mathbf{T}}_n}{\Delta t} = -\int_\Omega (\nabla N_p)^T\frac{k}{\gamma_w}\nabla\mathbf{N}_p d\Omega\big((1-\theta)\bar{\mathbf{p}}-\theta\bar{\mathbf{p}}\big) + \int_\Omega (\nabla N_p)^T\frac{k}{\gamma_w}\rho\mathbf{g}d\Omega + \int_\Gamma N_p^T\frac{q^w}{\rho^w}d\Gamma \tag{2.46}$$

Energy balance equation

Applying the time discretization on equation 2.41 yields equation 2.47.

$$\begin{aligned}\int_\Omega \Big(\mathbf{N}_T^T\big(\rho_w c_w\frac{\mathbf{k}}{\gamma_w}(-\nabla p+\rho_w\mathbf{g})\mathbf{N}_T\big) + \mathbf{N}_T^T(\chi_{eff}\nabla\mathbf{N}_T\Big)d\Omega\big((1-\theta)\bar{\mathbf{T}}-\theta\bar{\mathbf{T}}\big) \\ + \int_\Omega \mathbf{N}_T^T(\rho c)_{sw}\mathbf{N}_T d\Omega\frac{\bar{\mathbf{T}}_{n+1}-\bar{\mathbf{T}}_n}{\Delta t} = -\int_\Gamma \mathbf{N}_T^T\mathbf{q}^{Te}d\Gamma\end{aligned} \tag{2.47}$$

Block matrix form

Combining equation 2.45, 2.46 and 2.47 in a block matrix yields the matrix system 2.48.

$$\begin{aligned}\theta\Delta t\begin{bmatrix}0&0&0\\0&K_{pp}&0\\0&0&K_{TT}\end{bmatrix}\begin{bmatrix}\bar{\mathbf{u}}\\\bar{\mathbf{p}}\\\bar{\mathbf{T}}\end{bmatrix}_{n+1}+\begin{bmatrix}C_{uu}&C_{up}&C_{uT}\\-C_{up}^T&C_{pp}&C_{pT}\\0&0&C_{TT}\end{bmatrix}\begin{bmatrix}\bar{\mathbf{u}}\\\bar{\mathbf{p}}\\\bar{\mathbf{T}}\end{bmatrix}_{n+1}=\\(\theta-1)\Delta t\begin{bmatrix}0&0&0\\0&K_{pp}&0\\0&0&K_{TT}\end{bmatrix}\begin{bmatrix}\bar{\mathbf{u}}\\\bar{\mathbf{p}}\\\bar{\mathbf{T}}\end{bmatrix}_{n}+\begin{bmatrix}C_{uu}&C_{up}&C_{uT}\\-C_{up}^T&C_{pp}&C_{pT}\\0&0&C_{TT}\end{bmatrix}\begin{bmatrix}\bar{\mathbf{u}}\\\bar{\mathbf{p}}\\\bar{\mathbf{T}}\end{bmatrix}_{n}+\Delta t\begin{bmatrix}\frac{df_u}{\Delta t}\\f_p\\f_t\end{bmatrix}\end{aligned}\tag{2.48}$$

Where the following equations apply:

$$K_{pp}=\int_\Omega(\nabla\mathbf{N}_p)^T\frac{k}{\gamma_w}\nabla\mathbf{N}_p d\Omega\tag{2.49}$$

$$K_{TT}=\int_\Omega\left(\mathbf{N}_T^T\left(\rho_w c_w\frac{\mathbf{k}}{\gamma_w}(-\nabla p+\rho_w\mathbf{g})\mathbf{N}_T\right)+\mathbf{N}_T^T(\chi_{eff}\nabla\mathbf{N}_T\right)d\Omega\tag{2.50}$$

$$C_{uu}=\int_\Omega\mathbf{B}_u^T\mathbf{D}_T\mathbf{B}_u d\Omega\tag{2.51}$$

$$C_{up}=-\int_\Omega\mathbf{B}_u^T\alpha\mathbf{m}\mathbf{N}_p d\Omega\tag{2.52}$$

$$C_{uT}=\int_\Omega\mathbf{D}_T\mathbf{m}\frac{\beta_{sw}}{3}\mathbf{N}_t d\Omega\tag{2.53}$$

$$C_{pp}=\int_\Omega\mathbf{N}_p^T\hat{S}\mathbf{N}_p d\Omega\tag{2.54}$$

$$C_{pT}=\int_\Omega-N_p^T\beta_{sw}\mathbf{N}_T d\Omega\tag{2.55}$$

$$C_{TT}=\int_\Omega\mathbf{N}_T^T(\rho c)_{sw}\mathbf{N}_T d\Omega\tag{2.56}$$

$$f_p=\int_\Omega(\nabla N_p)^T\frac{k}{\gamma_w}\rho\mathbf{g}d\Omega+\int_\Gamma N_p^T\frac{q^w}{\rho^w}d\Gamma\tag{2.57}$$

$$f_t = -\int_\Gamma \mathbf{N}_T^T \mathbf{q}^{Te} d\Gamma \tag{2.58}$$

2.3.4 Numerical integration

The integrals in the governing equations are solved using numerical integration. The procedure is as explained in general in Bell (2013) and specific in Cottrell et al. (2009), with Gaussian quadrature. The Gaussian quadrature for one dimension is shown in equation 2.59.

$$I = \int_{-1}^{1} g(\zeta) d\zeta \approx \sum_{k=1}^{n} w_k g(\zeta_k) \tag{2.59}$$

Where w is the weight of the value in the k'th Gauss point. For calculation, each element in the knot space is normalised to size a size of 2. Since area and volume is a double or triple integral, the solution is based on Gauss points in 2 or 3 directions.

It is normal to differentiate between full and reduced integration. Full integration represent the integral exactly for a undistorted element, while reduced integration is one order lower than full integration. The order is defined by the number of Gauss points in each direction.

2.3.5 Newton-Raphson iteration

The occurrence of pressure in K_{TT} makes the equations system non-linear. After calculating the initial unknown vector, the residual is calculated as shown in equation 2.60.

$$\mathbf{R}_{n+1} = (\Delta t \mathbf{K} + \mathbf{C})\mathbf{X}_{n+1} - \mathbf{C}\mathbf{X}_n - \Delta t \mathbf{X}_{n+1} \tag{2.60}$$

Using first-order Taylor expansion and Newton-Raphson iteration, the i'th step is found as in equation 2.62.

$$\mathbf{R}_{n+1}^i + \frac{\delta \mathbf{R}}{\delta \mathbf{X}}\Big|_{n+1}^i \Delta \mathbf{X}_{n+1}^{i+1} = 0 \tag{2.61}$$

$$\mathbf{X}_{n+1}^{i+1} = \mathbf{X}_{n+1}^i + \Delta \mathbf{X}_{n+1}^{i+1} \tag{2.62}$$

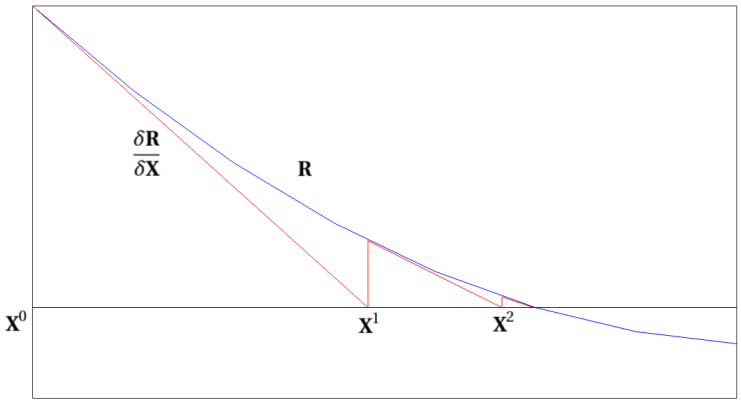

Figure 2.1: Illustration of the Newton-Raphson method

Chapter 3

THM Model for Ground Freezing: Theory

This chapter introduces the THM (Thermo-Hydro-Mechanical) model with ground freezing. The model is based on the same principles as the model presented in chapter 2, the main focus in this chapter is hence to introduce the ground freezing part of the model. The model is also presented in Bekele et al. (2016).

3.1 General statements

3.1.1 Material Time Derivative

When dealing with a derivative with a moving coordinate system(typically following a particle), it is very useful to apply the material derivative notation. The simplest form is widespread (for instance presented in continuummechanics.org), and shown in equation 3.1.

$$\frac{Df(x,t)}{Dt} = \frac{\delta f(x,t)}{\delta t} + v\frac{\delta f(x,t)}{\delta x} \tag{3.1}$$

Equation 3.1 can be expanded to more dimensions, as well as to including the different phases. Equation 3.2 is the material derivative with respect to the same phase, while equation 3.3 is the derivative of a phase property with respect to the solid phase.

$$\frac{D_\alpha f^\alpha}{Dt} = \frac{\delta f^\alpha}{\delta t} + \nabla f^\alpha \cdot \mathbf{v}^\alpha \tag{3.2}$$

$$\frac{D_s f^\alpha}{Dt} = \frac{D_\alpha f^\alpha}{Dt} + \nabla f^\alpha \cdot (\mathbf{v}^s - \mathbf{v}^\alpha) \tag{3.3}$$

Where **v** is velocity, and s and α denotes the solid or ice/water phase respectively.

3.1.2 Thermal Properties

Both thermal conductivity and heat capacity for ice must be included, as shown in equation 3.4 and 3.5.

$$(\rho c)_{eff} = (1-n)\rho_s c_s + nS_w\rho_w c_w + nS_i\rho_i c_i \tag{3.4}$$

$$\chi_{eff} = \chi_s^{1-n}\chi_w^{nS_w}\chi_i^{nS_i} \tag{3.5}$$

The amount of energy needed for a material to change state, is referred to as latent heat. The general formulation of latent heat is shown in equation 3.6.

$$L = \frac{Q}{m} \tag{3.6}$$

Where L is latent heat, Q is energy and m is mass. Latent heat of fusion for water is the relevant latent heat in this thesis, and is denoted L_f

3.1.3 Modified Clausius-Clapeyron Equation

Adding phase change introduces a new variable, ice pressure. It is possible to add this variable in the unknown vector, along with u, p^w and T. The model used in this thesis, does however utilise the close connection between water and ice pressure. This relation is shown in equation 3.7, and also found in for example Nishimura et al. (2009).

$$p^i = \frac{\rho_i}{\rho_w}p^w - \rho_i L_f ln(\frac{T}{T_0}) \tag{3.7}$$

Where T_0 is 273.15 K (0 degree Celsius).

3.1.4 Saturation Curves

Below 0 degree Celsius, water gradually freezes with decreasing temperature. As the model is limited to fully saturated materials, S_i+S_w=1. The suggested relation between S_w, temperature and pore pressure is shown in equation 3.8, similar to the relation presented in

Nishimura et al. (2009).

$$S_w = 1 - S_i^{max}\Big[1 - \Big(1 + \big(S^{\alpha}(p^i - p^w)\big)^{S^{\beta}}\Big)^{-S^{\gamma}}\Big] \tag{3.8}$$

Where S^{α}, S^{β} and S^{γ} is the saturation model parameters. Applying the modified Clausius-Clapeyron equation yields equation 3.9.

$$S_w = 1 - S_i^{max}\Big[1 - \big[1 + \Big(S^{\alpha}\big((\frac{\rho_i}{\rho_w} - 1)p^w - \rho_i L_f ln(\frac{T}{T_0})\big)^{S^{\beta}}\big]^{-S^{\gamma}}\Big] \tag{3.9}$$

S_w is hence a function of p^w and T, making it possible to simplify the time derivative of the water saturation as shown in equation 3.10.

$$\frac{\delta S_w}{\delta t} = \frac{\delta S_w}{\delta p^w}\frac{\delta p^w}{\delta t} + \frac{\delta S_w}{\delta T}\frac{\delta T}{\delta t} = S_p\frac{\delta p^w}{\delta t} + S_T\frac{\delta T}{\delta t} \tag{3.10}$$

Where S_p and S_T is the isothermal and non-isothermal water capacities.

3.1.5 Relation between Water Saturation and Permeability

Water freezing will gradually decrease the permeability of the material. This is corrected with a correction parameter k_r, resulting in an effective hydraulic conductivity as $k_r\mathbf{k}$. Where $\mathbf{k}$ is the unfrozen hydraulic conductivity and k_r is as shown in equation 3.11. The same relation is used in Nishimura et al. (2009).

$$k_r = \sqrt{S_w}\big(1 - (1 - S_w^{\frac{1}{m^p}})^{m^p}\big)^2 \tag{3.11}$$

Where m^p is the permeability model parameter.

3.1.6 Relation between Ice Saturation and Strength

As shown in equation 2.7, the plane strain assumption is defined by E and ν. The plane strain assumption is still valid, but both E and ν must be adjusted, since they are highly dependent on the ice saturation. Both are assumed logarithmically dependent, as shown in equation 3.12 and 3.13.

$$E = \big(\frac{E_i}{E_s}\big)^{S_i^{\eta}}E_s \tag{3.12}$$

$$\nu = \left(\frac{\nu_i}{\nu_s}\right)^{S_i^{\eta}} \nu_s \tag{3.13}$$

Where i and s denotes the ice and solid skeletons properties respectively, for Young's modules and Poisson's ratio. η is the strength model parameter.

The ice saturation will also affect the effective stress. Equation 2.3 adjusted for phase change yields equation 3.14.

$$d\boldsymbol{\sigma}' = \mathbf{D}_T(d\boldsymbol{\epsilon} - d\boldsymbol{\epsilon}_0 - d\boldsymbol{\epsilon}^T - d\boldsymbol{\epsilon}^{ph}) \tag{3.14}$$

Where $\boldsymbol{\epsilon}^{ph}$ is strain due to phase change. The volumetric strain due to phase change can be expressed as in equation 3.15, and assuming isotropic expansion/contraction the strain is given by equation 3.16.

$$\delta\dot{\epsilon}_v^{ph} = n\frac{\rho_w - \rho_i}{\rho_w S_i + \rho_i S_w}\frac{D_s S_i}{Dt} \tag{3.15}$$

$$d\epsilon^{ph} = \frac{1}{3}\Big(\frac{\delta\epsilon_v^{ph}}{\delta S_i} dS_i\Big)\mathbf{m} \tag{3.16}$$

3.2 Governing Equations

3.2.1 Linear Momentum Balance Equation

The general eqaution 2.19 still holds, however with alteration to equation 2.1 presented in equation 3.17 and strain as presented in section 3.1.6.

$$\boldsymbol{\sigma}' = \boldsymbol{\sigma} - \mathbf{m}p^w - S_i\mathbf{m}(p^i - p^w) \tag{3.17}$$

Similar to equation 2.21 and 2.22, the momentum equalibrium may be rewritten as:

$$\frac{1}{\delta t}(\mathbf{L}^T\big(\mathbf{D}_T(\delta\boldsymbol{\epsilon} - \delta\boldsymbol{\epsilon}_0 - \delta\boldsymbol{\epsilon}^T - \delta\boldsymbol{\epsilon}^{ph}) - \mathbf{m}\delta p^w - S_i\mathbf{m}\delta(p^i - p^w)\big) + \delta\rho\mathbf{g}) = 0 \tag{3.18}$$

3.2.2 Mass Balance Equation

Equation 3.19 is taken from Lewis and Schrefler (1998)(eq.2.202), and is developed assuming Biot's coefficient equal to one and incompressible grains. Lewis and Schrefler (1998) base

the development on a two phase medium with gas and liquid, the model used in this thesis applies the same principals for an ice and water relation.

$$\frac{nS_w}{K_w}\frac{D_s p^w}{Dt} + S_w \nabla \cdot \mathbf{v}^s - \beta_{sw}\frac{D_s T}{Dt} + \frac{1}{\rho^w}\nabla \cdot (nS_w \rho^w \mathbf{v}^{ws}) = -\frac{\dot{m}}{\rho^w} \tag{3.19}$$

Where ρ^α is the material density as defined in equation 3.20, $\mathbf{v}^{\alpha\beta} = \mathbf{v}^\alpha - \mathbf{v}^\beta$, and $\dot{m}$ is the quantity of inflow per time unit related to volume due to phase change.

$$\rho^s = (1-n)\rho_s \qquad \rho^w = nS_w\rho_w \qquad \rho^i = nS_i\rho_i \tag{3.20}$$

Assuming that thermal expansion is neglectable, as well as water being incompressible, equation 3.20 may be rewritten as equation 3.21 and 3.22 for the water and ice phase respectively. Equation 3.23 follows from $S_w + S_i = 1$.

$$\rho^w S_w \nabla \mathbf{v}^s + n\rho^w \frac{D_s S_w}{Dt} + \nabla(nS_w \rho^w \mathbf{v}^{ws}) = -\dot{m} \tag{3.21}$$

$$\rho^i S_w \nabla \mathbf{v}^s + n\rho^w \frac{D_s S_w}{Dt} + \nabla(nS_w \rho^w \mathbf{v}^{ws}) = -\dot{m} \tag{3.22}$$

$$\frac{D_s S_w}{Dt} = -\frac{D_s S_i}{Dt} \tag{3.23}$$

Combining the equation 3.21 and 3.22 with equation 3.23, assuming no loss of mass and neglecting $\mathbf{v}^{is}$ yields equation 3.24.

$$(\rho_w S_w + \rho_i S_i)\nabla \cdot \mathbf{v}^s + n(\rho_w - \rho_i)\frac{D_s S_w}{Dt} + \rho_w \nabla \cdot \mathbf{v}^{ws} \tag{3.24}$$

3.2.3 Energy Balance Equation

The energy balance equation is similar to what presented in equation 2.29. The alterations consist of including latent heat of fusion, properties of ice and the material derivative notation. The Result is shown in equation 3.25.

$$(\rho c)_{eff}\frac{D_s T}{Dt} + \mathbf{a}\nabla T + L_f \xi \frac{D_s S_w}{Dt} - \nabla \mathbf{q}_F = Q \tag{3.25}$$

Where $\mathbf{a}$=$(\rho c)_{adv}\mathbf{v}^{ws}$ is the advective heat transfer vector, and the specific heat density's and mass-volume relation ξ is defined in equation 3.26. Q is a source or sink term, and $\mathbf{q}_F$ still

follows Fourier's law, but with ice conductivity included.

$$\begin{aligned}(\rho c)_{eff} &= (1-n)\rho_s c_s + nS_w\rho_w c_w + nS_i\rho_i c_i \\ (\rho c)_{adv} &= \rho_w c_w + \frac{S_i}{S_w}\rho_i c_i \\ \xi &= \frac{n\rho_i}{S_w + \frac{\rho_i}{\rho_w}S_i}\end{aligned} \tag{3.26}$$

3.3 Finite Element Discretization

The steps to discretize the governing equations is shown in chapter 2. It can be shown that applying the weak formulation, and discretizing in both space and time yields the block matrix presented in equation 3.27. The numerical integration is the same, and the Newton-Raphson method is still the chosen iteration method. When the water velocities are high, the energy balance equation may become unstable. If specified, the SUPG (Streamline Upwind Petrov Galerkin) stabilization method is implemented. The contribution from SUPG is shown in equation 3.38, 3.40 and 3.42.

$$\begin{aligned}\Delta t \begin{bmatrix} 0 & 0 & 0 \\ 0 & K_{pp} & 0 \\ 0 & 0 & K^*_{TT} \end{bmatrix} \begin{bmatrix} \bar{\mathbf{u}} \\ \bar{\mathbf{p}} \\ \bar{\mathbf{T}} \end{bmatrix}_{n+1} + \begin{bmatrix} C_{uu} & C_{up} & C_{uT} \\ C^T_{pu} & C_{pp} & C_{pT} \\ 0 & C^*_{Tp} & C^*_{TT} \end{bmatrix} \begin{bmatrix} \bar{\mathbf{u}} \\ \bar{\mathbf{p}} \\ \bar{\mathbf{T}} \end{bmatrix}_{n+1} \\ = \begin{bmatrix} C_{uu} & C_{up} & C_{uT} \\ C^T_{pu} & C_{pp} & C_{pT} \\ 0 & C^*_{Tp} & C^*_{TT} \end{bmatrix} \begin{bmatrix} \bar{\mathbf{u}} \\ \bar{\mathbf{p}} \\ \bar{\mathbf{T}} \end{bmatrix}_{n} + \Delta t \begin{bmatrix} \frac{df_u}{\Delta t} \\ f_p \\ f_t \end{bmatrix}\end{aligned} \tag{3.27}$$

Where the following equations applies:

$$C_{uu} = \int_\Omega \nabla \mathbf{N}_u^T \mathbf{D} \mathbf{N}_u d\Omega \tag{3.28}$$

$$C_{up} = \int_\Omega \nabla \mathbf{N}_u^T \Big(\frac{\delta \boldsymbol{\sigma}}{\delta p^w} - \mathbf{D} \frac{\delta \epsilon^{ph}}{\delta p^w} \Big) \mathbf{N}_p d\Omega \tag{3.29}$$

$$C_{up} = \int_\Omega \nabla \mathbf{N}_u^T \Big(\frac{\delta \boldsymbol{\sigma}}{\delta T} - \mathbf{D} \frac{\delta \epsilon^{ph}}{\delta T} \Big) \mathbf{N}_T d\Omega \tag{3.30}$$

$$f_u = \int_{\Gamma_N^u} \mathbf{N}_u^T \bar{\mathbf{t}} d\Gamma \tag{3.31}$$

$$K_{pp} = \int_\Omega \nabla \mathbf{N}_p^T \frac{\mathbf{k}}{\gamma^w} \nabla \mathbf{N}_p d\Omega \tag{3.32}$$

$$C_{pu} = \int_\Omega \mathbf{N}_p^T \frac{\rho_w S_w + \rho_i S_i}{\rho_w + \frac{S_i}{S_w}\rho_i} \nabla \mathbf{N}_u d\Omega \tag{3.33}$$

$$C_{pp} = \int_\Omega \frac{n(\rho_w - \rho_i)}{\rho_w + \frac{S_i}{S_w}\rho_i} S_p \mathbf{N}_p d\Omega \tag{3.34}$$

$$C_{pp} = \int_\Omega \frac{n(\rho_w - \rho_i)}{\rho_w + \frac{S_i}{S_w}\rho_i} S_T \mathbf{N}_T d\Omega \tag{3.35}$$

$$f_p = \int_\Omega \nabla \mathbf{N}_p^T \rho_w \frac{\mathbf{k}}{\gamma^w} \mathbf{g} d\Omega - \int_{\Gamma_N^p} \mathbf{N}_p^T \mathbf{q}^w d\Gamma \tag{3.36}$$

$$K_{TT} = \int_\Omega \nabla \mathbf{N}_T^T \mathbf{a} \mathbf{N}_T d\Omega + \int_\Omega \nabla \mathbf{N}_T^T \boldsymbol{\lambda} \mathbf{N}_T d\Omega + \int_\Omega \nabla \mathbf{N}_T^T \lambda_e \mathbf{N}_T d\Omega \tag{3.37}$$

$$K_{TT}^s = \int_\Omega \nabla \mathbf{N}_T^T \tau_e \mathbf{a} \cdot \mathbf{a} \nabla \mathbf{N}_T d\Omega + \int_\Omega \nabla \mathbf{N}_T^T \tau_e \mathbf{a} \cdot \boldsymbol{\lambda} \nabla (\nabla \mathbf{N}_T) d\Omega \tag{3.38}$$

$$C_{Tp} = \int_\Omega \mathbf{N}_T^T L_f \xi S_p \mathbf{N}_p d\Omega \tag{3.39}$$

$$C_{Tp}^s = \int_\Omega \mathbf{N}_T^T L_f \xi S_p \tau_e \mathbf{a} \mathbf{N}_p d\Omega \tag{3.40}$$

$$C_{TT} = \int_\Omega \mathbf{N}_T^T (\rho c)_{eff} \mathbf{N}_T d\Omega + \int_\Omega \mathbf{N}_T^T L_f \xi S_T \mathbf{N}_T d\Omega \tag{3.41}$$

$$C_{TT}^s = \int_\Omega \mathbf{N}_T^T (\rho c)_{eff} \tau_e \mathbf{a} \mathbf{N}_T d\Omega + \int_\Omega \mathbf{N}_T^T L_f \xi S_T \tau_e \mathbf{a} \mathbf{N}_T d\Omega \tag{3.42}$$

$$f_t = \int_{\Gamma_N^T} \mathbf{N}_T^T \mathbf{q}^T d\Gamma + \int_{\Gamma_N^T} \mathbf{N}_T^T \lambda_e T_e d\Gamma \tag{3.43}$$

$$\frac{\delta \boldsymbol{\sigma}}{\delta p^w} = S_p(p_i - p) - (S_w + S_i \frac{\rho_i}{\rho_w}) \tag{3.44}$$

$$\frac{\delta \boldsymbol{\epsilon}^{ph}}{\delta p^w} = \frac{n(\rho_i - \rho_w)S_p}{3(\rho_w S_w + \rho_i S_i}) \tag{3.45}$$

$$\frac{\delta \boldsymbol{\sigma}}{\delta T} = S_T(p_i - p) + S_i \rho_i \frac{L_f}{T} \tag{3.46}$$

$$\frac{\delta \boldsymbol{\epsilon}^{ph}}{\delta T} = \frac{n(\rho_i - \rho_w)S_T}{3(\rho_w S_w + \rho_i S_i}) \tag{3.47}$$

Chapter 4

Isogeometric Analysis

Most FEM (Finite Element Method) programs in use today, applies Lagrange's polynomials as basis functions. The code used in this thesis does however rely on splines as the basis functions. This chapter will briefly introduce splines for FEA (Finite Element Analysis). IGA (IsoGeometric Analysis) is thoroughly presented in other literature, such as Cottrell et al. (2009).

4.1 Introduction

Splines are a collection of polynomial functions, joined at the ends. Splines are for example commonly used CAD(computer aided design), and to create graphics in computer games. Splines is hence nothing new, but using splines as basis functions in FEA is not widespread. The overall performance of splines versus Lagrange's is far too complex to discuss in this thesis. There are however some advantages of splines that will be pointed out and illustrated.

One of the advantages of splines, is the possibility to use the same basis functions to create both the geometry and solution fields. Conventional FEM will need to convert data between FEM and CAD, increasing the simulation time. As the name implies for isogeometric analysis, splines represent CAD and FEM one to one, removing the necessity to convert data.

Another advantage lays in the problem of discontinuities, both in the calculation and in the geometry. Splines can be created to ensure both continuity and discontinuity, which are especially important in flow problems. Conventional finite element analysis has however several methods for reducing this problem, for example smoothing by point averaging (Bell

(2013)).

4.2 Splines

Splines comes in many forms, but the focus of this thesis is B-Splines (Benzier Splines) and NURBS (Non-Uniform Rational B-Splines). The basis for creating splines is a knot vector, and the properties of the spline is determined by the entries (knots) in the knot vector. The knot vector is defined as Ξ=[ξ_1 ξ_2...ξ_n], where Ξ is non-decreasing. Each knot represents a position in the knot space, and the knot may be repeated in the knot vector. If the knots are not equally spread, the knot vector is considered non-uniform.

The knot vector is used to create a set of constant functions, either equal to 1 or 0. A function is 1 of between the knots, and zero elsewhere, as shown in equation 4.1. These functions are used in the Cox-de Boor formula (equation 4.2) to create the desired polynomial degree.

$$N_{i,0}(\xi) = \begin{cases} 1 & \text{if } \xi_i \leq \xi < \xi_{i+1} \\ 0 & \text{otherwise} \end{cases} \tag{4.1}$$

$$N_{i,p}(\xi) = \frac{\xi - \xi_i}{\xi_{i+p} - \xi_i} N_{i,p-1}(\xi) + \frac{\xi_{i+p+1} - \xi}{\xi_{i+p+1} - \xi_{i+1}} N_{i+1,p-1}(\xi) \tag{4.2}$$

A B-spline curve is then created by weighing the basis functions with the control points, as shown in equation 4.3.

$$Curve = \sum_{i=0}^{n} C_i N_{i,p} \tag{4.3}$$

Using python, equations 4.1 to 4.3 implemented and plotted. The top plot in figure 4.1 show the constant functions from equation 4.1, and the next two plots show the linear and quadratic expansion using equation 4.2. Figure 4.2 shows a set of control points and the correlating linear and quadratic B-Splines.

We observe that in the knot vector $\Xi = [0,0,0,0.25,0.5,0.75,1,1,1]$, 0 is repeated 3 times, making $N_{1,2}$ C^{-1} continues. Due to the nature of equation 4.1 and 4.2, a set of basis functions is C^{p-m} continues. Where p is the polynomial degree, and m is highest number of repeated knots. It is possible to use this to create discontinues functions, for example to represent a impermeable crack. To create a discontinuity in a given knot, one simply repeats the knot so that $C^{p-m} = C^{-1}$ in the knot. An example of continuity and knot insertion is shown in 4.3.

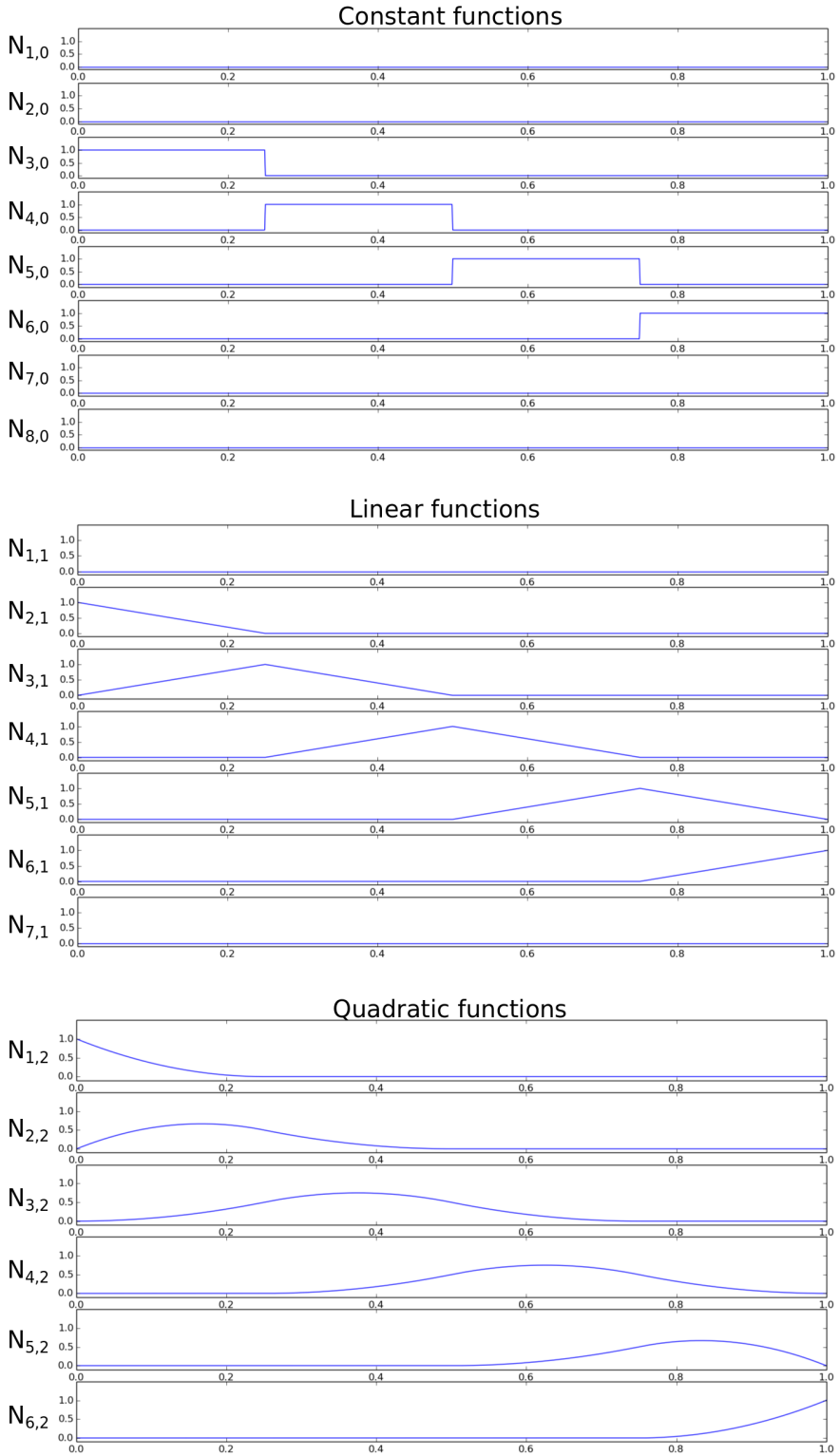

Figure 4.1: Basis functions for $\Xi = [0,0,0,0.25,0.5,0.75,1,1,1]$

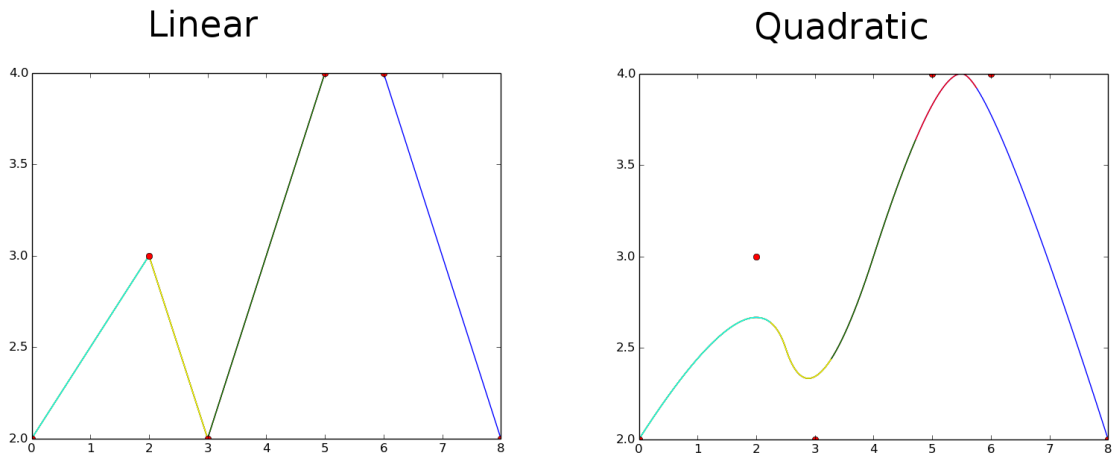

Figure 4.2: Example of splines used to create a curve with a given set of points

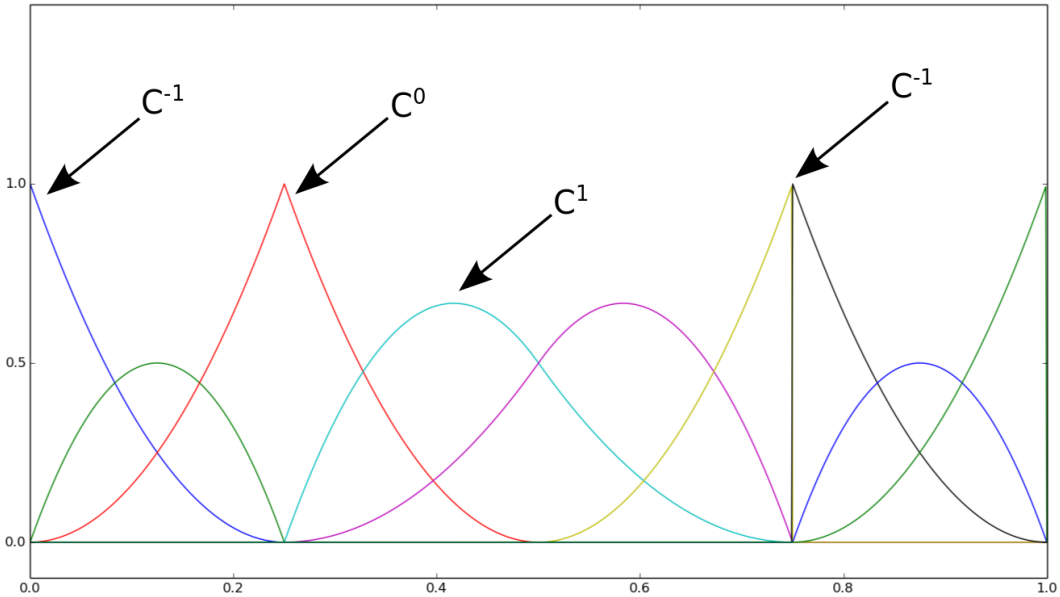

Figure 4.3: Continuity for $\Xi = [0,0,0,0.25,0.25,0.5,0.75,0.75,.75,1,1,1]$

4.3 Relation to FEM and CAD

The geometry in CAD and the fields in FEM, is created simply by expanding the previous sections to 2 or 3 dimensions. It is important to understand that the foundation of IGA, is swapping out the Lagrange's basis functions with splines. A B-splines surface is generated as shown in equation 4.4.

$$Surface = \sum_{i=0}^{n} C_{i,j} N_{i,p} N_{j,q} \tag{4.4}$$

In case of complex geometries, it is sometimes convenient to use NURBS. NURBS are created by projecting a B-spline, a 2D NURBS would for instance be created from a 3D B-spline. An example of applying NURBS in CAD is shown in Borden et al. (2011), and a selection of figures from this text is presented in 4.4. A important difference from convectional FEM, is that the elements exist in the knot space, explaining why "elements" overlap in the CAD geometry.

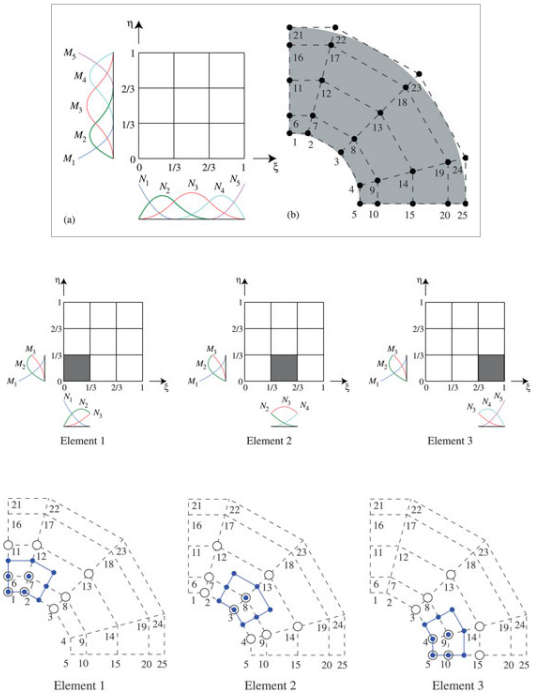

Figure 4.4: Applying NURBS to 2-D geometry, from Borden et al. (2011)

A geometry can be separated in patches, where each patch has its own knot space. The patches can be joined at the border, normally with C^0 continuity. A large amount of patches would hence reduce the advantage of continuity in IGA.

Chapter 5

THM Model for Saturated Soils: Numerical Studies

5.1 Thermal Consolidation

This section will model the effects of thermal expansion and consolidation, and evaluate the results based on similar models using conventional FEM. The example is similar to those presented in Aboustit et al. (1985) and Lewis and Schrefler (1998), and these papers are hence used as a reference.

5.1.1 Model

The geometry, mesh and boundary conditions are as shown in figure 5.1. As explained in chapter 4, elements does not exist in a similar way for IGA. Instead of elements, it is the control points (nodes) that are displayed in figure 5.1. All edges are impermeable and adiabatic, *except* the top. The top is loaded with both a mechanical and a thermal load, and all initial fields are zero. The values in table 5.1 are chosen to make sure the thermal expansion effects the solution when most of the draining deformation is complete. The chosen time stepping is shown in table 5.2.

5.1.2 Results

The results are presented in figure 5.2. Temperature, deformation and pore pressure development is plotted for different heights.

What	Symbol	Value	Unit
Porosity	n	0.4	-
Young's modulus	E	6e6	Pa
Poisson's ratio	ν	0.4	-
Water bulk modulus	K_w	1e99	Pa
Solid bulk modulus	K_s	1e99	Pa
Medium bulk modulus	K_0	0	Pa
Water density	ρ_w	1000	Kg/ m³
Solid density	ρ_s	2000	Kg/ m³
Permeability	K	1.11e-9	m/s
Water heat capacity	c_w	200	J/KgK
Solid heat capacity	c_s	66	J/KgK
Water thermal conductivity	λ_w	0.6	W/mK
Solid thermal conductivity	λ_s	0.0006	W/mK
Volumetric expansion	β	9e-7	-

Table 5.1: Input values for the thermal consolidation

Nr. of steps	Step size
10	0.01
10	0.1
10	10
10	100
20	1000

Table 5.2: Time stepping for the thermal consolidation

5.1.3 Discussion

Figure 5.2 clearly shows how the model deforms when draining, and how the thermal expansion counteracts this effect. The results are highly comparable with the results in Aboustit et al. (1985) and Lewis and Schrefler (1998), and there was no oscillation in temperature or pore pressure at the first time step. This overall indicates that the models yields good physical results.

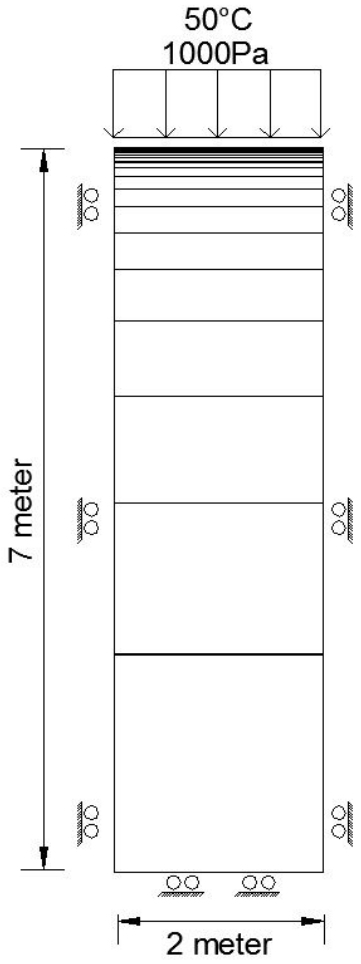

Figure 5.1: Model and mesh for the one dimensional thermal consolidation

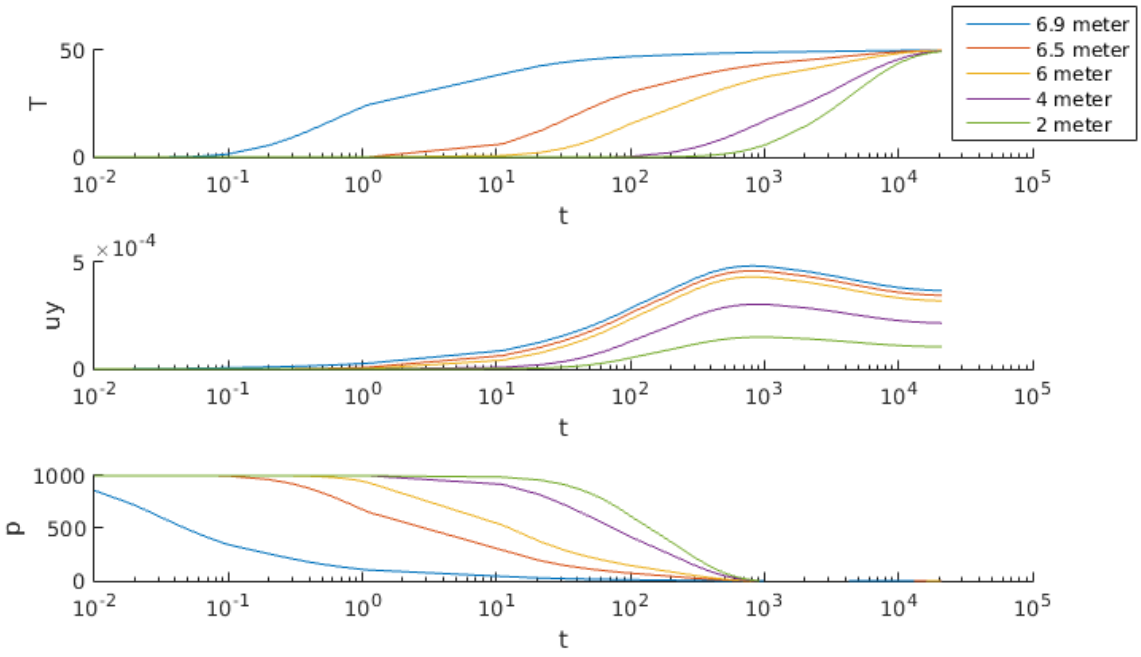

Figure 5.2: Temperature, deformation and pore pressure with time

5.2 Thermal Loading with Discontinuities

Discontinuities can be difficult to handle in conventional FEM, leading to the development of XFEM(Extended Finite Element Method). The XFEM is based on changing the basis functions around a discontinuity, as further explained in Khoei et al. (2012). This, and the following sections investigates if isogeometric analysis, *without any alteration*, can represent discontinuities as well as XFEM. The example problems are taken from, and compared with Khoei et al. (2012).

5.2.1 Model

The geometry is shown in figure 5.3, and the material parameters are presented in table 5.3. The red line indicates the crack/discontinuity, and both the top and bottom is adiabatic. A thermal load of ±50 degree Celsius is applied at the sides, with all initial field equal to zero. The calculations is computed with two different meshes, one uniformly distributed, and one with finer mesh close to the discontinuity (graded). The time stepping is presented in table 5.4, resulting in a total time of 100 seconds.

What	Symbol	Value	Unit
Porosity	n	0.0	-
Young's modulus	E	9e6	Pa
Poisson's ratio	ν	0.3	-
Water density	ρ_w	1000	Kg/ m³
Solid density	ρ_s	2000	Kg/ m³
Solid heat capacity	c_s	100/500	J/KgK
Solid thermal conductivity	λ_s	1000	W/mK
Volumetric expansion	β	0.3e-6	-

Table 5.3: Input values for the thermal loading

Nr. of steps	Step size
100	0.1
90	1

Table 5.4: Time stepping for the thermal loading

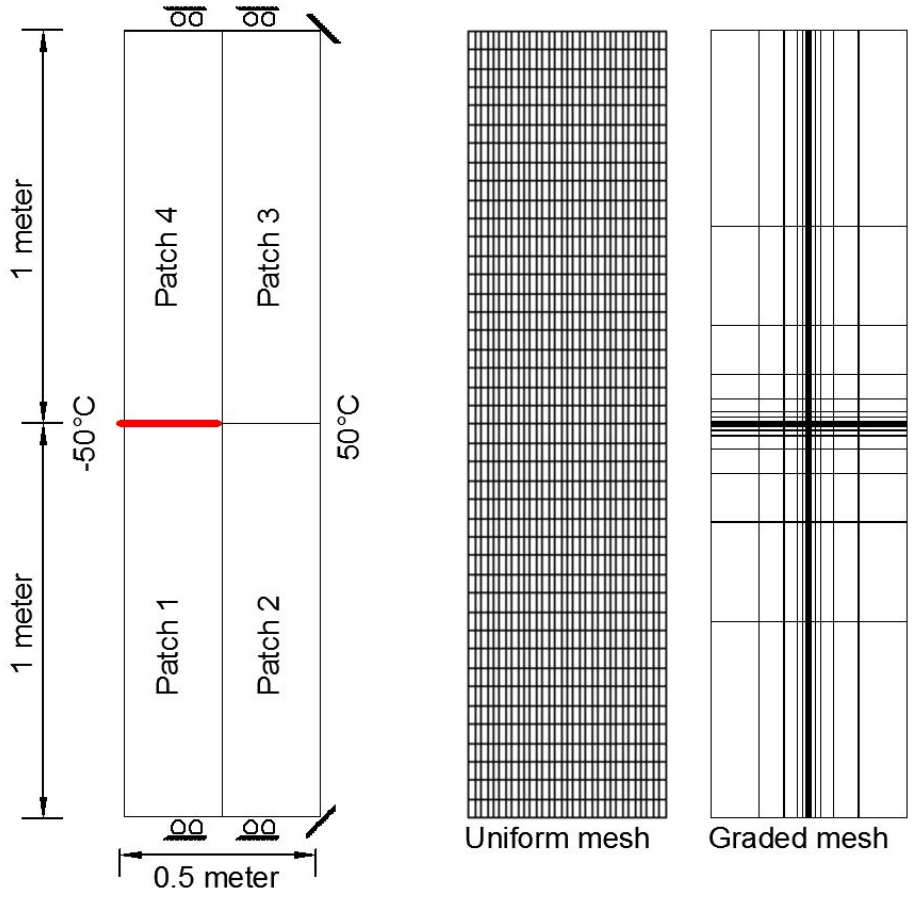

Figure 5.3: Model and mesh for the thermal loading with discontinuity

5.2.2 Results

The temperature and displacements fields after 100 seconds (steady-state) is shown in figure 5.4. The temperature profile from the crack towards the right edge is plotted to the left in figure 5.5, and compared to the solution in Khoei et al. (2012), also corresponding to the analytical solution. The temperature gradient in x-direction will reach $200°C/m$ when in steady state, and is hence a good indicator of when steady state is reached. The temperature gradient is plotted with time to the right in figure 5.5. The specific heat capacity is not given in Khoei et al. (2012), the simulation was hence executed with different specific heat capacities (as indicated in the figure legend). The stresses in y-direction around the crack tip is plotted for different mesh and polynomial degree in figure 5.6. The scale is chosen to give a good representation close to the crack tip, resulting in much of the left part being out of bound (represented by a gray color). The same stresses are plotted for a distance Δ in x-direction from the crack tip, with the time in figure 5.7. Since the crack tip is a singularity point, the stresses are expected to increase to infinity, hence comparison with Khoei et al. (2012) is done at distance Δ from the crack.

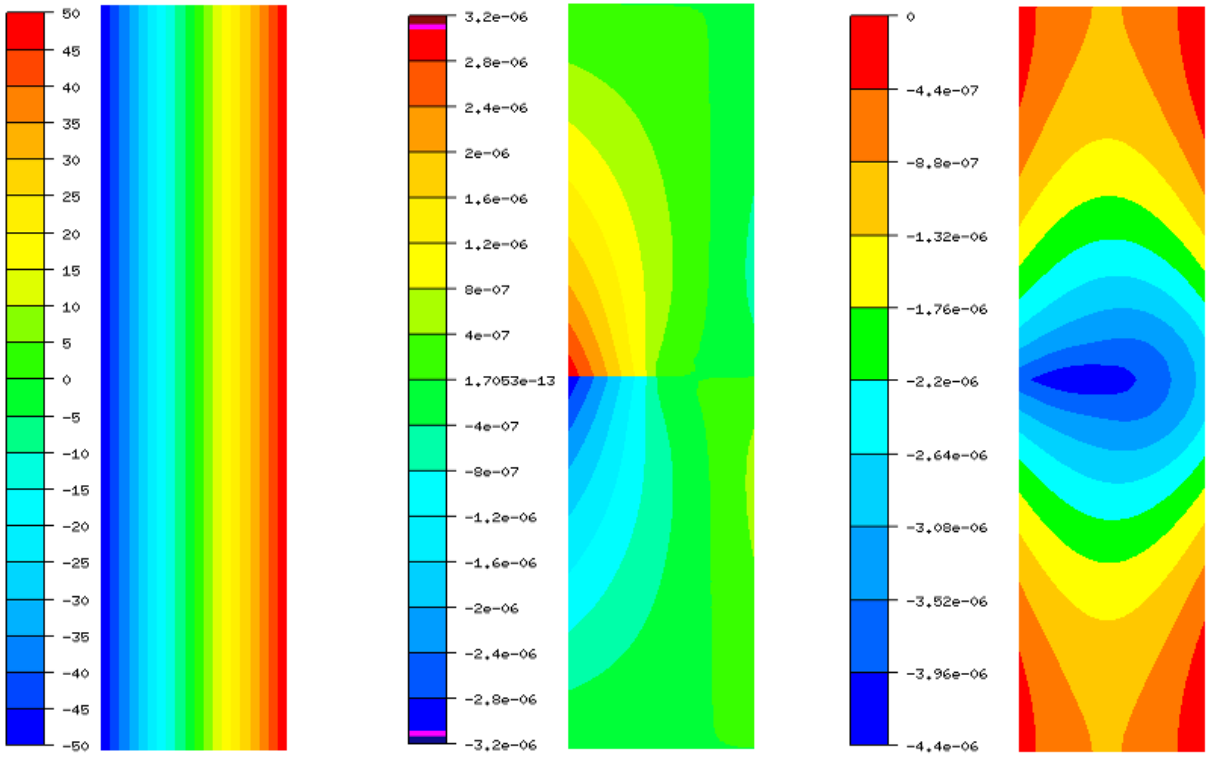

Figure 5.4: Temperature(left), y-displacement(centre) and x-displacement(right) at stady state

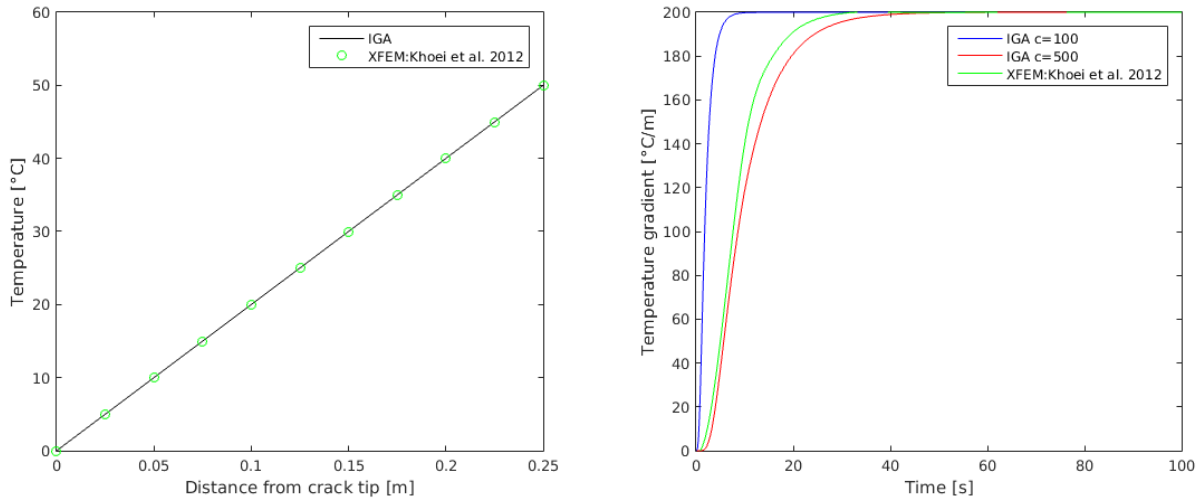

Figure 5.5: Temperature profile from crack tip at 100 seconds, and development of temperature gradient at crack tip with time

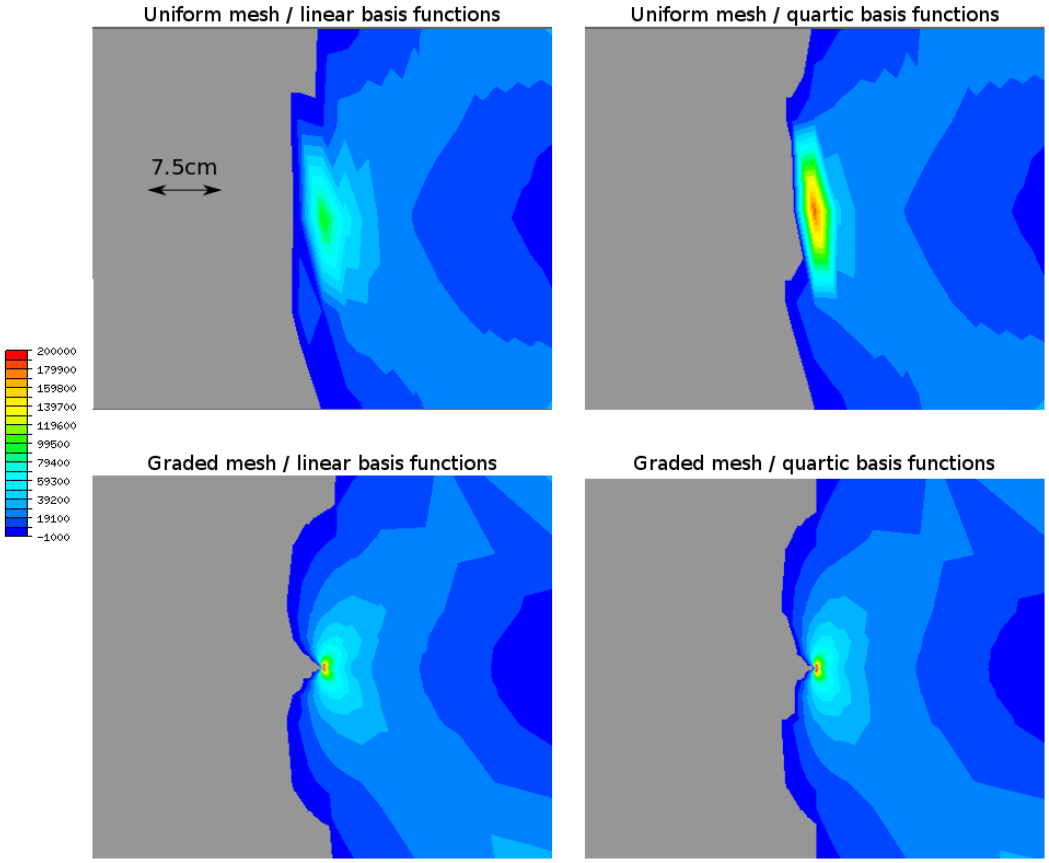

Figure 5.6: Stress in the y-direction around the crack tip. For scale is set for best visibility of the singularity, the gray area is out of bound.

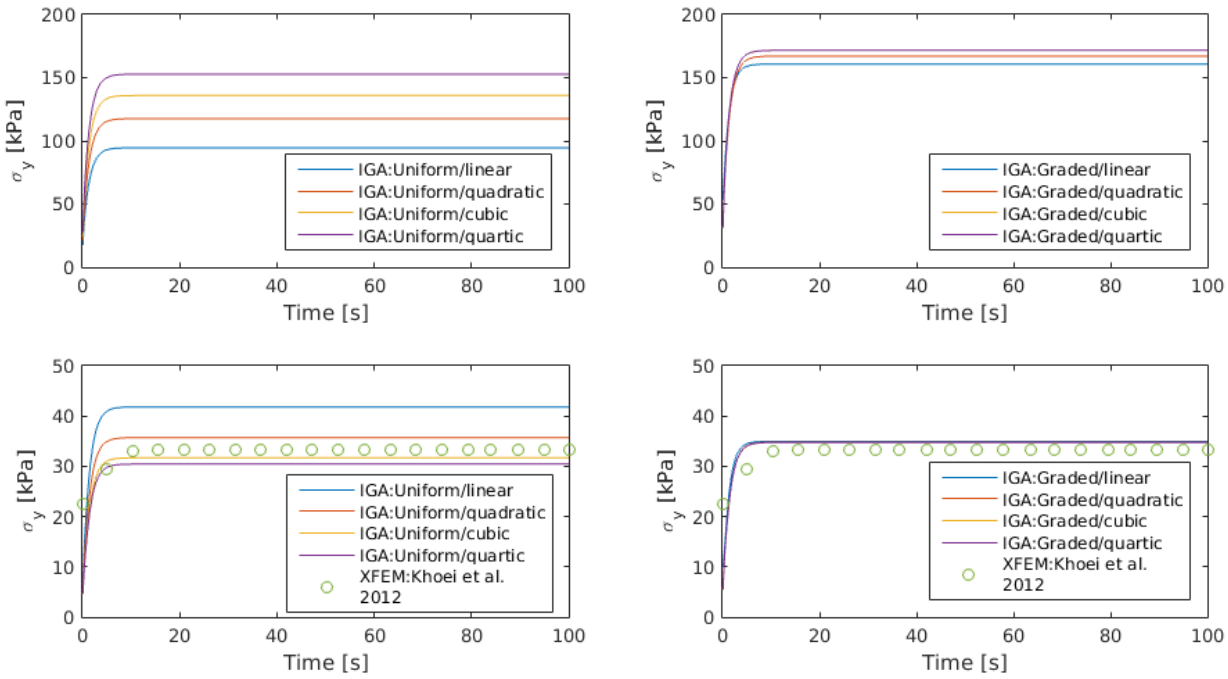

Figure 5.7: Stress in the y-direction plotted for uniform and graded refinement, and polynomial degree. The distance from the crack is 10mm and 37.5mm for the top and bottom plots respectively.

5.2.3 Discussion

The steady state fields are highly comparable with Khoei et al. (2012), and the steady state temperature field is matched exactly. The lack of information about heat capacity makes the convergent rate hard to compare, a heat capacity of 500J/KgK does however yield similar results. The primary solutions does overall compare well.

The calculations with varying refinement and polynomial degree, shows as expected a increased stress concentration with polynomial degree. An exact distance from the crack is not specified, but a chosen distance Δ of 37.5mm yield comparable results with Khoei et al. (2012), and the plots clearly show increasing stress closer to the singularity. This indicates that the secondary solutions is both realistic and comparable to Khoei. It is however interesting to note that the uniform and graded mesh does not seam to converge towards the exact same solution, when the polynomial degree is raised. This problem probably occurs because the uniform mesh is too course around the singularity, to get the expected convergence and convergence rate.

5.3 Ground Water Flow with Discontinuities

5.3.1 Model

The model represents a dam seepage problem, with geometry and mesh as shown in figure 5.8. The red lines indicates impermeable boundaries and discontinuities, and material properties is shown in table 5.5. The time stepping is presented in table 5.6, resulting in a total time of 110 seconds.

What	Symbol	Value	Unit
Porosity	n	0.3	-
Young's modulus	E	9e9	Pa
Poisson's ratio	ν	0.4	-
Water bulk modulus	K_w	2e9	Pa
Solid bulk modulus	K_s	1e20	Pa
Medium bulk modulus	K_0	0	Pa
Water density	ρ_w	1000	Kg/ m³
Solid density	ρ_s	2000	Kg/ m³
Permeability	K	1e-5	m/s

Table 5.5: Input values for ground water flow

Nr. of steps	Step size
100	0.1
100	1

Table 5.6: Time stepping for ground water flow

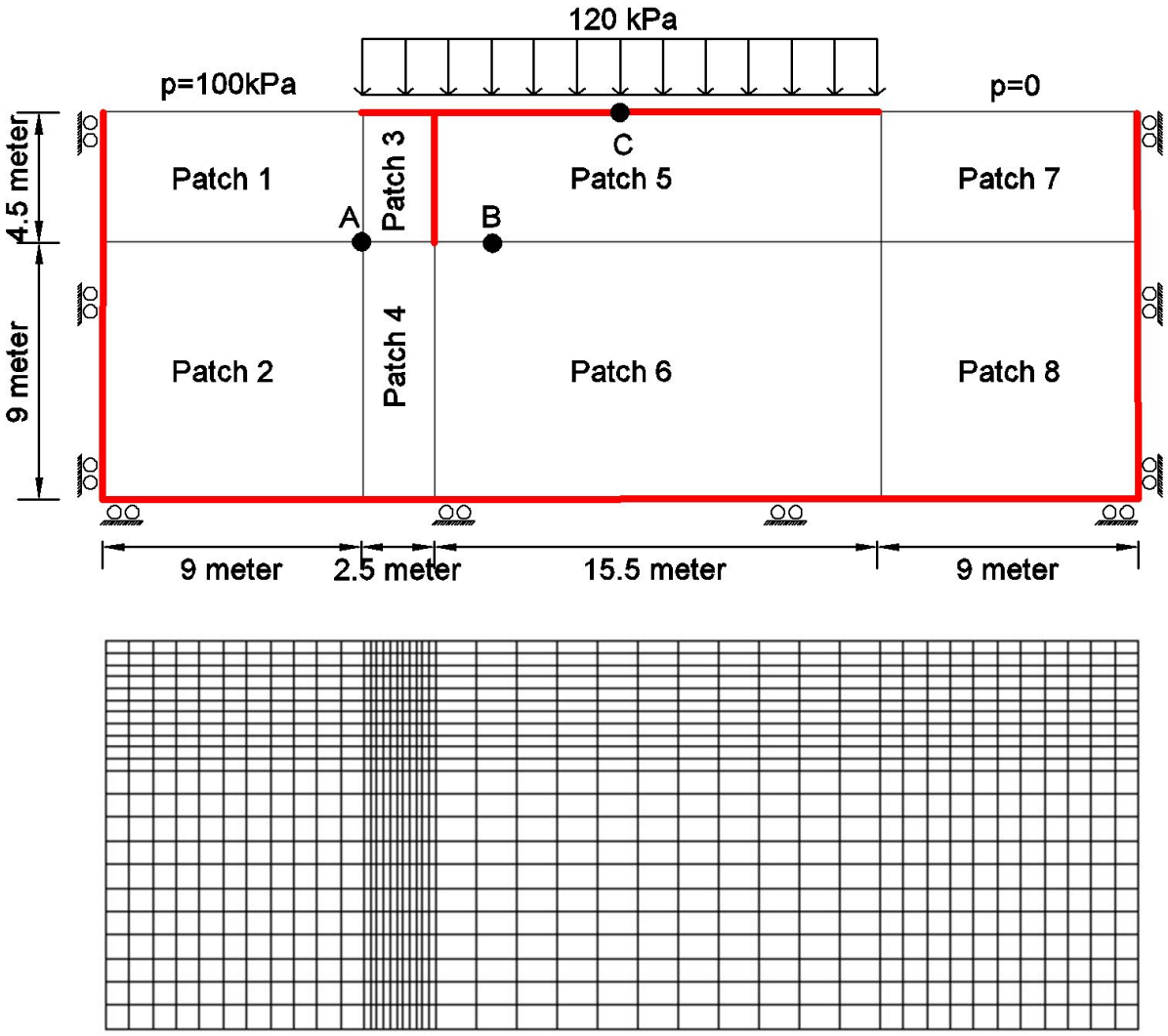

Figure 5.8: Model and mesh for ground water flow with discontinuity

5.3.2 Results

The pore pressure profile at 5, 10 and 110 seconds is presented in figure 5.9. The pore pressure and settlement for point A,B and C is presented and compared with Khoei et al. (2012) in figure 5.10. Since Khoei did not specify the point for pore pressure gradient, the pore pressure and pore pressure gradient is plotted and compared using the closed node the left of the singularity in figure 5.11. The results are hence not directly comparable with the results presented by Khoei.

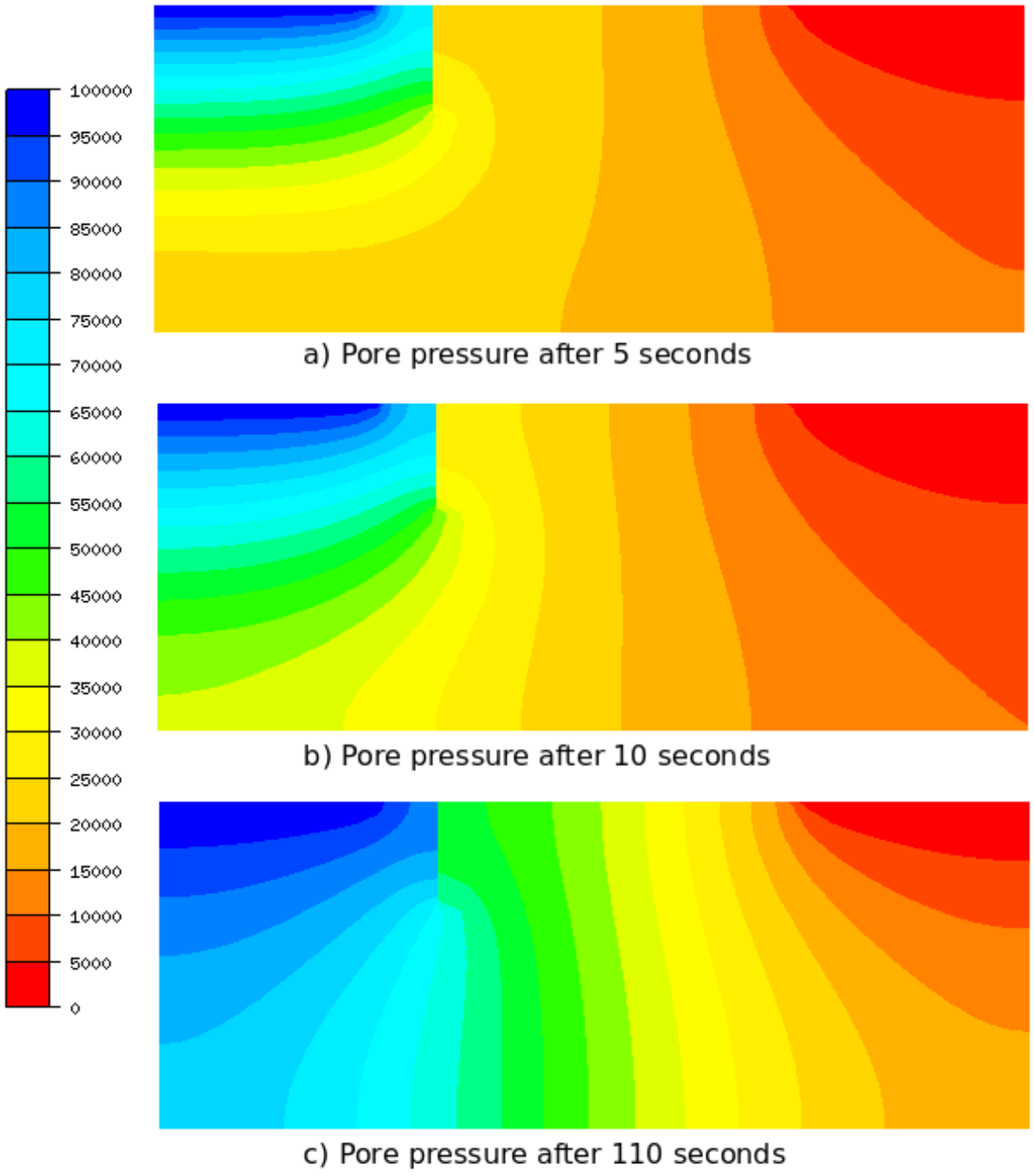

Figure 5.9: Pore pressure after 5, 10 and 110 seconds

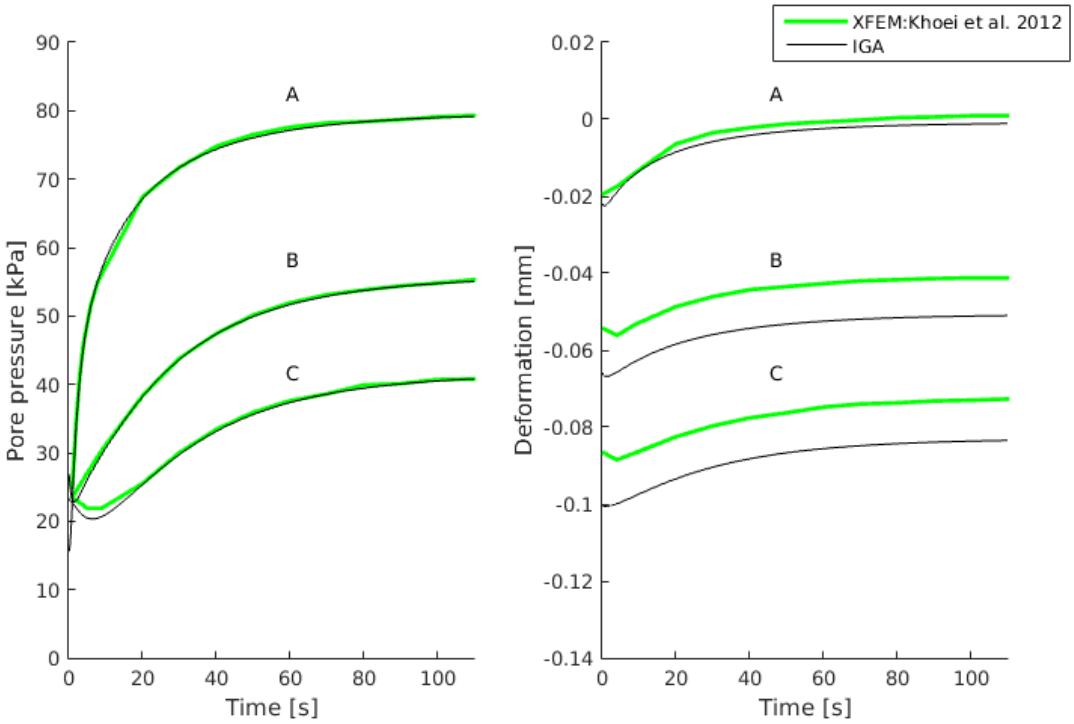

Figure 5.10: Pore pressure and deformation development

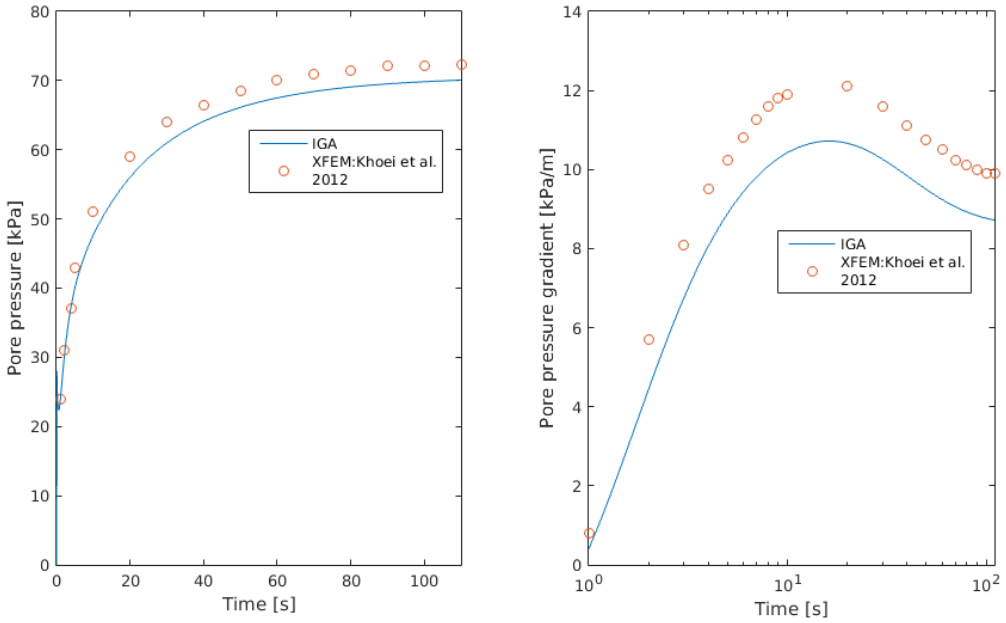

Figure 5.11: Pore pressure and pore pressure gradient near the singularity

5.3.3 Discussion

Both figure 5.9 and 5.10 shows almost identical pore pressure development as Khoei. It also show a similar settlement development, but in both point B and C, IGA estimates 15-20% higher initial deformation. Considering the differences in for example load distribution, the result is within the expected deviation.

Due to the vague description of the point for pore pressure gradient, comparing is difficult. The point node directly to the left (approximately 0.2m), does however yield a comparable result. The model does as expected show a rapid increase in flow near the tip of the discontinuity, and the pore pressure gradient will hence vary greatly near the tip.

The simulation is overall realistic and comparable to the results in Khoei et al. (2012).

5.4 Fully Coupled Model with Discontinuities

5.4.1 Model

This problem consist of two 10x10m models, with a discontinuity with an angle of 0 and 45 degree, as shown in figure 5.12. The mesh is graded, and the material properties are displayed in table 5.7. The time stepping is shown in table 5.8, resulting in a total time of 1e5 seconds. Since the code does not yet support Neumann boundary conditions for pore pressure and temperature, the Nuemann pore pressure boundary was approximated by a linear increasing Dirichlet boundary until t=1e4.

What	Symbol	Value	Unit
Porosity	n	0.3	-
Young's modulus	E	6e6	Pa
Poisson's ratio	ν	0.4	-
Water bulk modulus	K_w	2e9	Pa
Solid bulk modulus	K_s	1e20	Pa
Medium bulk modulus	K_0	0	Pa
Water density	ρ_w	1000	Kg/ m³
Solid density	ρ_s	2000	Kg/ m³
Permeability	K	1.08e-5	m/s
Water heat capacity	c_w	4200	J/KgK
Solid heat capacity	c_s	878	J/KgK
Water thermal conductivity	λ_w	837	W/mK
Solid thermal conductivity	λ_s	837	W/mK
Volumetric expansion	β	9e-8	-

Table 5.7: Input values for coupled discontinuity

Nr. of steps	Step size
10	10
10	90
10	900
10	9000

Table 5.8: Time stepping for ground water flow

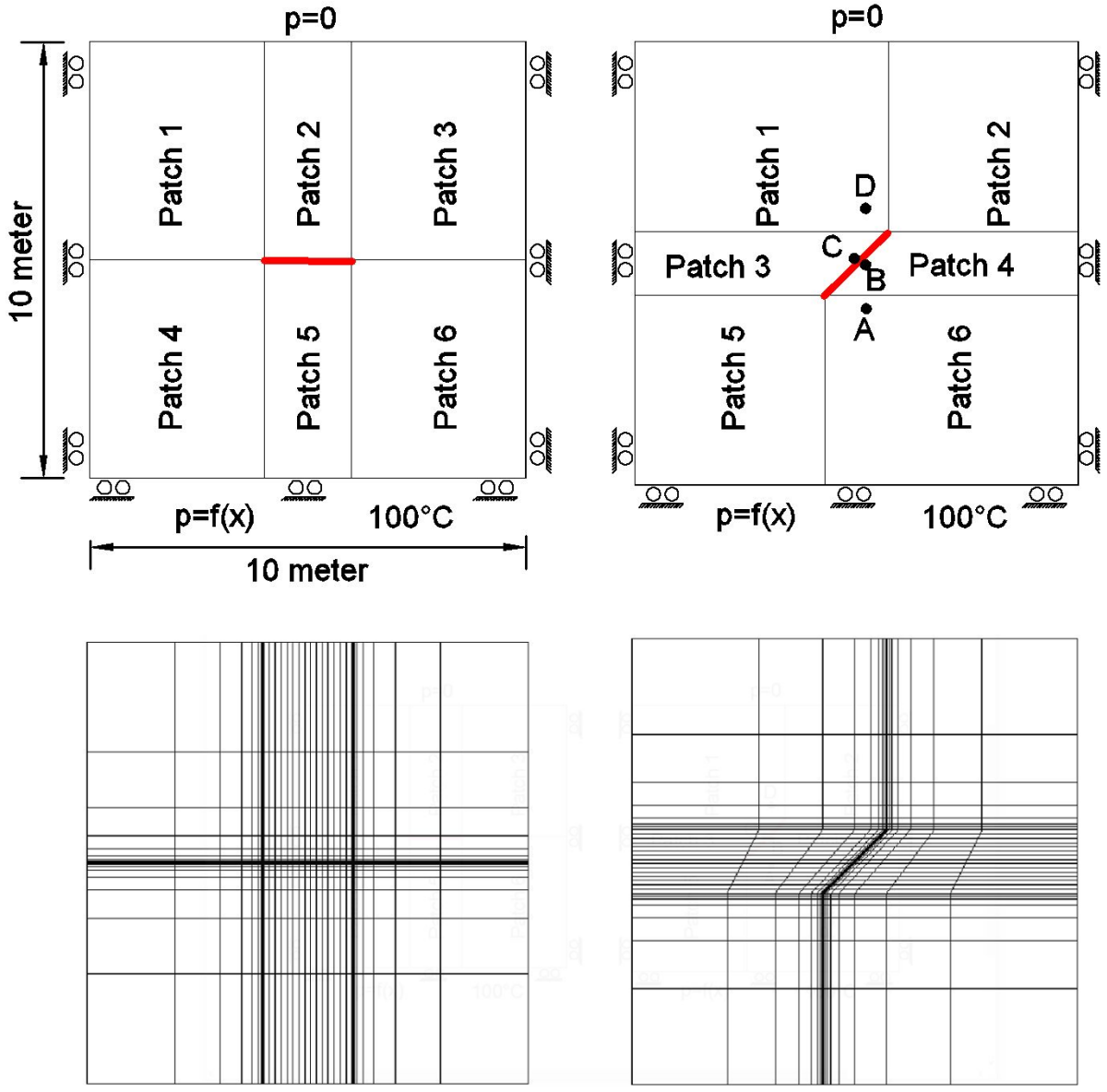

Figure 5.12: Model and mesh for the fully coupled problem

5.4.2 Results

The approximation of the Neumann boundary is shown and compared with the exact boundary condition in figure 5.13. The pore pressure development is plotted for point A, B, C and D, and compared with Khoei et al. (2012) in figure 5.14. The difference in temperature between the two crack tips are plotted and compared with Khoei in figure 5.15. The pore pressure and temperature are plotted in the center of the crack, and gradient normal to the crack is calculated and plotted in 5.16. The code was modified to output the gradient in x and y-direction, and the gradient in the normal direction was calculated using the dot product on the normal vector and the pressure gradients. For a smoother curve in figure 5.16, the time steps was increased from 10 to 30 in the area between t=1e2 and t=1e4.

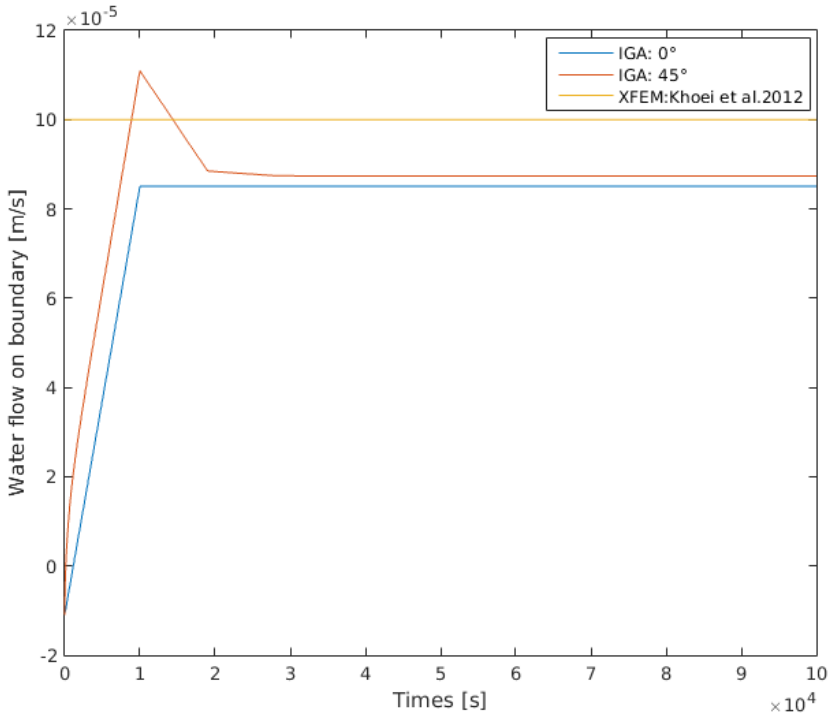

Figure 5.13: Result of approximation by Dirichlet boundary

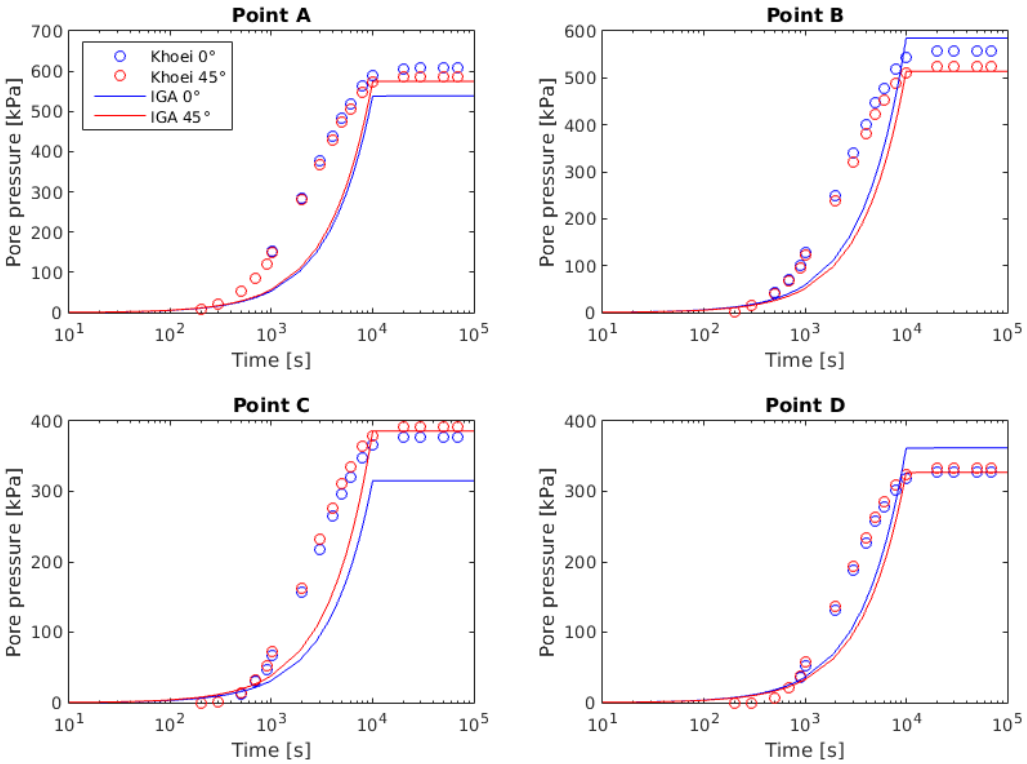

Figure 5.14: Pore pressure development at different points in the model

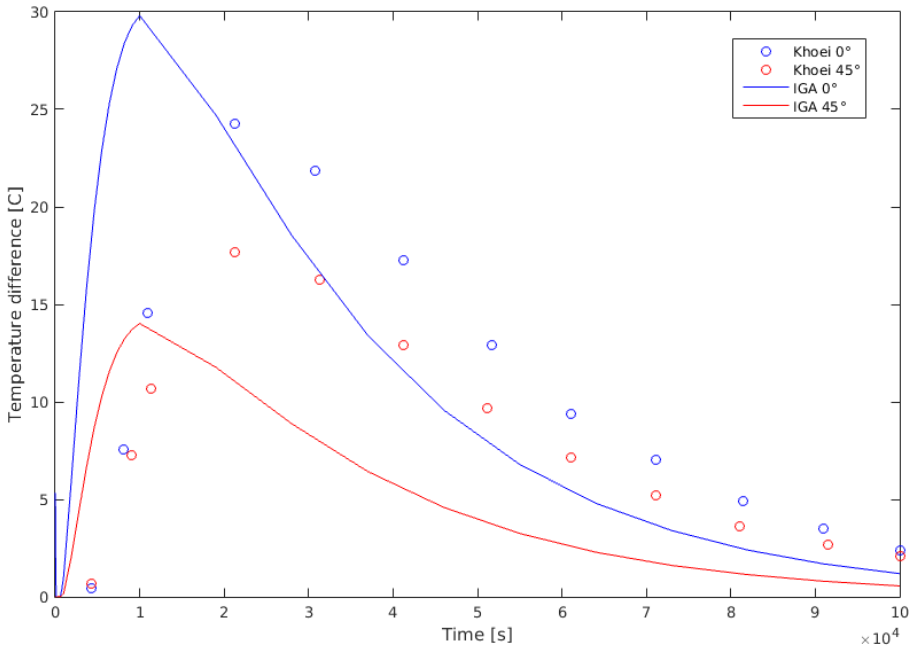

Figure 5.15: Temperature difference between the crack tips

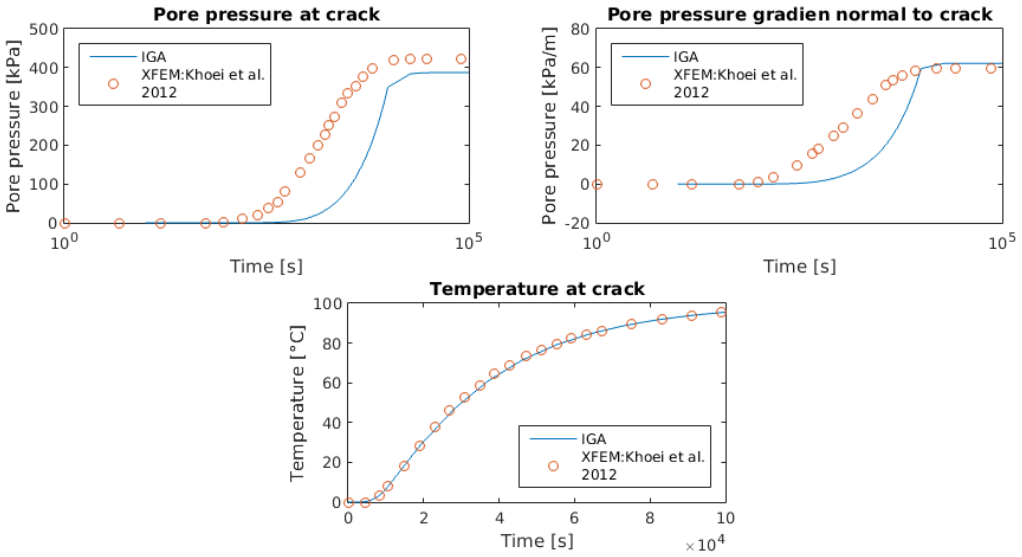

Figure 5.16: Temperature and pore pressure development for 45 degree crack

5.4.3 Discussion

As clearly visible in figure 5.13, the approximation yields a much lower inflow, and hence a slower convergence than Khoei et al. (2012). All plots considering pore pressure does show a much slower convergence, however it does overall converge towards the approximately same values as in Khoei. The temperature development is almost exactly the same as in Khoei, and the temperature difference is showing the same tendency. The model is indicating singularities for both pore pressure and temperature at the crack tips, and increasing polynomial degree results in increased gradients at the crack tips.

Due to the approximation of the Neumann boundary, the IGA does not represent an exact match. The calculations does however give results in approximately the same scale, and shows the same trends. The results show slower convergence time for IGA, but this is expected from the approximation. The overall results does indicate that the results is realistic, and similar to the results by Khoei.

Chapter 6

THM Model for Ground Freezing: Numerical Studies

6.1 Parametric Study

This section contains investigations on the parameters used in the ground freezing model, and has two main goals. The first part consist of observing the parameters effect on the solution using sets of phase change parameters that is previously shown to have good convergence properties. The second parts consist of realistic phase change parameters, based on the different soil types.

6.1.1 Inital Model

The study is conducted on a one dimensional heave problem, altering only the relevant parameter. The model and mesh is presented in figure 6.1, with both sides impermeable and adiabatic. The initial model parameters are shown in table 6.1. The time stepping is presented in table 6.2, and the simulation ends at 120 days.

The limits for the phase change parameters are chosen so that the model converges without significant alteration to the model, and the material parameters are chosen to represent typical limits of what to be expected in a silt or silty clay. It is important to note that all parameters are treated separately, although several parameters are closely related (such as porosity and permeability). A summary of the parameter variations are shown in table 6.3.

Property	Symbol	Value	Unit
Porosity	n	0.44	-
Solid density	ρ_s	2650	Kg/ m³
Water density	ρ_w	1000	Kg/ m³
Ice density	ρ_i	910	Kg/ m³
Young's modulus of soil	E_s	3e6	Pa
Young's modulus of ice	E_i	9.1e9	Pa
Poisson's ratio for soil	ν_s	0.2	-
Poisson's ratio for ice	ν_i	0.4	-
Strength model parameter	η	1	
Permeability	K	1e-5	m/s
Saturation model parameter 1	S^α	0.1	Pa^{-1}
Saturation model parameter 2	S^β	2.5	-
Saturation model parameter 3	S^γ	8	-
Permeability model parameter	m^p	0.87	-
Solid heat capacity	c_s	800	J/KgKs
Water heat capacity	c_w	4190	J/KgKs
Ice heat capacity	c_i	2095	J/KgKs
Solid thermal conductivity	λ_s	1.5	W/mK
Water thermal conductivity	λ_w	0.6	W/mK
Ice thermal conductivity	λ_i	2.2	W/mK
Latent heat of fusion	L_f	334e3	J/kg

Table 6.1: Input values for initial model

Start	End	Nr. of steps
0	0.1	30
0.1	1.1	30
1.1	101.1	40
101.1	1101.1	30
1101.1	21101.1	30
21101.1	86400	30
86400	1037e4	119

Table 6.2: Time stepping for initial model

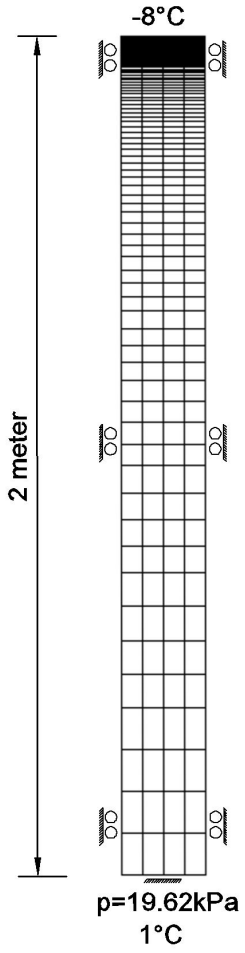

Figure 6.1: Model and mesh for parametric study

Parameter	test 1	test 2	test 3	test 4	test 5
m^p [-]	0.25	0.5	0.87	1	1.25
η [-]	0.2	0.4	0.6	0.8	1
S^α $[MPa^{-1}]$	0.05	0.075	0.1	0.125	0.15
S^β [-]	1.5	2.0	2.5	3.0	3.5
S^γ [-]	4	6	8	12	16
ρ_s [kg/m^3]	2500	2600	2650	2700	2800
c_s [J/kg]	600	700	800	900	1000
λ_s [W/mK]	0.5	1.5	2.5	3.5	4.5
k [m/s]	1e-2	1e-4	1e-5	1e-7	1e-9
E [MPa]	0.5	1	3	15	75
n [-]	0.2	0.3	0.44	0.5	0.6
μ [-]	0.15	0.2	0.25	0.3	0.33

Table 6.3: Parameter values

6.1.2 Previous Experimental Data on the Phase Change Parameters

A literature search on the permeability parameter m^p, the strength parameter η, and the saturation curve parametersS^α, S^β and S^γ, shows that there is limited information about these parameters. A relatively broad study water/ice content found in Smith and Tice (1988) was adopted to determine the saturation curves. From the study, five saturation curves was estimated to represent the span from fine clay to sand. The curves are plotted and shown in figure 6.2 and table 6.4.

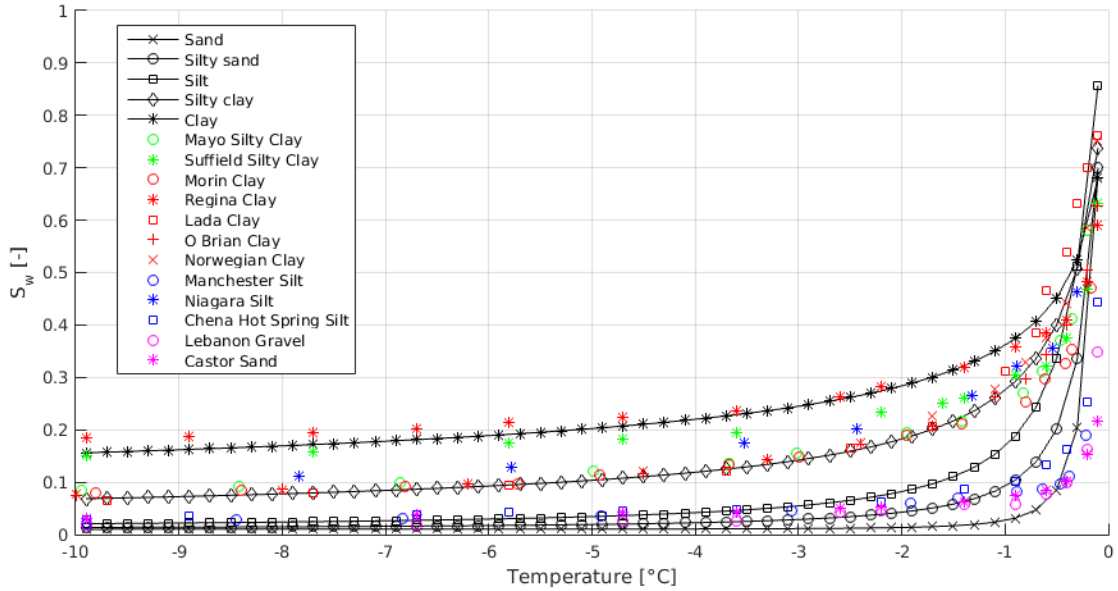

Figure 6.2: Chosen saturation curves and experimental data from Smith and Tice (1988).

Nr.	S^α [MPa^{-1}]	S^β [-]	S^γ [-]	Representation
1	5	1.8	1.3	Sand
2	5	1.4	1	Silty sand
3	4	1.7	0.7	Silt
4	5	1	0.7	Silty clay
5	8	0.7	0.6	Clay

Table 6.4: Model parameters for chosen saturation curves

Experimental data collected in Andersland and Ladanyi (2004) is used to compare with the permeability model. The permeability model is based on saturation curve nr. 3. Since the reduction in permeability decreases very rapidly, the results are plotted for temperature for 0 to -1 degree Celsius in figure 6.3.

Since there exist very little data on the strength model, the strength parameter is compared with empirical formulas presented in Andersland and Ladanyi (2004) and with test on

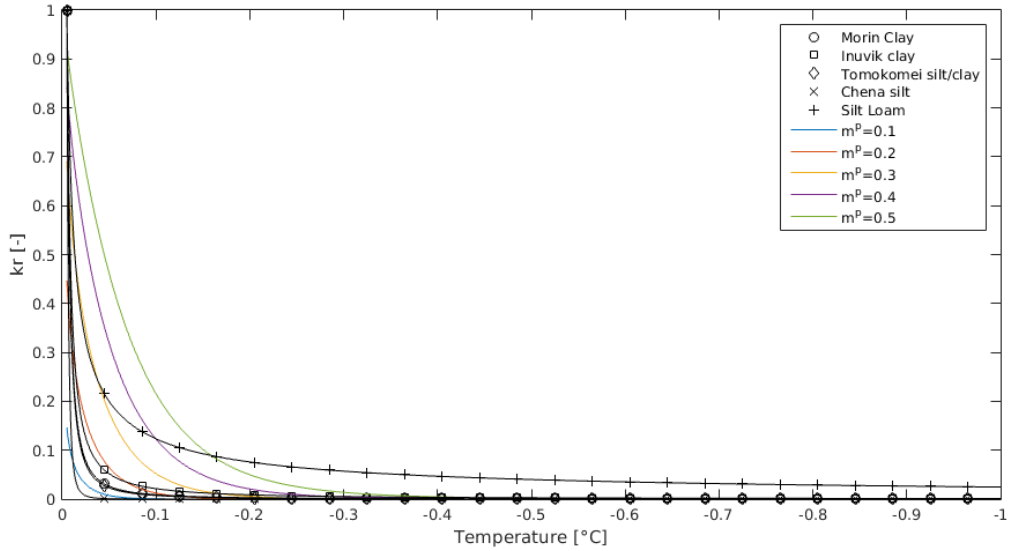

Figure 6.3: Permeability parameters compared with experimental data from Andersland and Ladanyi (2004)

a silt from Zhu and Carbee (1984) in figure 6.4. The upper and lower limits represents strain rates of 5.7e-3s^{-1} and 1.1e-6s^{-1} respectively, the ground freezing model used does however no adjust stiffness with strain rate.

Due to the lack of information about correlation between saturation curves, the strength model and the permeability model, m^p and η are kept constant at 0.4 and 2 respectively during simulations with varying saturation curves.

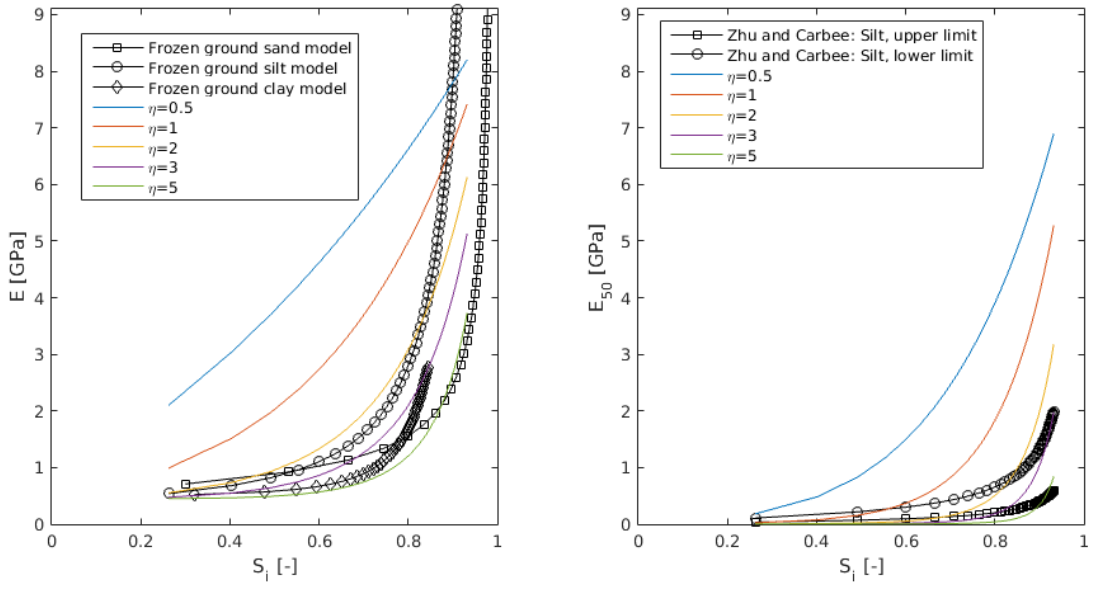

Figure 6.4: Strength parameters compared with empirical formals and silt experiment

6.1.3 Results

For each parameter, a total of four representative plots are shown. The top left plot shows the surface heave with time. The top right plot shows the frost penetration. The freezing front is found by linearly interpolating between nodes to find where the ice saturation is 1%. This way of post processing the results leads to a bit less smooth lines for the real (non-linear) saturation curves. The bottom left plot shows the ice saturation profile after 60 and 120 days. Finally, the bottom right plot shows the pore pressure development 10, 50 and 100cm below the surface, with a logarithmic time scale.

Phase Change parameters:

The permeability parameter, m^p

The results for m^p in the range of 0.25 to 1.5 is plotted in figure 6.5. The permeability model parameter seams to have almost no effect on ice saturation, top heave or the freezing front. Since a low m^p represents a rapid loss in permeability with decreasing temperature, the drop in pressure during freezing is expected to be higher. This effect is visible in the figure, and the maximum difference is approximately 1.4kPa. Also visible is the increase in pore pressure behind the freezing front, which probably appear due to numerical problems related to increasing non-linearity.

The strength parameter, η

The results for η in the range of 0.2 to 1 is plotted in figure 6.6. The strength model parameter does not seam to effect freezing depth or the ice saturation. Since a low η represents a rapid increase in strength, decreasing η should limit the deformation. This is clearly visible in the top heave, where a reduction from η=1 to 0.2 results in a top heave reduction from 13.2cm to 2.1cm. The suction during freezing is also decreased, with as much as 1.5kPa.

Saturation model parameter 1, S^α

The results for S^α in the range from 0.05MPa^{-1} to 0.25MPa^{-1} is shown in figure 6.7. S$^\alpha$, S^β and S^γ all directly effects the saturation curves. From the plot it is visible that S$^\alpha$ has a large effect the slope in the mid section. Decreasing the saturation α parameter from 0.25Mpa^{-1} to 0.05MPa^{-1} increases the heave from 7.2cm to 18.4cm. The greatest drop in pore pressure

is achieved with S^{α} close to 0.1^{-1}.

Saturation model parameter 2, S^{β}

The results for S^{β} in the range from 1.5 to 3.5 is shown in figure 6.8. A decrease in the saturation parameter β seams to rapidly increase the ice saturation in the beginning of freezing. Increasing S^{β} from 1.5 to 3.5 increases heave from 7.5cm to 16.5cm, maximum pore pressure drop increase with 1.5kPa, and the frost penetration has a notable reduction.

Saturation model parameter 3, S^{γ}

The results for S^{γ} in the range from 4 to 16 is shown in figure 6.9. The saturation model parameter γ seams to greatly affect the ice saturation curvature for high ice saturation. Increasing S^{γ} from 4 to 16, reduces heave for 16,7cm to 11cm, but the freezing front is not greatly affected. The freezing induced suction reaches a maximum using S^{γ} close to 8.

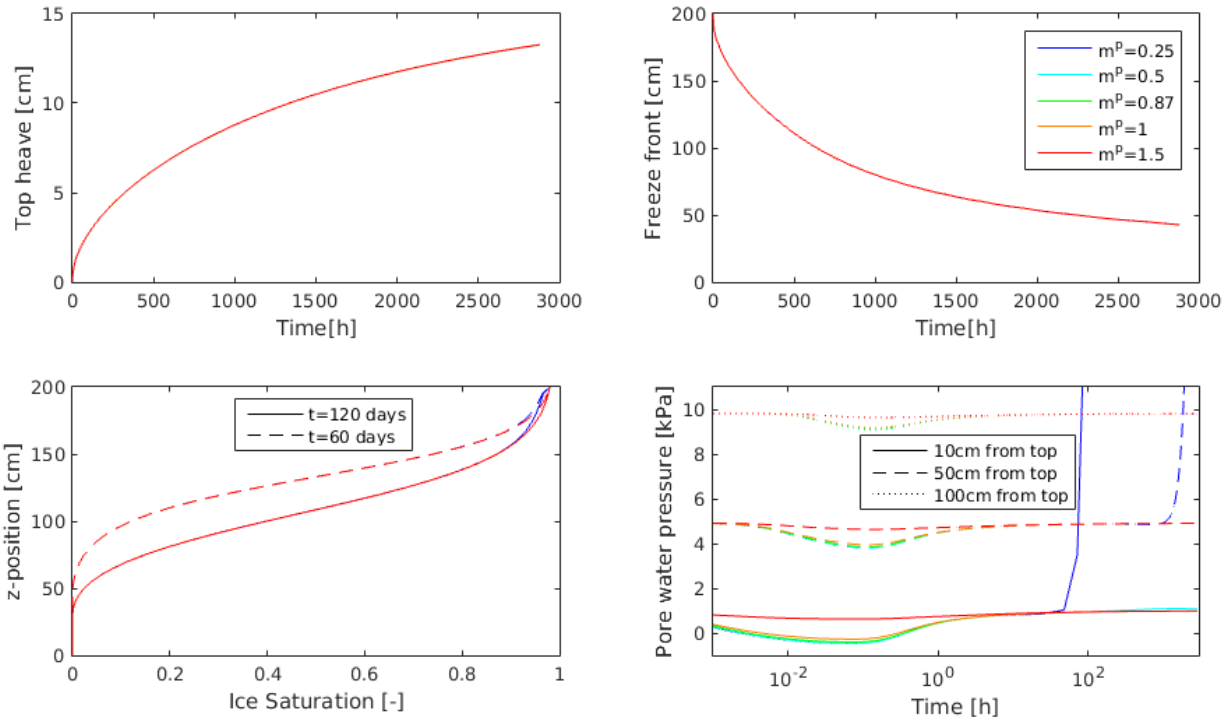

Figure 6.5: Parametric study of the permeability parameter, m^p

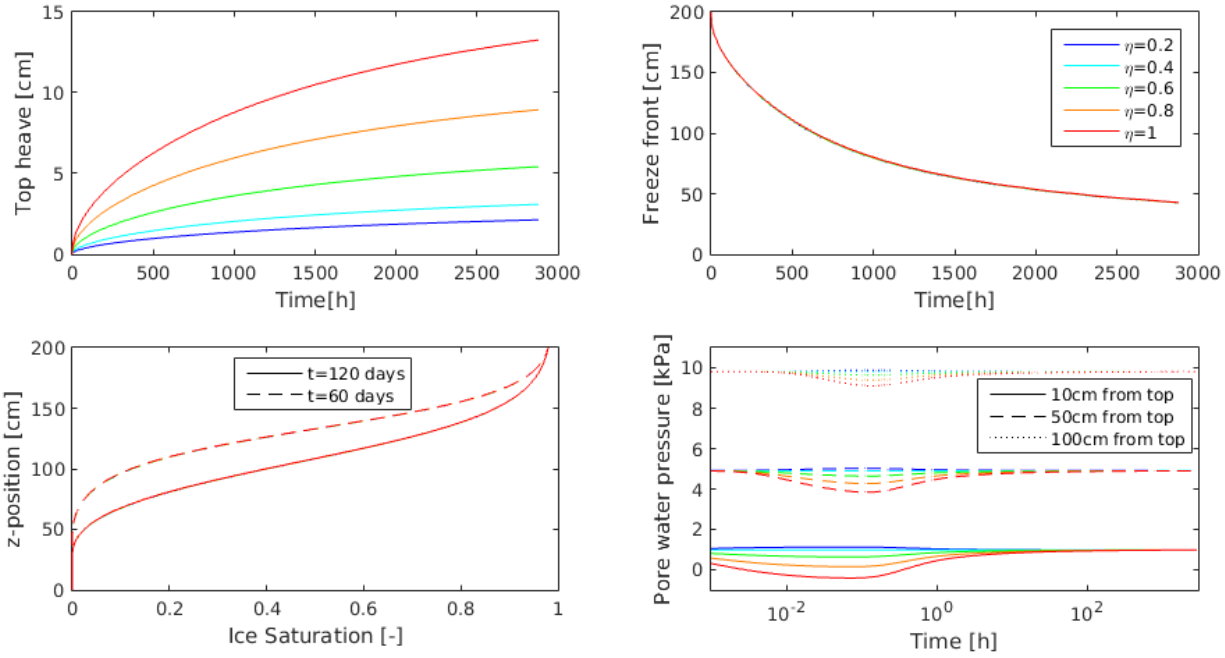

Figure 6.6: Parametric study of the strength parameter, η

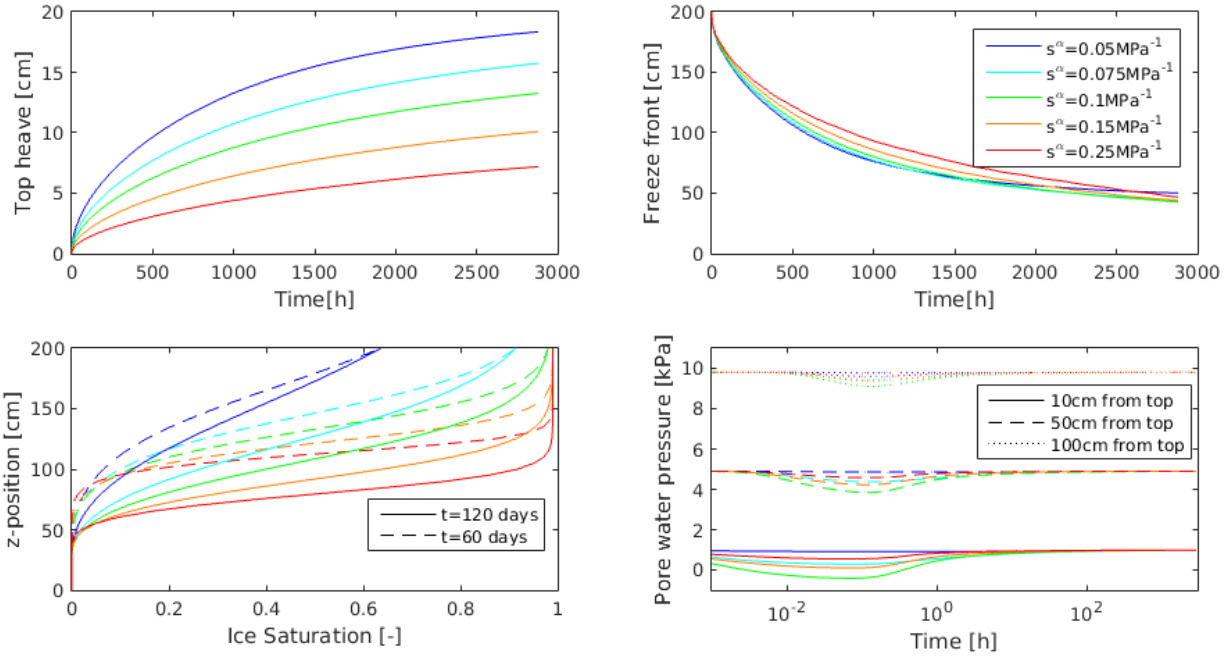

Figure 6.7: Parametric study of the saturation curve parameter 1, S^{α}

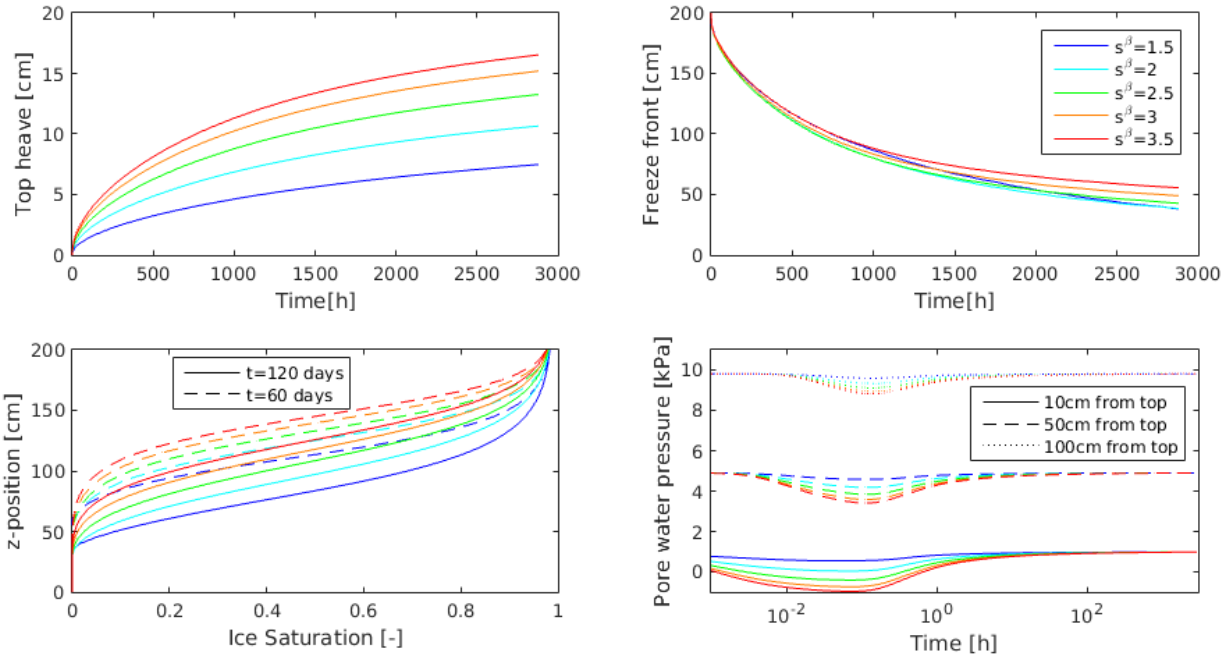

Figure 6.8: Parametric study of the saturation curve parameter 2, S^{β}

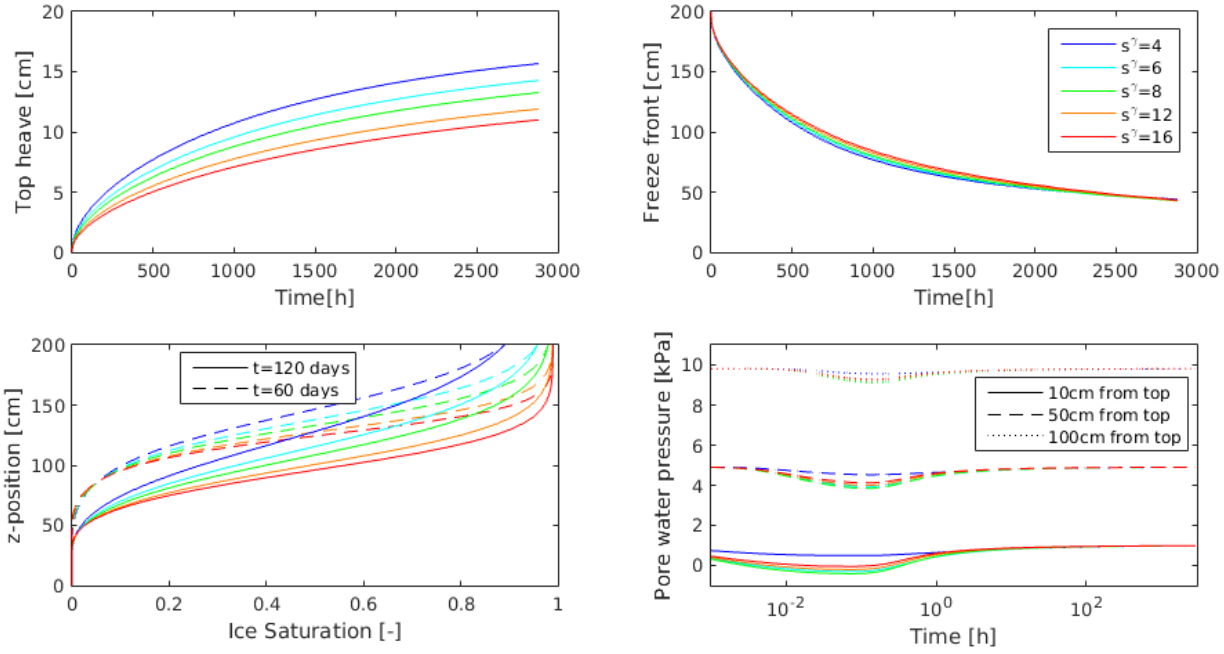

Figure 6.9: Parametric study of the saturation curve parameter 3, S^{γ}

Material parameters:

Grain density, ρ_s

The results for ρ_s in the range of 2500 to 2800Kg/m^3 is plotted in figure 6.10. It is clearly visible that the solid density contribution is minimal.

Grain heat capacity, c_s

The results for c_s in the range of 600 to 1000J/KgK is plotted in figure 6.11. A lower heat capacity would increase frost penetration, and hence increase the heave. Compared to the other parameters, this effect is very small.

Grain heat conductivity, λ_s

The results for λ_s in the range of 0.5 to 4.5W/mK is plotted in figure 6.12. Increasing λ_s increases both freezing depth and the pore pressure drop. This results in a increase in top heave from 10.7cm to 15.2cm. The increasing rate of frost penetration also results in changes in the ice saturation profile.

Hydraulic conductivity, k

The results for hydraulic conductivity in the range of 10^{-2} to 10^{-9}m/s is presented in figure 6.13. The permeability seams to have no effect on frost penetration or ice saturation. Comparing pore pressure and top heave, it is clear that the increased pore pressure drop is counteracted by a decrease in permeability, resulting in a relatively equal water inflow. For very low permeability, the permeability outweighs the increased pore pressure, resulting in less heave.

Young's modulus, E

The results for Young's modulus in the range of 0.5MPa to 75MPa is plotted in figure 6.14. The effect on frost penetration and ice saturation is very limited. However, as expected considering the momentum balance, a decreasing Young's modulus increases the top heave. Increasing E from 0.5MPa to 75 reduces the heave from 54.7cm to 2.6cm. The maximum drop in pore pressure is increased with 3.1kPa, and the decreasing Young's modulus also lengthen the period with freezing induced suction.

Porosity, n

The results for porosity in the range of 0.2 to 0.6 is plotted in figure 6.15. Changing the porosity greatly changes the thermal properties, as shown in equation 3.4 and 3.5. This effect is visible in the freeze front plot, resulting in a higher rate of penetration in the beginning, and 15 cm deeper frost penetration. Decreasing the porosity from 0.6 to 0.2 also increases the maximum pore pressure drop with 1kPa.

Poisson's ratio, μ

The results for Poisson's ratio in the range of 0.15 to 0.33 is plotted in figure 6.16. Increasing Poisson's ratio results in increased stiffness, as from equation 2.7. The results are hence directly comparable to the Young's modulus study, however in a much smaller scale.

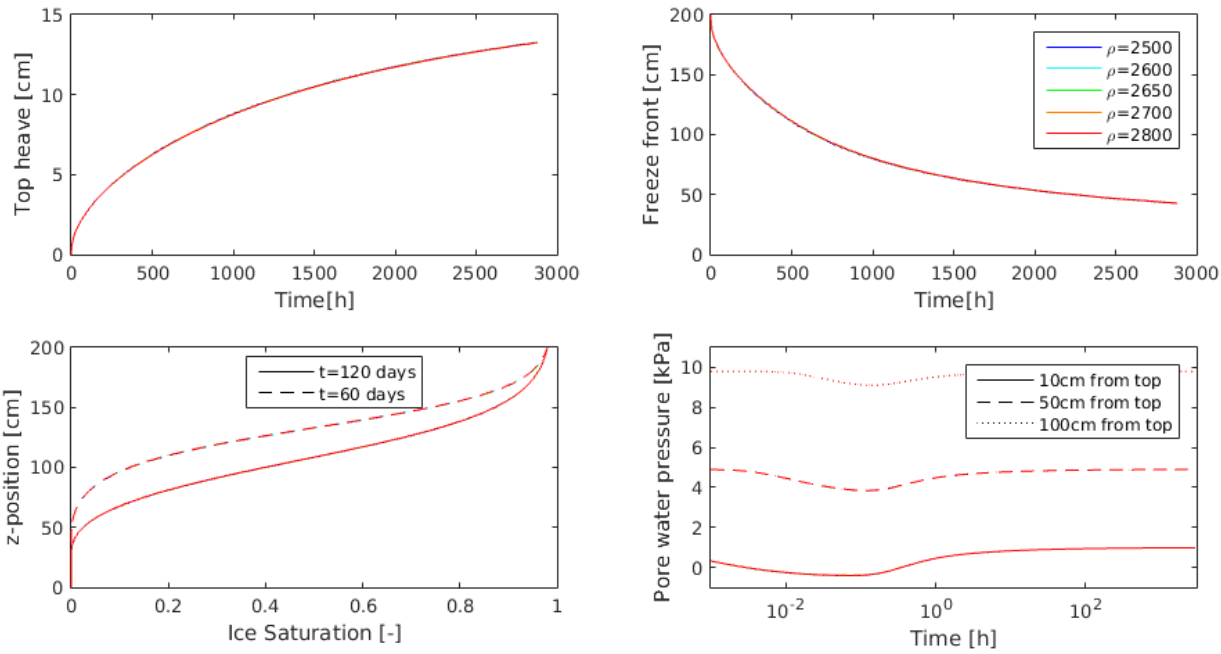

Figure 6.10: Parametric study of the grain density, ρ_s

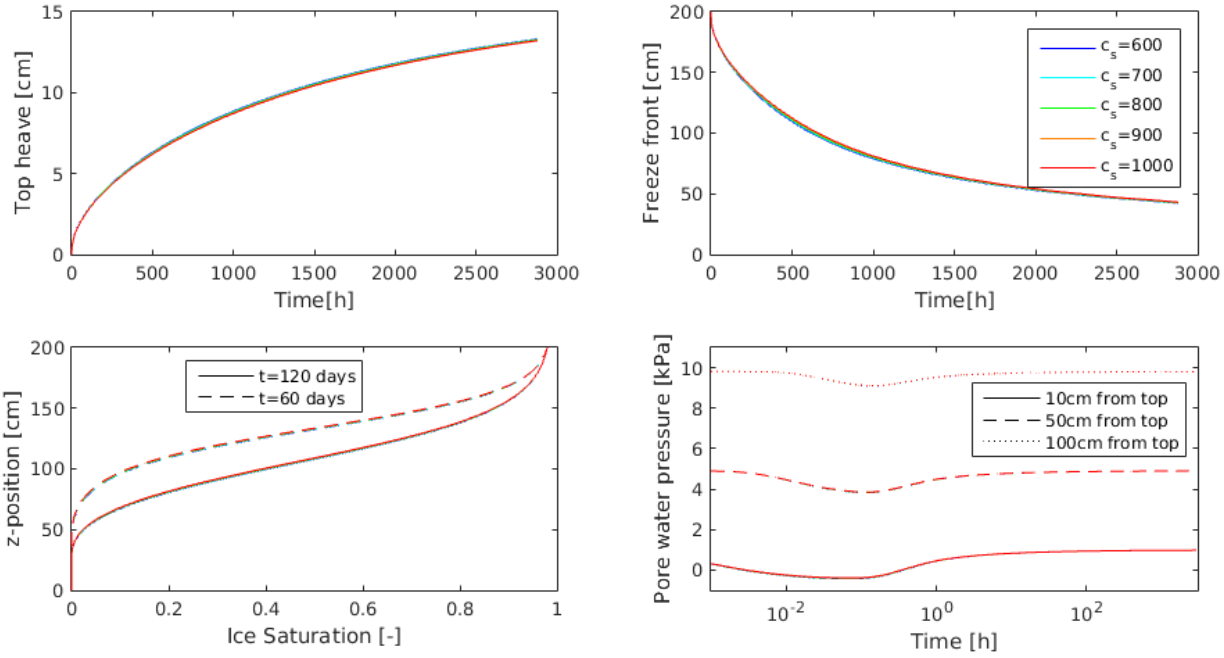

Figure 6.11: Parametric study of grain heat capacity, c_s

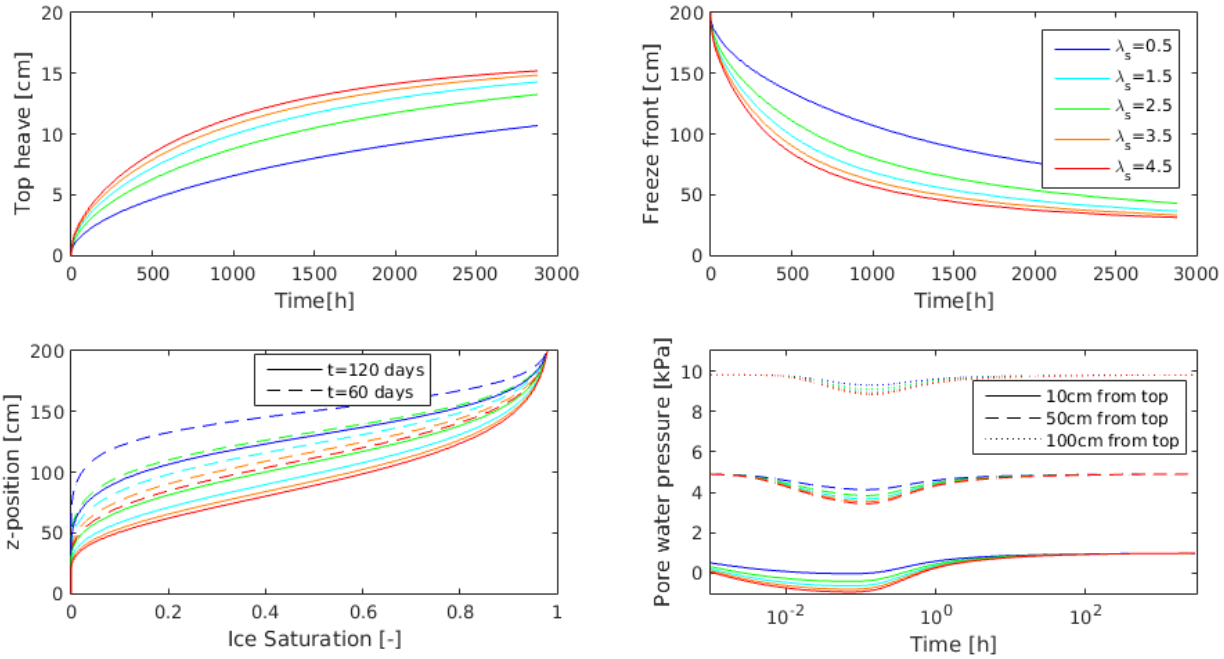

Figure 6.12: Parametric study of the grain heat conductivity, λ_s

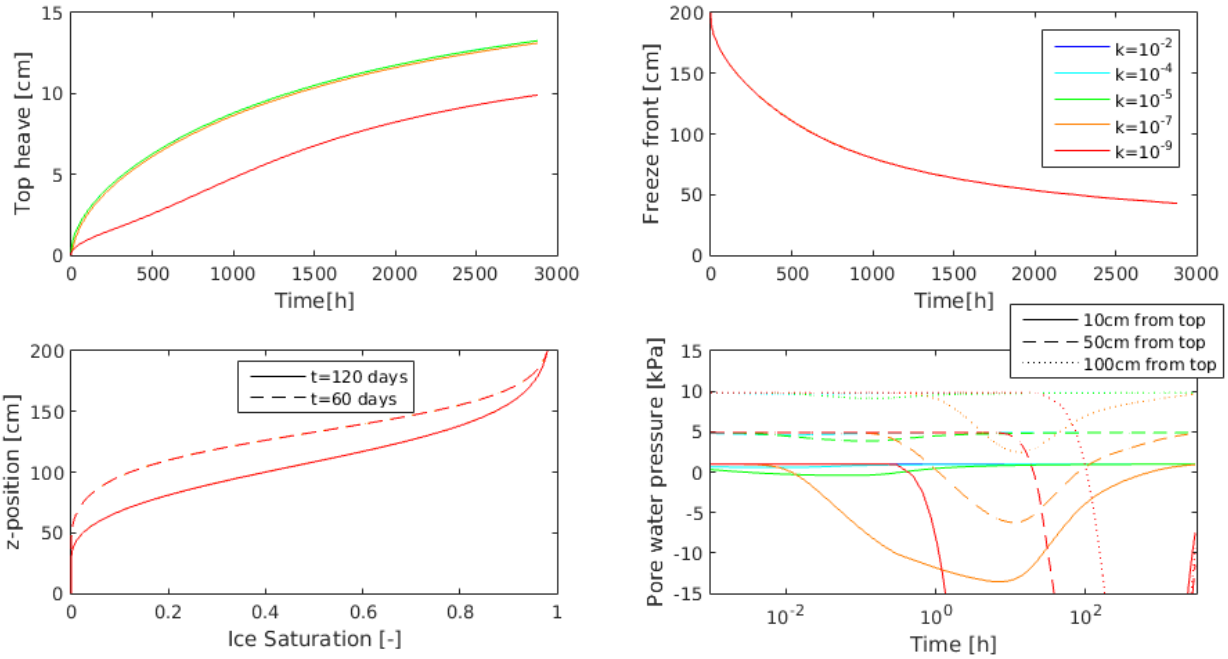

Figure 6.13: Parametric study of the hydraulic conductivity, k

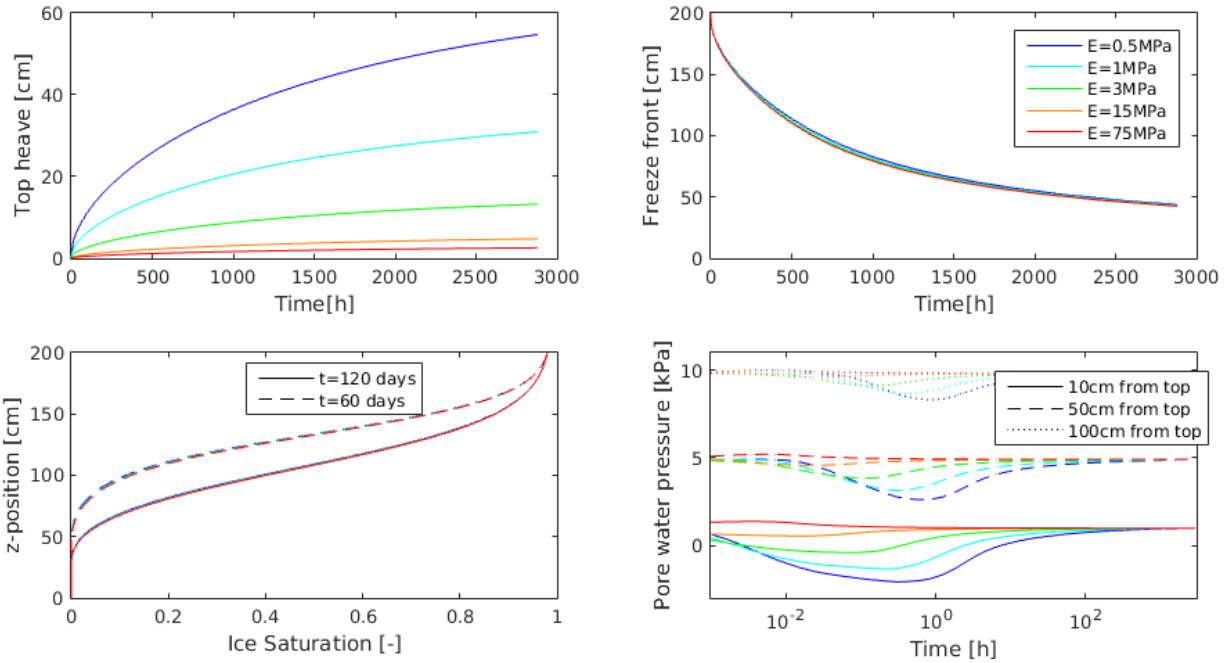

Figure 6.14: Parametric study of Young's modulus (stiffness), E

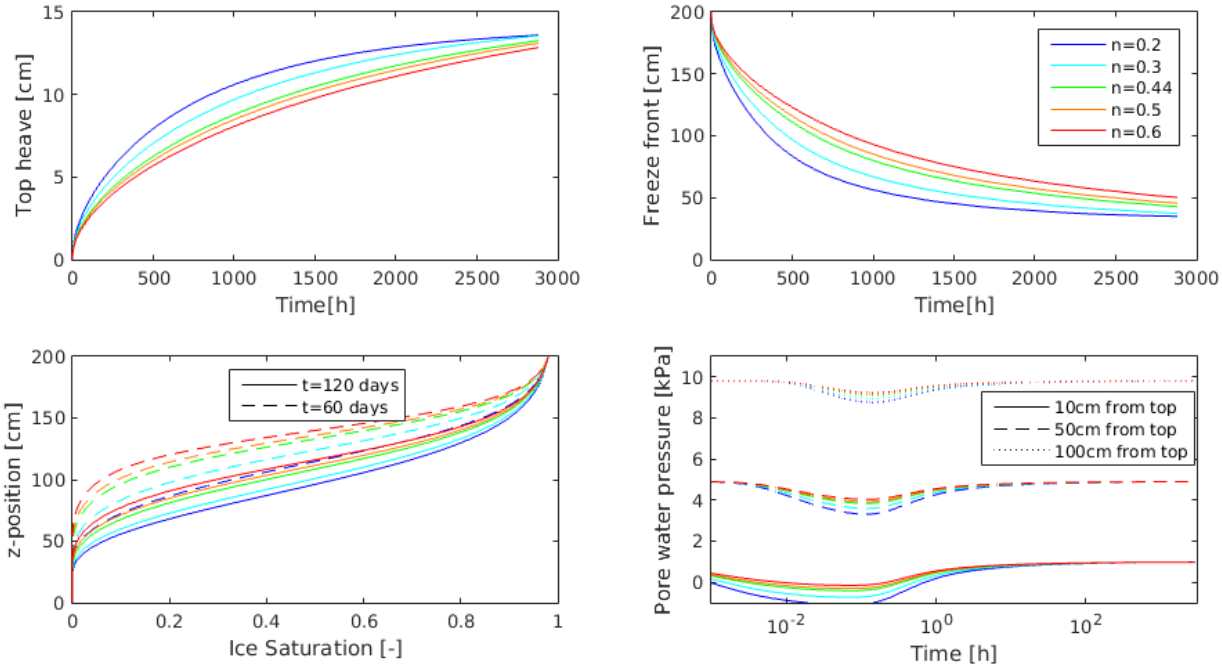

Figure 6.15: Parametric study of the porosity, n

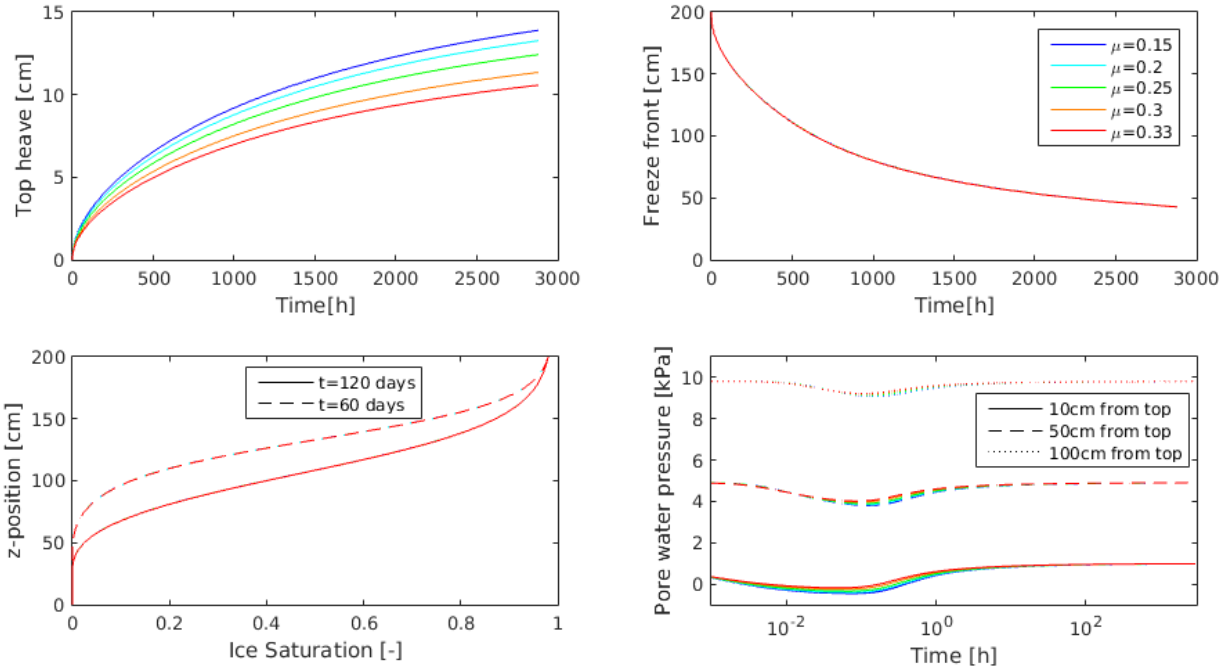

Figure 6.16: Parametric study of Poisson's ratio, μ

Saturation curves based on soil type

It must be noted that the saturation curves makes the equations highly non-linear, and that the time stepping is greatly reduced for this simulation. With exception of the sand, the top deformation increases with decreasing grain size. The total heave of the clay is almost two times that of an silty sand. The results also show that the pore pressure behind the frozen fringe becomes increasingly difficult to simulate when the saturation curves are steep.

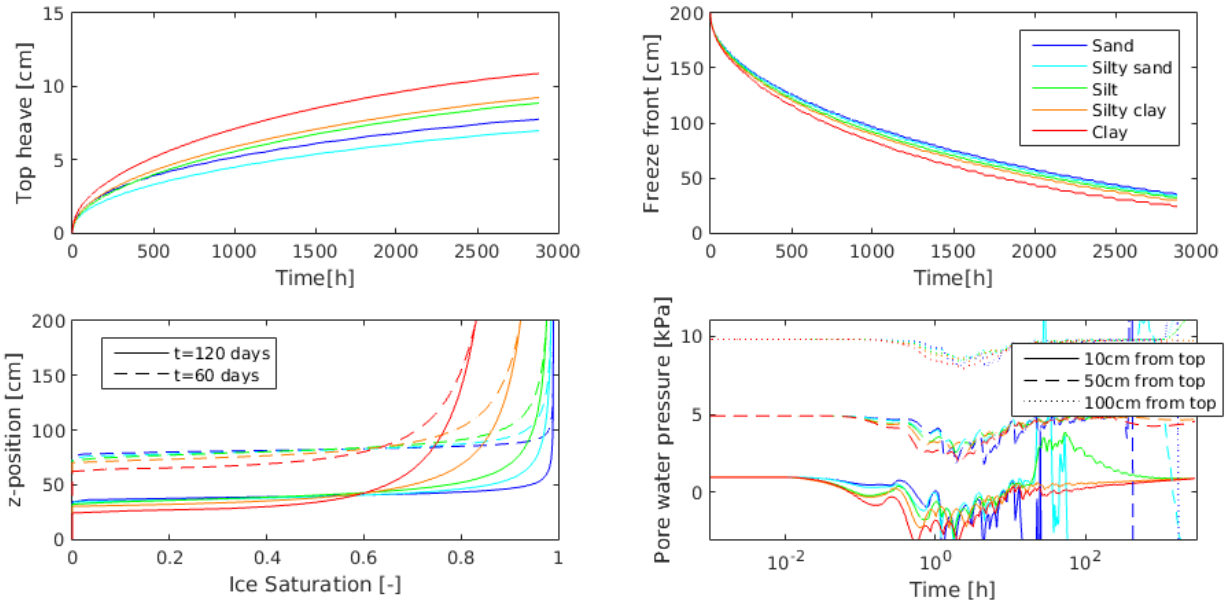

Figure 6.17: Parametric study of the different saturation curves

6.1.4 Discussion

Evaluation of parameters effect on the solution

The effect of each parameter is summarised in table 6.5, ranging from no effect(-) to high effect. As the parametric study is conducted only on a one dimensional model with constant surface temperature, the importance of the parameters may vary for different situations.

Parameter	Heave	Frost penetration	Ice Saturation	Freezing induced suction
m^p	low	-	-	medium
η	high	-	-	medium
S^α	high	medium	high	medium
S^β	high	medium	high	medium
S^γ	medium	low	high	medium
ρ_s	-	-	-	-
c_s	low	low	-	-
λ_s	medium	high	high	medium
k	medium	-	-	high
E	high	low	low	high
n	medium	high	medium	medium
μ	medium	-	-	high
Saturation curves	high	medium	high	high

Table 6.5: Summary of parametric study

Evaluation of saturation curves effect on the solution

One typically expects the most heave from a silty clay, and reduced heave with smaller or larger grain sizes. There is however to little information on the relationship between saturation curves, the strength parameter and the stiffness parameter, to accurately model the different soil types. It is however clear that the saturation curves is important in estimating the total heave. It is also clear from the pore pressure development, that the pore water pressure in the frozen zone becomes significantly more difficult to model when using real saturation curves. Of the different soil type, the course material yields more oscillations in the pore pressure. It is also interesting to note that they clay needed the smallest time steps, while the silt required fewest time steps to avoid divergence.

Limitations in phase change parameter estimation

Although there exist some information on the strength, permeability and saturation model, there has not been found any previous data on the correlations between the models. As these

model parameters are closely related, the data presented in section 6.1.2 must be considered as estimations.

Convergence in relation to the phase change parameters

The parameters m^p ,η, S^α, S^β and S^γ has a huge effect on the convergence properties of the model. As figure 6.3 and 6.4 clearly show, the strength and permeability properties are highly non-linear. From experience gathered during this thesis, it seams m^p less than 0.5 ,η grater than 1 rapidly decreases the models convergence properties. However, the comparison with existing data suggest that this is the area where the real soil properties lies. The increases non-linear, and divergent problem related to the strength and permeability model seams to be a physical, rather than numerical induced problem.

The saturation curves effect on convergence has proven much more difficult to explain, and this thesis contains no solution to this challenge. During selection of saturation curves, clays with more curvature has been most difficult to converge. The selections has also shown that different sets of S^α, S^β and S^γ, representing almost exactly the same curve, have different convergence properties. It is hence reasonable to believe that the divergence problems can be related to both physical and numerical issues.

6.2 Simulation of Frost Heave Cell Experiment

Although not very common in Norway, frost heave cells can be used to determine the heaving properties of soils. Frost heave cells are traditionally used to determine the segregation potential (Konrad (1980)), and the material properties important in the model is not always investigated. The test preformed in Konrad and Seto (1994) is chosen as a reference test, because the material properties(E,k,n) are relatively well defined. The test setup is shown in appendix C.

6.2.1 Model

The geometry and mesh is shown in figure 6.18, and the material properties are either calculated based on average properties presented in the paper, or given a reasonable value. The material properties is shown in table 6.6. The sample is consolidated to 100kPa pore pressure and 20kPa overburden, with a total of 60 time steps and 250 hours. The temperature in the heave phase is applied instantly, with -1.5 and 3.7 degrees Celsius on the top and bottom respectively. The first 20 hours of the heave phase consist of 5000 time steps, and the last 27 hours consist of 4000 time steps.

The phase change parameters related to clay is making the equations highly non-linear. In order to overcome divergence from the instant temperature change, the mesh is very fine and the tolerance is relatively low (1e-2).

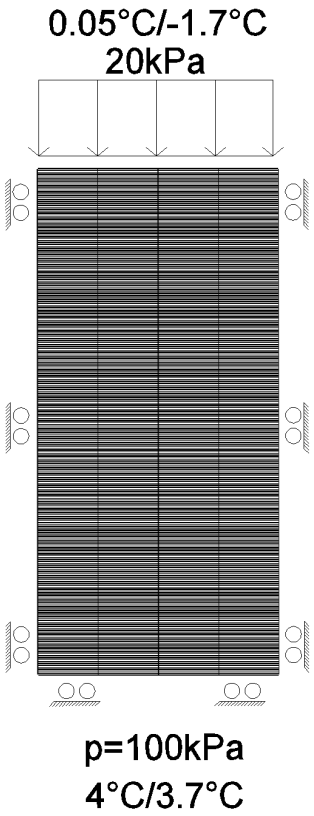

Figure 6.18: Model and mesh for the frost heave cell calculation

Property	Symbol	Value	Unit
Porosity	n	0.705	-
Solid density	ρ_s	2800	Kg/ m³
Water density	ρ_w	1000	Kg/ m³
Ice density	ρ_i	910	Kg/ m³
Young's modulus of soil	E_s	110e3	Pa
Young's modulus of ice	E_i	9.1e9	Pa
Poisson's ratio for soil	ν_s	0.33	-
Poisson's ratio for ice	ν_i	0.4	-
Strength model parameter	η	3	
Permeability	K	2e-9	m/s
Saturation model parameter 1	S^α	2e-6	Pa^{-1}
Saturation model parameter 2	S^β	1	-
Saturation model parameter 3	S^γ	0.6	-
Permeability model parameter	m^p	0.3	-
Solid heat capacity	c_s	800	J/KgKs
Water heat capacity	c_w	4190	J/KgKs
Ice heat capacity	c_i	2095	J/KgKs
Solid thermal conductivity	λ_s	2.5	W/mK
Water thermal conductivity	λ_w	0.6	W/mK
Ice thermal conductivity	λ_i	2.2	W/mK
Latent heat of fusion	L_f	334000	J/kg

Table 6.6: Material properties for frost heave cell calculation

6.2.2 Results

The top deformations and temperature is shown and compared with Konrad and Seto (1994) in figure 6.19 and 6.21. Deformation, temperature and ice saturation profiles are shown in figure 6.20, and the error compared with the tolerance is shown in figure 6.22.

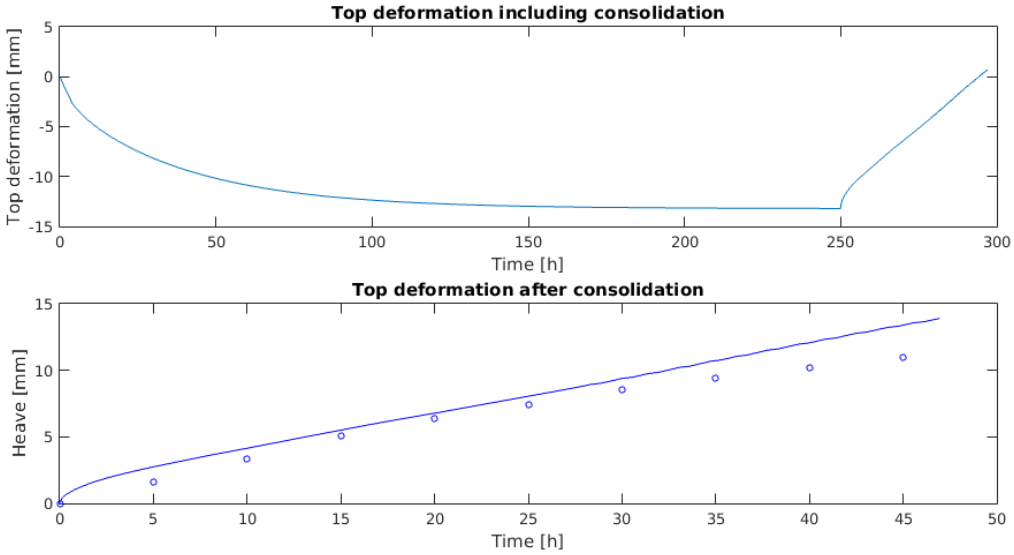

Figure 6.19: Surface deformation of test sample in y-direction, compared with test results

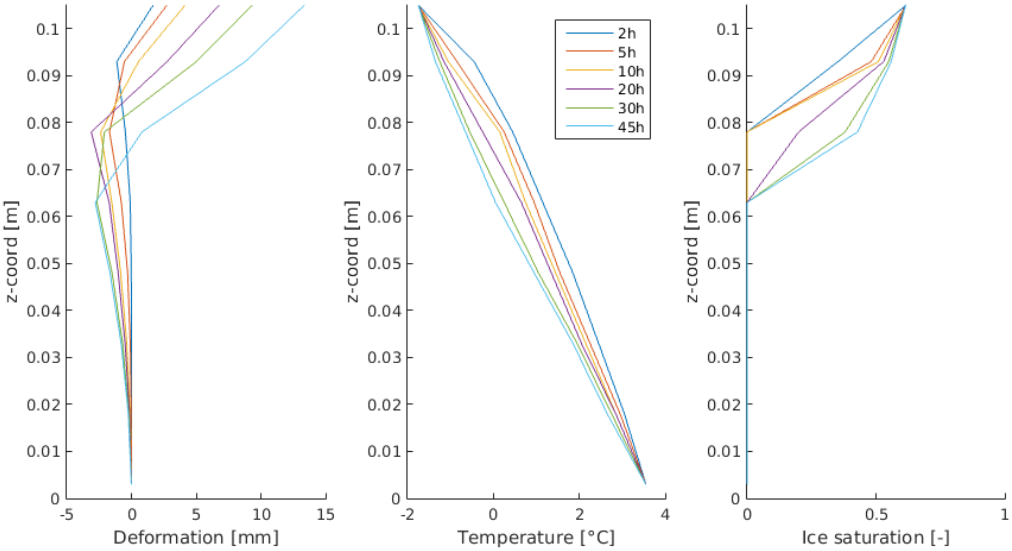

Figure 6.20: Deformation, temperature and ice saturation profiles

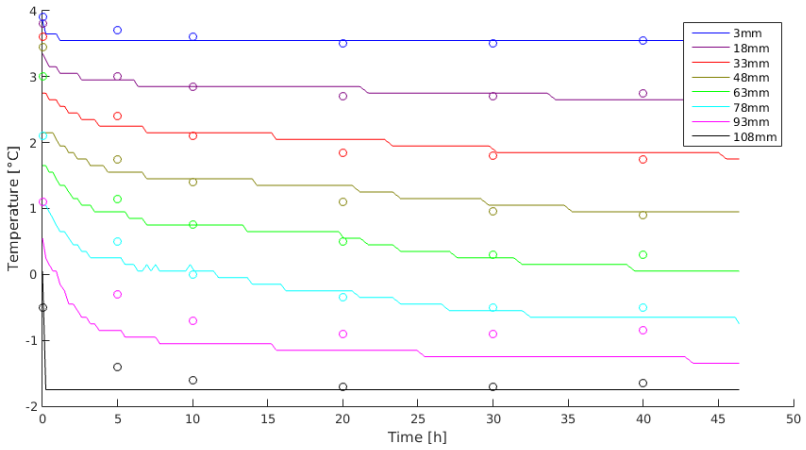

Figure 6.21: Temperature development compared with test results

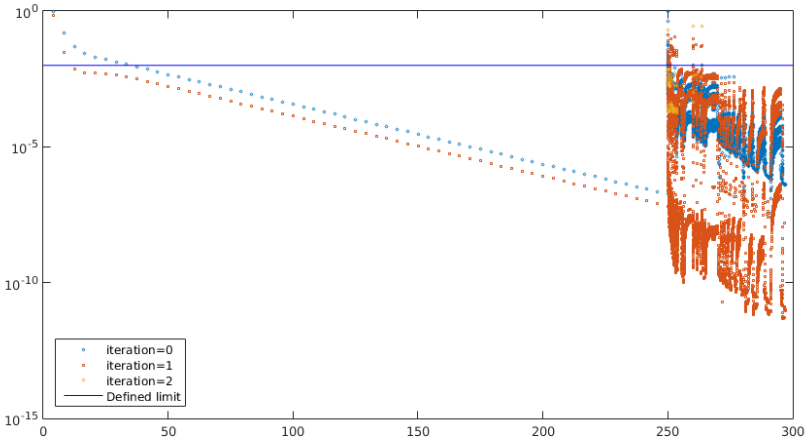

Figure 6.22: Error estimation for the two first iterations

6.2.3 Discussion

When considering the top heave and temperature, the model recreates the test well. The temperature change is enforced instantly in the model, as intended by Konrad and Seto. The results does however show a more gradual temperature change, but this deviation is belived to have limited effect on the overall solution. It is important to note that the real test has a large amount of plastic deformation, which is not accounted for in the linear elastic model. The linear elastic model reduces the deformation below the freezing front, but it also reduces heave. For the frost heave cell, the effects seams to cancel out each other. The maximum settlement below the frost front is 3-4mm in the model, but laboratory results shows close to 11mm deformation.

6.3 Simulation of Seasonal Temperature Variation

This chapter contains a study on a one dimensional frost heave simulation, using a sinusoid function to represent the temperature variation through the year.

6.3.1 Model

Surface temperature can be approximated using a sinus curve. A sinus function with mean temperature and amplitude of 5.68 and 10 respectively, is applied at the top boundary of the model in figure 6.23. The temperature function is based on observed temperature over a 11 year period for Ås, as shown in figure 6.24. The temperature at the bottom of the model is assumed to be equal to the annual mean air temperature. The mesh is created in python, with 3 levels of refinement. The area where the temperature is expected to be below 0, is finer meshed than the bottom part. The pore pressure is hydrostatic from the surface, and at the bottom boundary temperature is assumed to be equal to the average surface temperature. Time stepping is set to 2 steps per day during summer(T>0), and 83 steps per day during winter(T<0). The simulation is carried with and without applying the phase change equations. A summary of the chosen material parameters is presented in table 6.7.

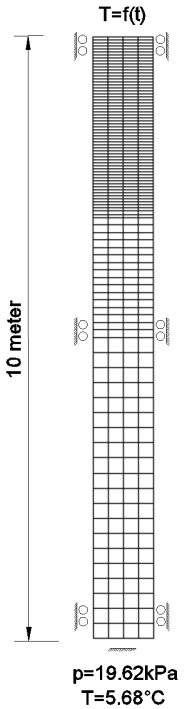

Figure 6.23: Model and mesh for varying temperature load

Property	Symbol	Value	Unit
Porosity	n	0.46	-
Solid density	ρ_s	2650	Kg/ m³
Water density	ρ_w	1000	Kg/ m³
Ice density	ρ_i	910	Kg/ m³
Young's modulus of soil	E_s	2e6	Pa
Young's modulus of ice	E_i	9.1e9	Pa
Poisson's ratio for soil	ν_s	0.2	-
Poisson's ratio for ice	ν_i	0.4	-
Strength model parameter	η	2	
Permeability	K	2e-9	m/s
Saturation model parameter 1	S^α	5e-6	Pa^{-1}
Saturation model parameter 2	S^β	1	-
Saturation model parameter 3	S^γ	0.7	-
Permeability model parameter	m^p	0.4	-
Solid heat capacity	c_s	700	J/KgKs
Water heat capacity	c_w	4190	J/KgKs
Ice heat capacity	c_i	2095	J/KgKs
Solid thermal conductivity	λ_s	3.25	W/mK
Water thermal conductivity	λ_w	0.6	W/mK
Ice thermal conductivity	λ_i	2.2	W/mK
Latent heat of fusion	L_f	334000	J/kg

Table 6.7: Material properties for simulation of seasonal temperature variation

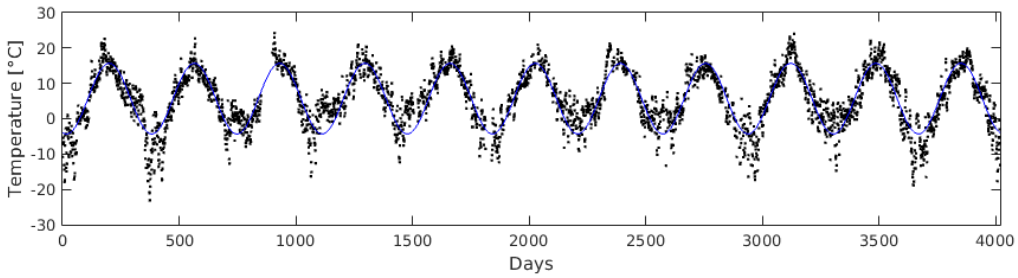

Figure 6.24: Fitting a sinus function to observed data for Ås

6.3.2 Results

An analytical calculation without latent heat is performed using the trumpet curve, as described in Andersland and Ladanyi (2004). The top left plot in figure 6.25 shows how fast the temperature converges for the ground freezing model. The other plots in figure 6.25 compares the analytical and THM models with and without ground freezing, at different times in the 5th year of the model. The temperate profiles are plotted for each month in figure 6.26. The development of top deformation is shown in figure 6.27. Temperature, deformation, ice saturation, heat flux and water flux is shown in figure 6.28 and 6.29, when the top deformation reaches a maximum, and late in the thawing process. The error tolerance was set to 5e-3, and figure 6.30 shows the approximate error relating to the first two iterations (if necessary) for each step. The time steps are much smaller during the ground freezing, and the vertical line shows when the time stepping is altered.

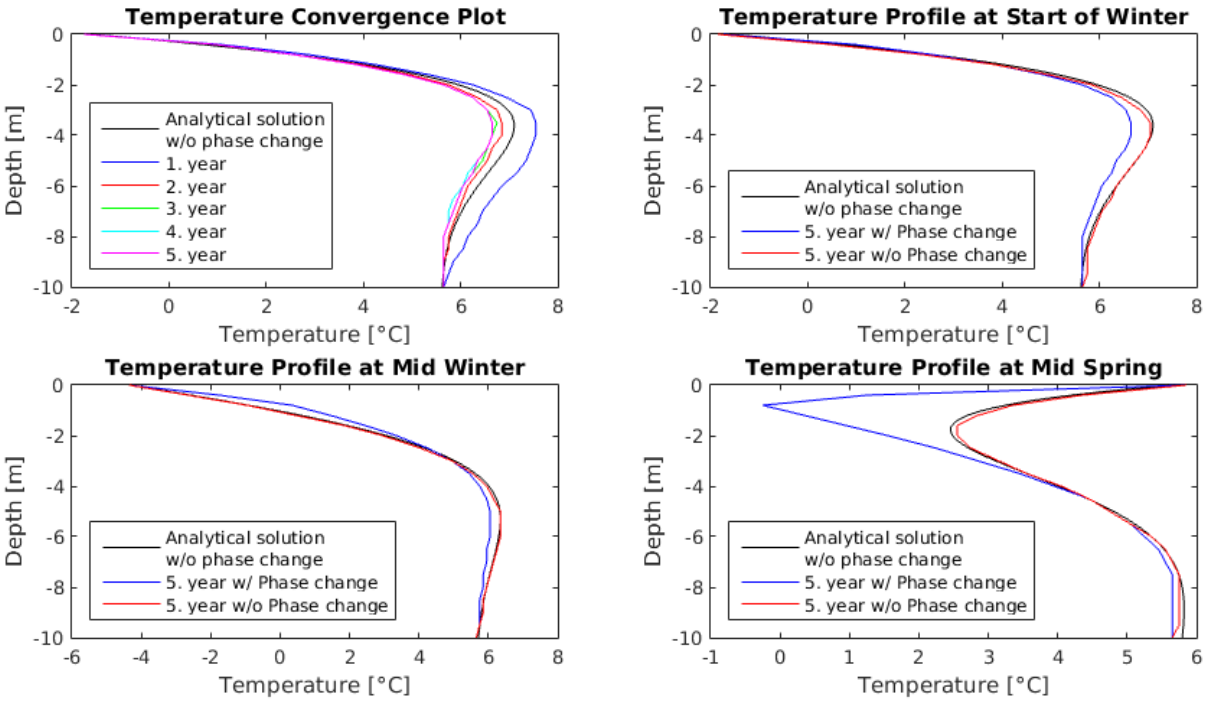

Figure 6.25: Convergence plot for the ground freezing model, and temperature plots comparing analytical and THM results with and without ground freezing

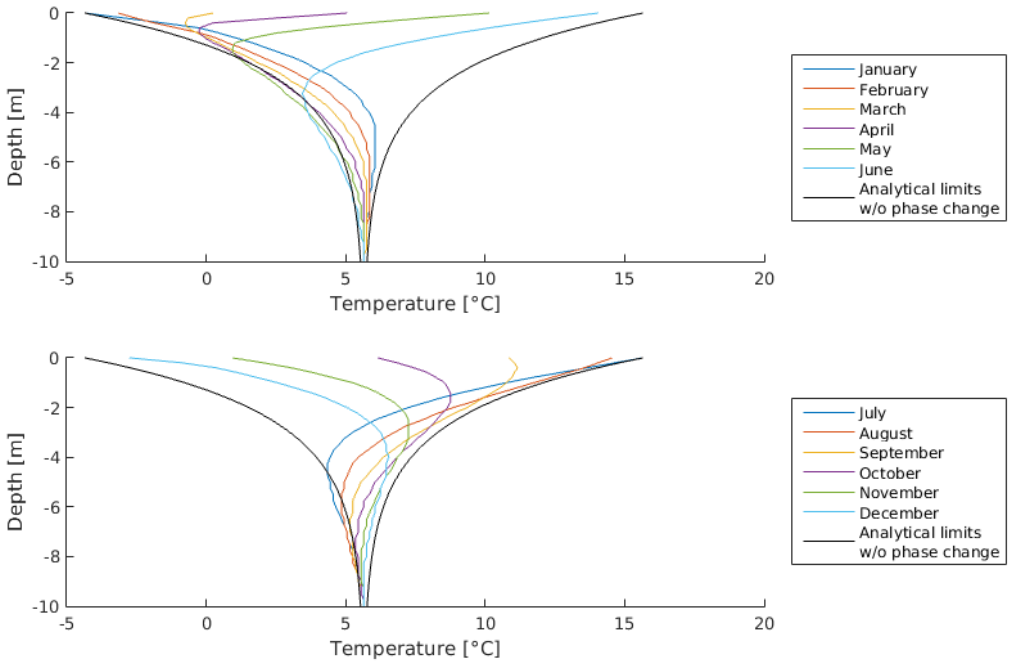

Figure 6.26: Temperature profiles with ground freezing plotted for each month in a year

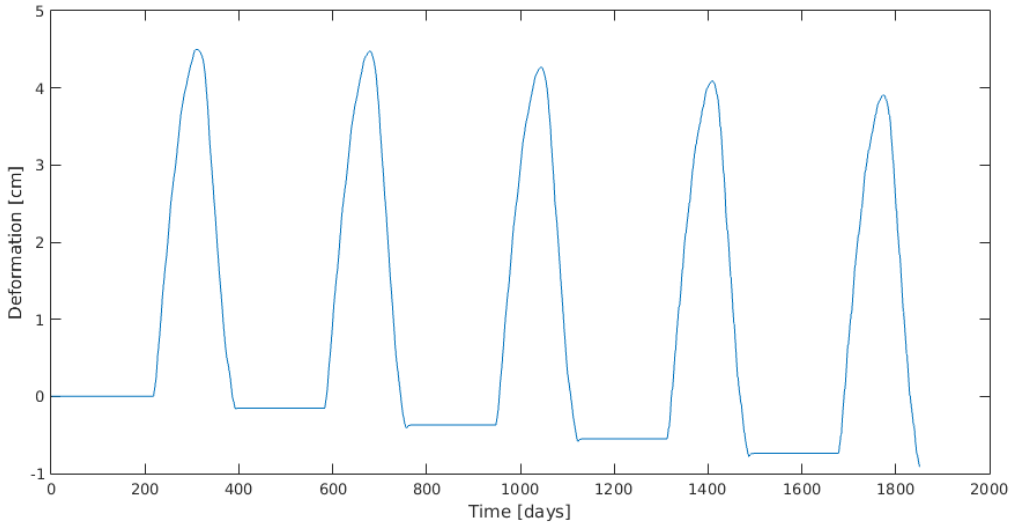

Figure 6.27: Development of top deformation

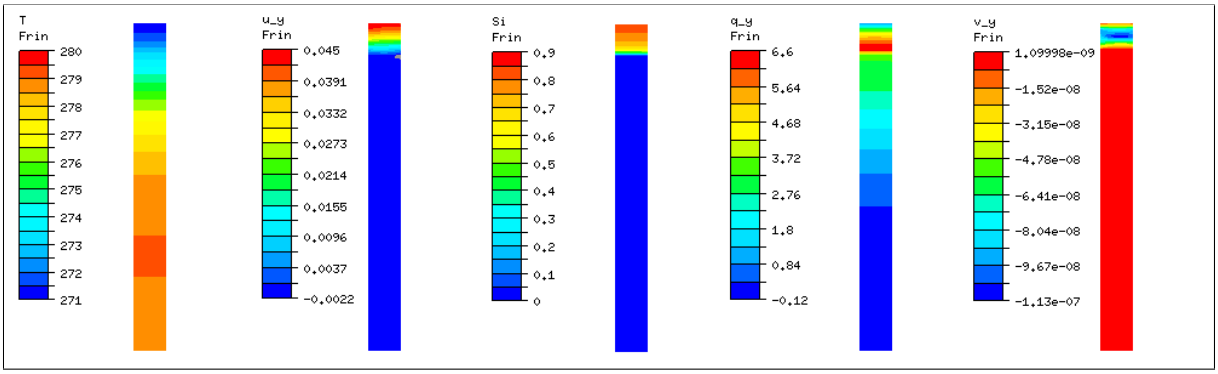

Figure 6.28: Temperature, deformation, ice saturation, heat flux and water flux when heave reaches a maximum

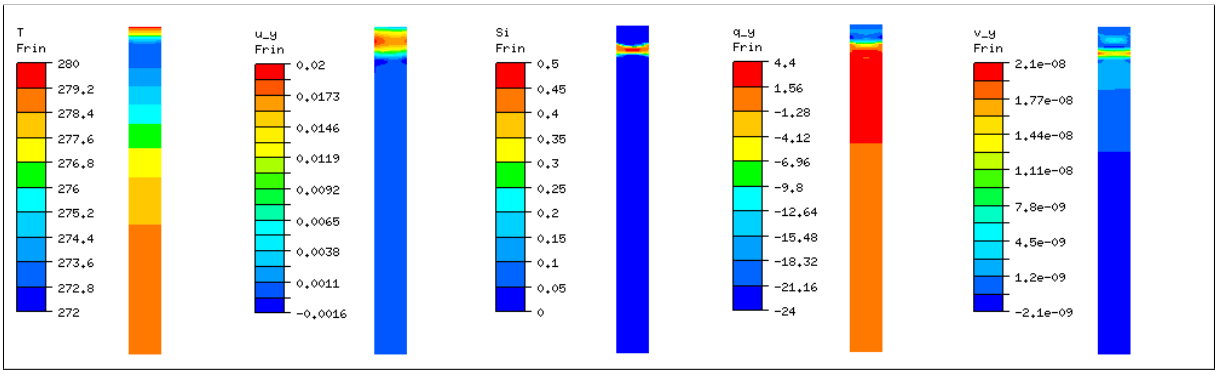

Figure 6.29: Temperature, deformation, ice saturation, heat flux and water flux when thawing from above.

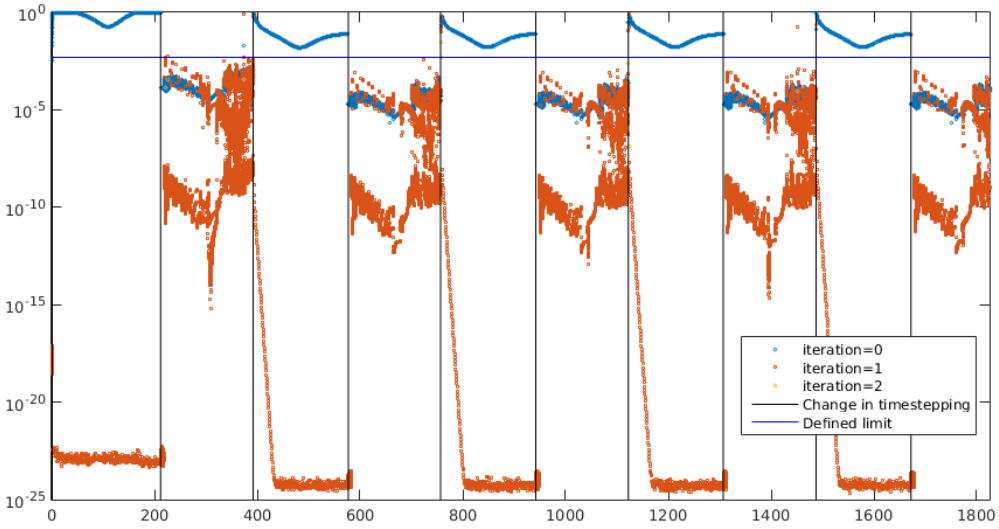

Figure 6.30: Error estimate of the solution. The vertical lines shows when the time stepping was increase/decreased.

6.3.3 Discussion

The convergence plot clearly shows that the temperature converges rapidly towards a solution close to the trumpet curve. It is clear that the latent heat influences the solution, and the difference reaches a maximum in the late spring. Although the temperature solution with and without phase change is different, the solutions is most similar at the start of winter. It is of interest to approximate the initial thermal regime without phase change, since the phase change requires much finer time stepping. The one dimension test shows that the maximum difference at the start of winter is less than 0.5 degree Celsius. It is hence reasonable to assume that the error from neglecting latent heat to establish an initial thermal regime is small.

Although the model is linearly elastic, and the top deformations is expected to return to 0 after a winter, the deformation after a winter decreases below 0. This is believed to be caused by accumulating errors from the Newton-Raphson iterations. The error is however small, approximately 3-4% compared to the total heave.

From both the error estimation plots, and experience, the model as proven most likely to diverge during the thawing phase.

6.4 Case Study

6.4.1 Introduction

The case problem is base on NGI (1996), related to damage on "Vestfoldbanen" and "Østfoldbanen" during the winter of 1996. NGI used thermistor strings to measure the temperature in the ground, heave on the separate rails is measured, and test pits are used to roughly estimate the material properties. In this section, two of the profiles are calculated. Due to the limited ground investigations, the results are not expected to match exactly.

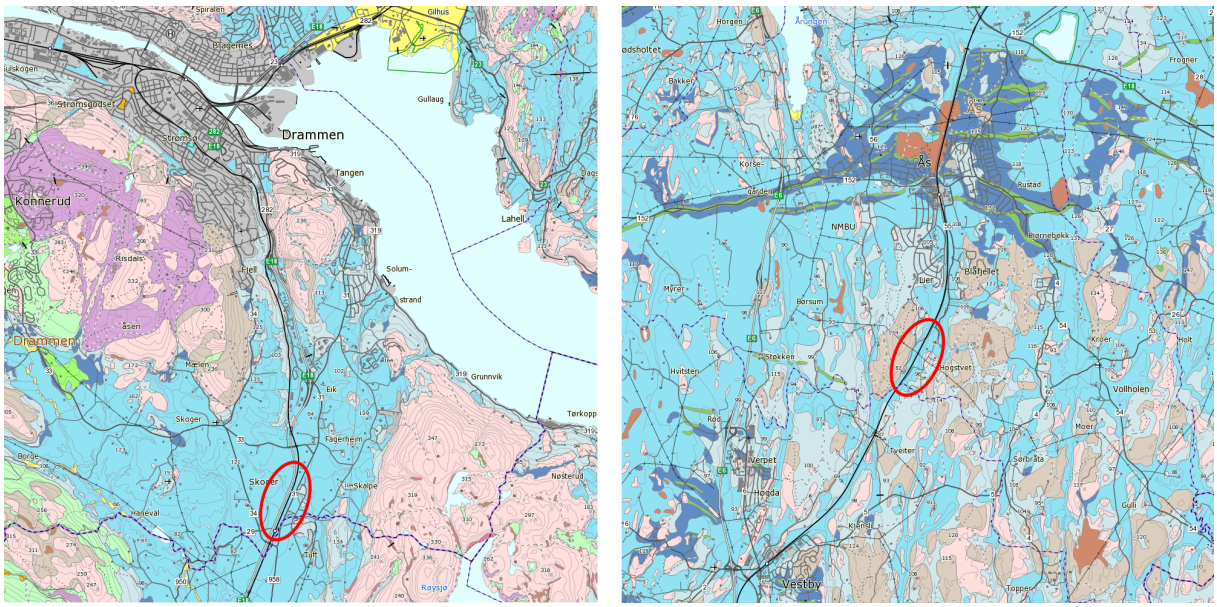

Figure 6.31: Sediment map for the sites near Drammen(left) and Ås(right)

6.4.2 Temperature and Pore Pressure

In the calculations, the surface temperature is assumed to be equal to the air temperature. The surface temperature in generally not equal to air temperature mainly due to windchill, radiation and snow cover. It is for example possible to add a snow cover using a Neumann boundary based on air temperature and heat conductivity for snow. At the time of writing, this feature is limited to fixed values, and is hence not applied. Temperature data is collected from eklima.met.no (2016), and shown in figure 6.33 and 6.32. The temperature is approximated using sinus curves for the initial condition, and monthly splines for the main winter calculation. The reports indicate a ground water table close to the surface, and below the frost protection layer.

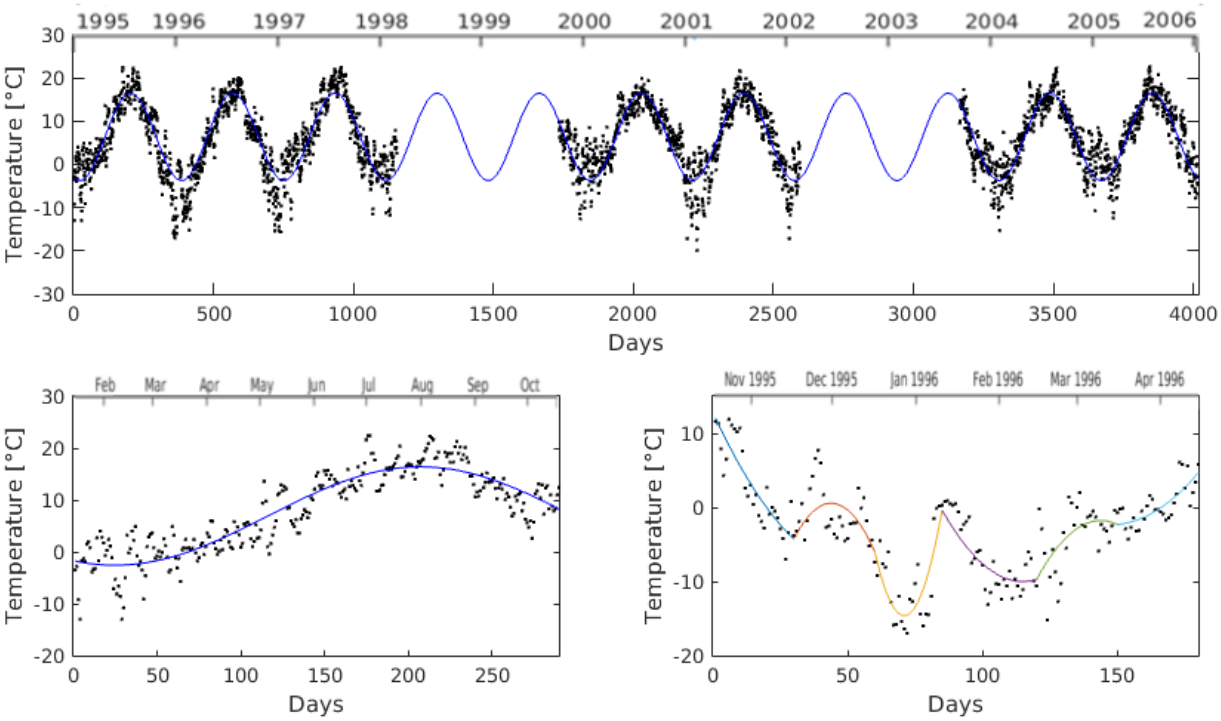

Figure 6.32: Observed and approximation of temperature for Skoger (close to the Drammen site)

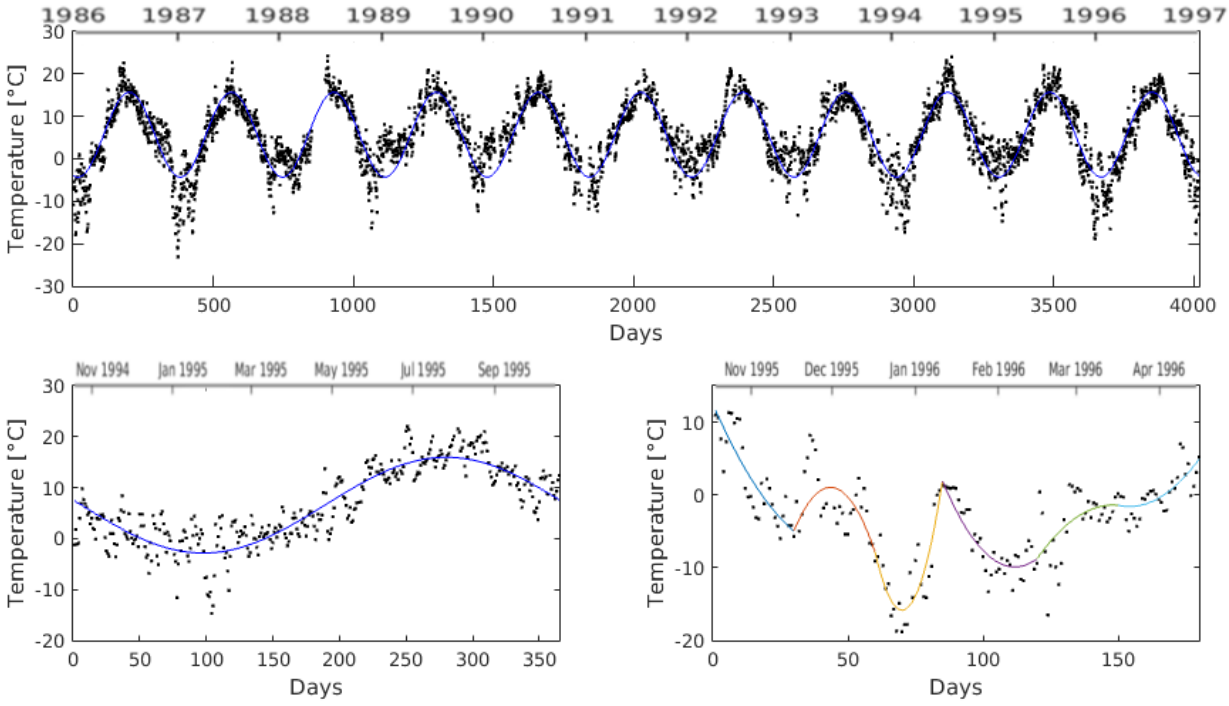

Figure 6.33: Observed and approximation of temperature in Ås

6.4.3 Material Properties

Both sites consist of a approximately 50cm thick ballast layer with 25-63mm crushed rock, over a minimum 1.25m thick frost protection/reinforcement layer with 0-250mm or 0-500mm crushed rock. The structure has good drainage, and NGI estimates a water content of as little as 2-3% during winter. Both layers are modelled to represent a dry material, since the model is based on fully saturated assumptions, porosity must be set to zero. The other material parameters are then adjusted to correlate with the porosity. Below the ballast and frost protection layer is a silty clay.

The thermal properties is discussed in NGI (1996), and the material properties used is related to unfrozen material properties in the report. A relatively recent ground investigation(NGI (2004)) was performed close to the Drammen site, containing CPTu with diffusion tests. The material properties used for the Drammen site is based on this report (Appendix D). Investigations on the site near Ås is older, and consist of mainly rotary weight soundings, vane test and simple laboratory test (NSB Engineeringavdeling (1989), Ingeniør Chr. F. Grøner AS (1979), NSB Engineeringavdeling (1988)). The test are not very well suited to determine the most important properties, but the soft silty/sandy clay reported is similar to what observed at the Drammen site. The silty clay in both Drammen and Ås is for simplicity modelled using the same material properties. Table 6.8 contains an overview of the parameters used in the simulation.

6.4.4 Geometry and Mesh

The geometry is based on NGI (1996), using profile number 2 for both Østfoldbanen and Vestfoldbanen, representing km 34.4 and km 62.0 respectively. Minor simplifications are made to ease the meshing, and the profile for Østfoldbanen is assumed symmetric. The polynomial degree is raised to quadratic and cubic for pore pressure and deformations respectively, and the mesh is created as shown in figure 6.35 and 6.34 using python. Due to long calculation time, only a relatively course mesh with 2 meters extra soil on each side of the model is used.

Property	Symbol	Ballast	Frost protection	Silty clay	Unit
Porosity	n	0	0	0.44	-
Solid density	ρ_s	2000	2000	2650	Kg/ m³
Water density	ρ_w	1000	1000	1000	Kg/ m³
Ice density	ρ_i	-	-	910	Kg/ m³
Young's modulus of soil	E_s	20e6	20e6	1e6	Pa
Young's modulus of ice	E_i	-	-	9.1e9	Pa
Poisson's ratio for soil	ν_s	0.2	0.2	0.3	-
Poisson's ratio for ice	ν_i	-	-	0.4	-
Strength model parameter	η	-	-	3	
Permeability	k	1e-1	1e-1	1e-9	m/s
Saturation model parameter 1	S^{α}	-	-	5e-6	Pa^{-1}
Saturation model parameter 2	S^{β}	-	-	1	-
Saturation model parameter 3	S^{γ}	-	-	0.7	-
Permeability model parameter	m^p	-	-	0.4	-
Solid heat capacity	c_s	920	920	750	J/KgKs
Water heat capacity	c_w	4190	4190	4190	J/KgKs
Ice heat capacity	c_i	-	-	2095	J/KgKs
Solid thermal conductivity	λ_s	1.5	1.45	3	W/mK
Water thermal conductivity	λ_w	0.6	0.6	0.6	W/mK
Ice thermal conductivity	λ_i	-	-	2.2	W/mK
Latent heat of fusion	L_f	-	-	334e3	J/kg

Table 6.8: Material properties for case study

6.4.5 Initial Conditions

The models are first run for approximately 4.5 years with the average temperature regime, then the year before the relevant winter is modelled to get the initial pore pressure and temperature. To avoid large calculations times, these calculations do not include phase change. The pore pressure is enforced with Dirichlet boundaries on the side of the models. For Drammen, the left side is hydrostatic from below the frost protection layer, and the right side is hydrostatic from 0.5 meter below the surface. For Ås, the left side is hydrostatic from below the frost protection layer, and the right side is hydrostatic from one meter below the surface. The result is shown in figure 6.37 and 6.36, using Si-units(K,Pa).

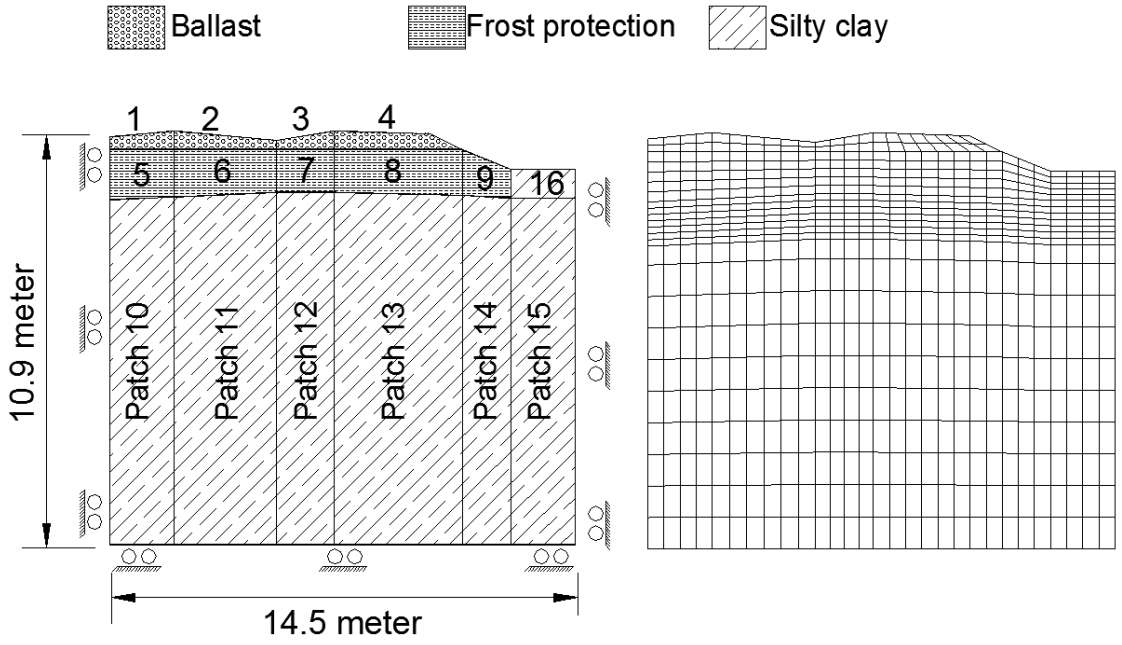

Figure 6.34: Geometry and mesh for the site near Drammen

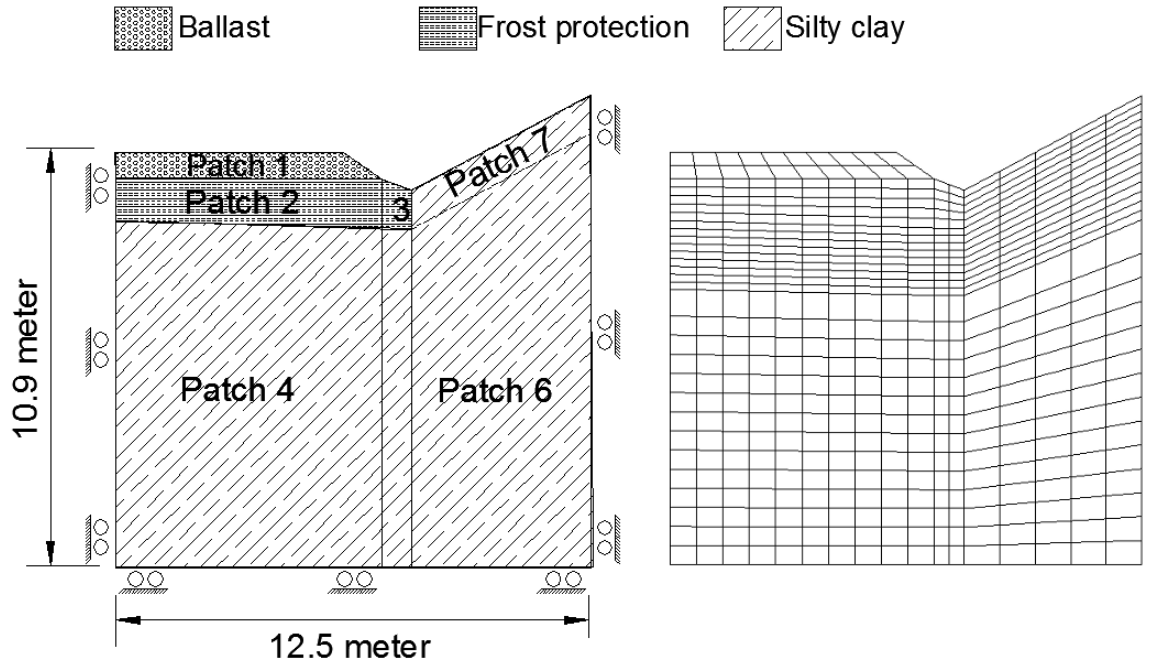

Figure 6.35: Geometry and mesh for the site near Ås

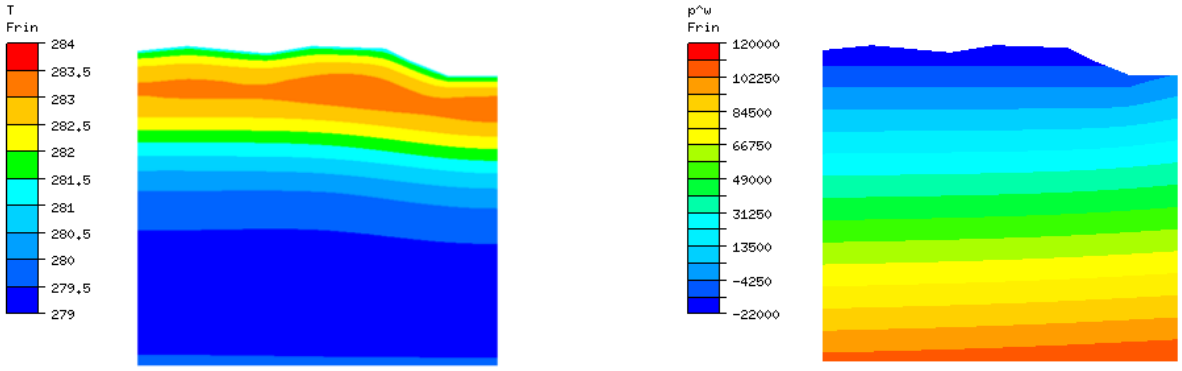

Figure 6.36: Initial temperature and pore pressure for the site near Drammen

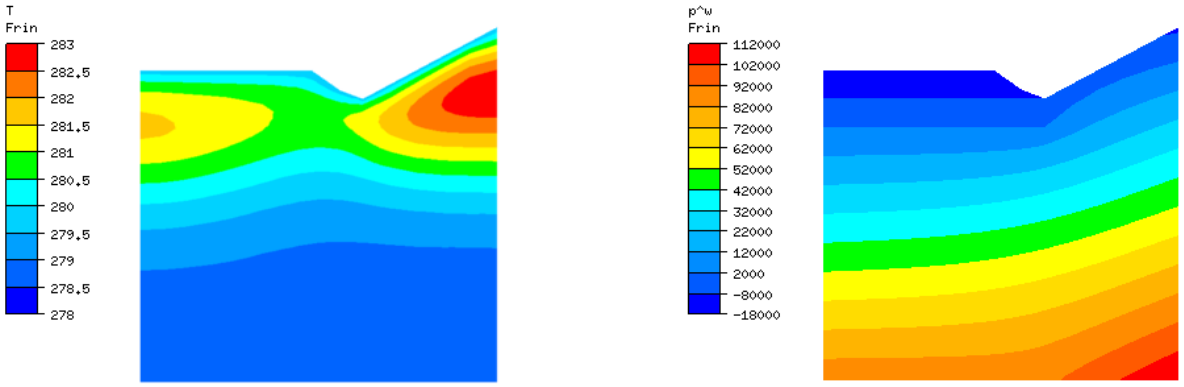

Figure 6.37: Initial temperature and pore pressure for the site near Ås

6.4.6 Results for Drammen

The modelled and measured deformation of the rails are compared in figure 6.39. The temperature measured by the thermistor string is compared to the analysis in figure 6.40. As the temperature is plotted for the closest node, the real and node depth is specified in the legend. The estimated error is plotted in figure 6.41, where the vertical line shows when the time stepping was adjusted. In appendix E, deformation, pore pressure, temperature and ice saturation is shown after 30, 70, 85, 120, 150 and 180 days.

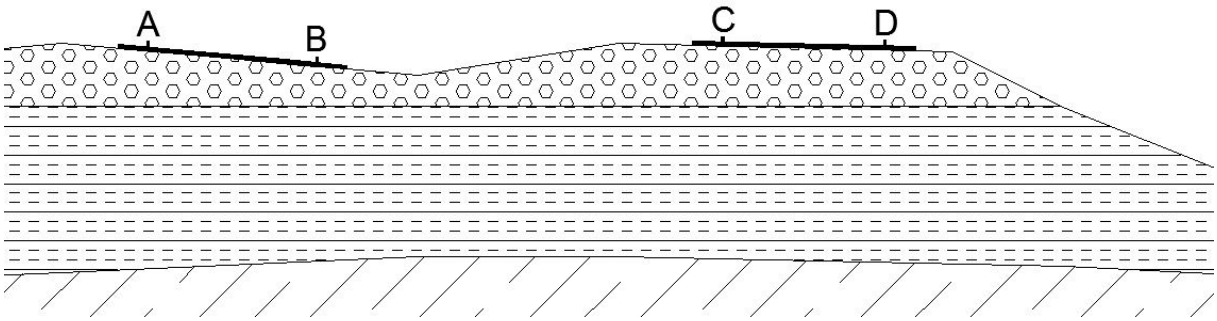

Figure 6.38: Reference for points with measured deformation

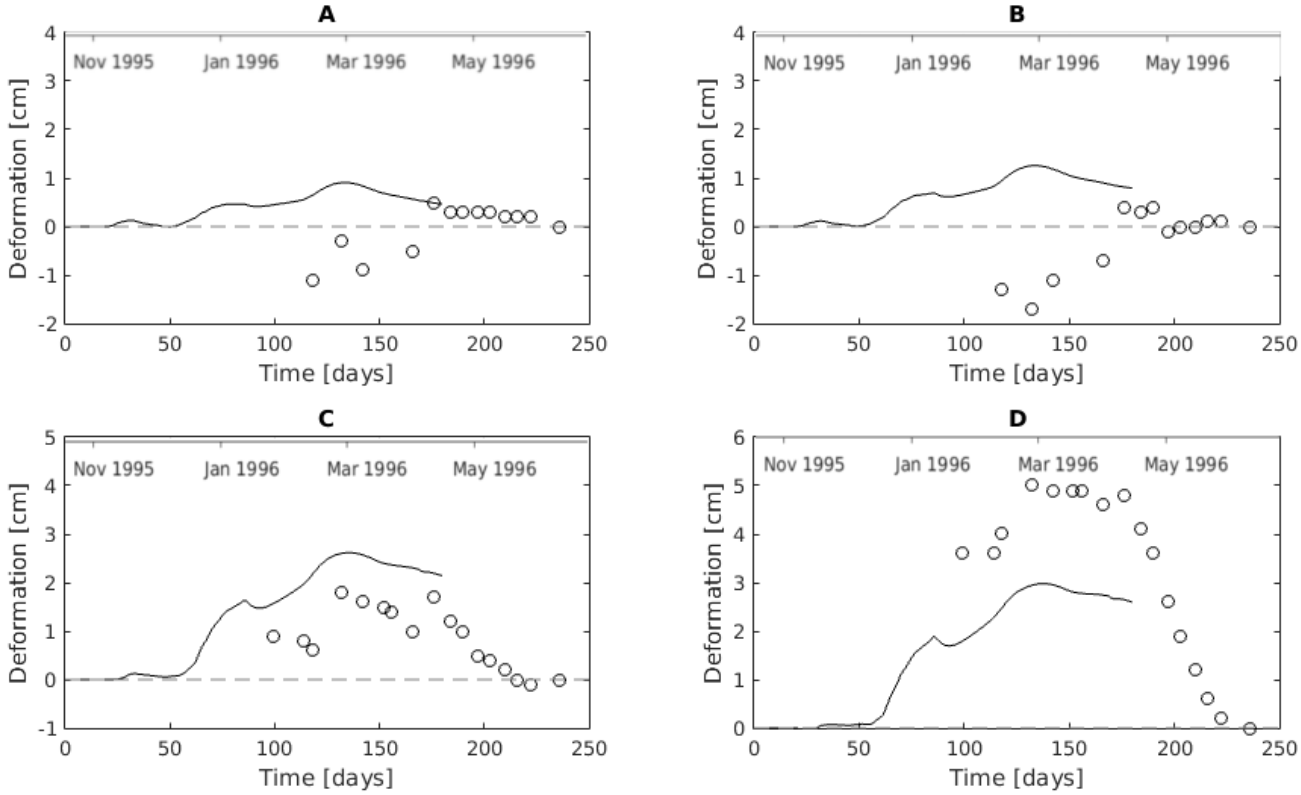

Figure 6.39: Observed and modelled track deformation.

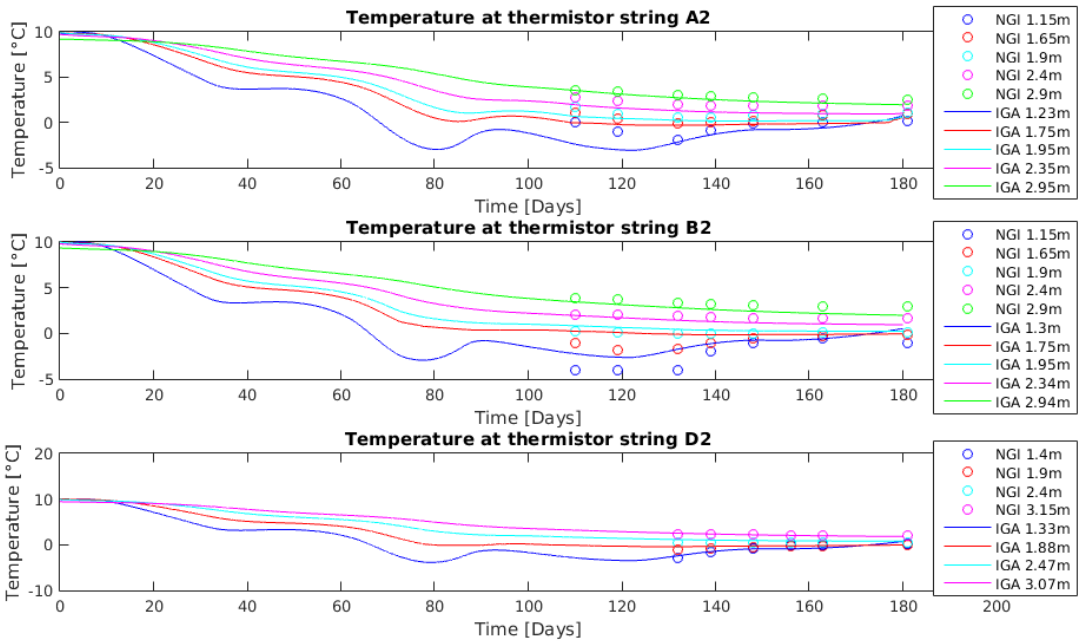

Figure 6.40: Measured and modelled temperature development

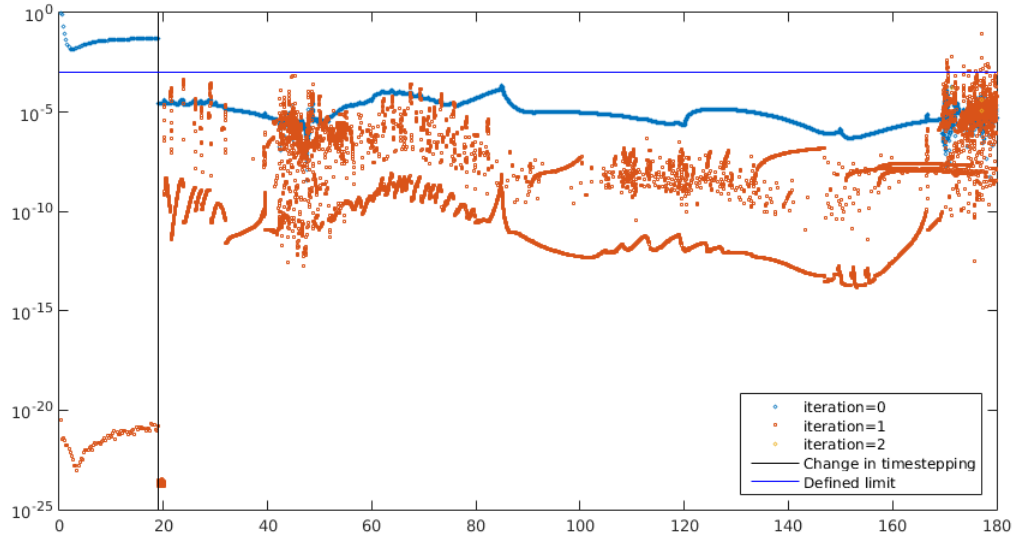

Figure 6.41: Estimated error plotted with time for the sit near Drammen

6.4.7 Results for Ås

The heave of the right track is shown in figure 6.42. The temperature relating to the measured points by NGI, is plotted and compared in figure 6.43. The estimated error is plotted in figure 6.44, where the vertical line shows when the time stepping was adjusted. In appendix E, deformation, pore pressure, temperature and ice saturation is shown after 30, 70, 85, 120, 150 and 180 days.

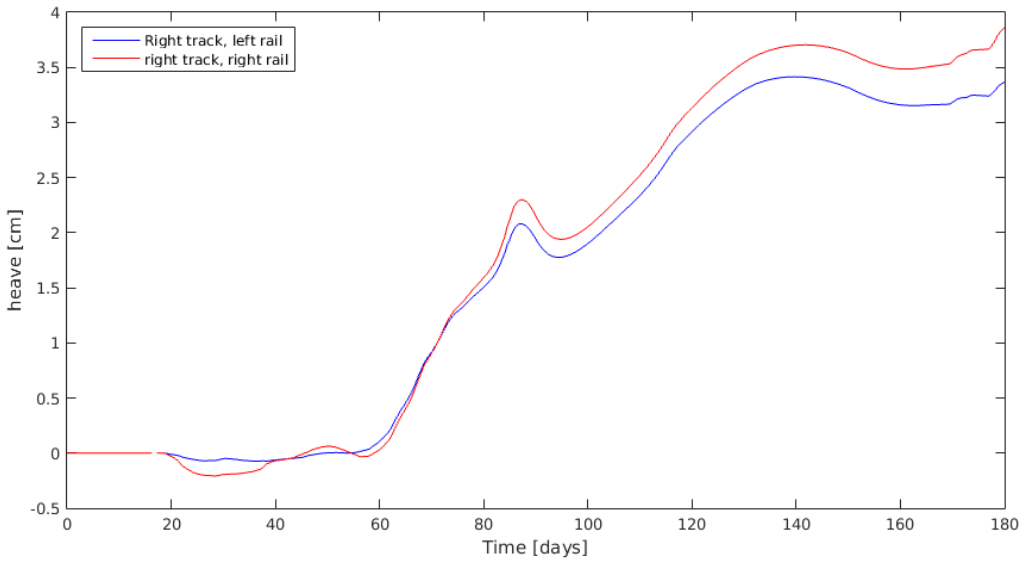

Figure 6.42: Deformation on the right track for the site near Ås

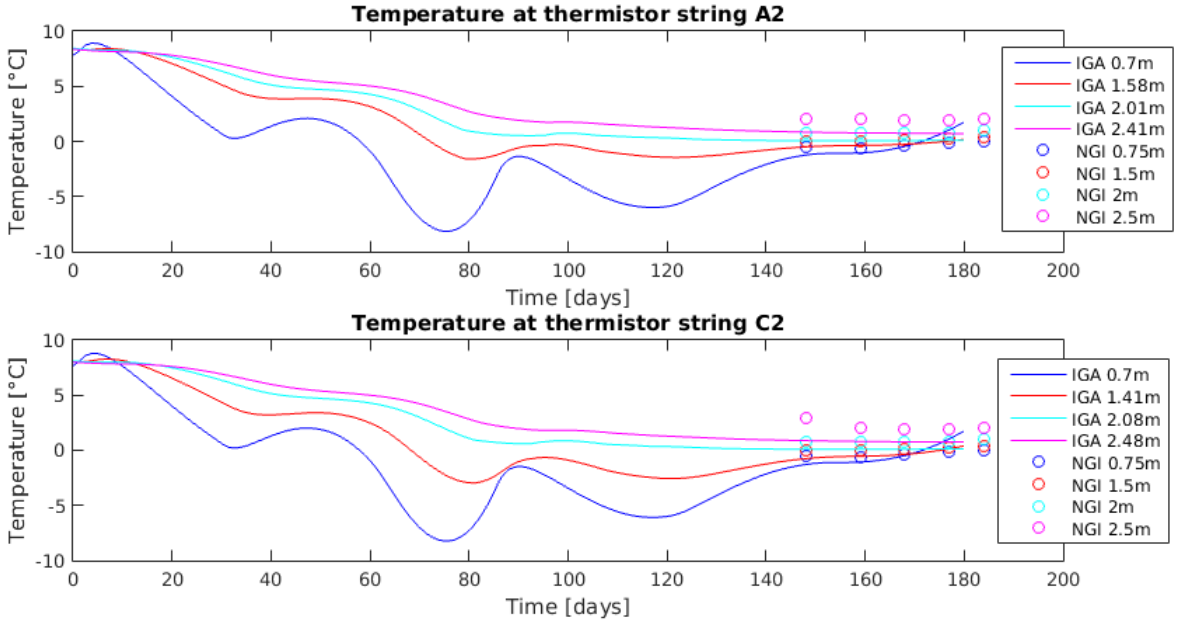

Figure 6.43: Measured and model temperature for the site near Ås

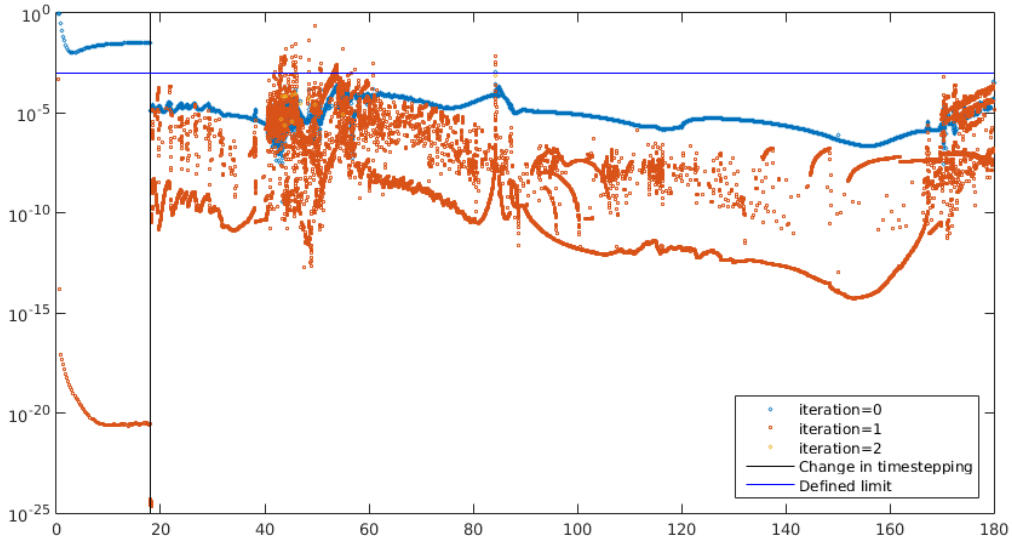

Figure 6.44: Estimated error plotted with time for the sit near Ås

6.4.8 Discussion

Due to long calculation time, the mesh is course, and there is only 2 meters extra soils on each side of the model. A calculation with half the element size mesh and expansion of the sides is assumed to run for approximately two days on the laptop available, and there has not been time to perform this calculation. There is also great uncertainty in the material parameters, and the is no field data on the phase change parameters.

The simulation results show much more heave on the right track, compared to the left track. In reality the right tack is most exposed to heave, but the left track does actually settle during the winter. For the right track, the simulation estimates more heave on the right rail. The same effect is measured om the rail, but the deformation is overestimate for the left rail, and underestimated for the right rail.

Based on the data from the thermistor string, especially the Drammen simulation predicts the temperature well, but also the Ås simulations is comparable with the data. Considering the approximation in heat conductivity, heat capacity, temperature functions and lack of modelled snow cover/wind chill/radiation, the result are relatively good.

It is clear that there is some problems with the model, although some aspects of model gives reasonable results. As with the frost heave cell, the problems may relate to the linear elastic model. As this is expected to be the first winter with considerable heave, there is reasonable to expect plastic strains, which is not detected in the model.

It is also unfortunate that the measurements of deformations starts in February, because the initial reference high of the track must be approximated by the measurement in June 1996. If there has been plastic settlement on the track, the elevation of the the track will not be the same for the summer of 1996 as the summer of 1995. Observing deformations in point D, we can see that the curve would fit much better if the track has experienced approximately 2cm of plastic settlement.

All things considered, the simulations only partially represent reality. It is believed that the solution may greatly benefit from a more advanced material model.

Chapter 7

Conclusion and Recommendations for Further Work

7.1 Isogeometric Analysis of Fully Saturated Porous Media

A total of 4 numerical studies of fully saturated porous medias has been conducted using isogeometric elements and the THM (Thermo-Hydro-Mechanical) model for fully saturated soils. The thermal consolidations example is compared with existing conventional finite element analysis, and is found to yield highly comparable results. Since isogeometric analysis is known to preform well for discontinuities, a total of 3 numerical studies with discontinuities was conducted and compared with existing XFEM (Extended Finite Element Method) calculations. An XFEM calculations relays on replacing the basis functions near a discontinuity. Using isogeometric analysis, *without* altering the basis functions, the results are shown to be comparable with the XFEM calculations. The thesis shows that for the type of problem tested, the fully saturated THM-model with isogeometric elements performers very well for problems with discontinuities.

7.2 The Parameters in the Ground Freezing Model

As expected, the phase change parameters are important in the simulations, but the strength parameter is shown to effect the solutions much more than the permeability parameter. The simulations also show that the heave is greatly effected when applying representative saturation curves for sand, silt and clay. Based on the results, the most important material prop-

erty is probably the stiffness. For a uniform soil with static temperature, the heat conductivity and especially the heat capacity in the normal range, has little effect on the solution. It is important to note that these parameters is more important in more complex calculations, such as the case study. The parametric study also shows that using realistic saturation curves makes the equation system highly non-linear. Of the materials tested, the clay was most prone to diverge. A short summary of the results is presented in table 7.1.

Parameter	Heave	Frost penetration	Ice Saturation	Freezing induced suction
m^p	low	-	-	medium
η	high	-	-	medium
S^α	high	medium	high	medium
S^β	high	medium	high	medium
S^γ	medium	low	high	medium
ρ_s	-	-	-	-
c_s	low	low	-	-
λ_s	medium	high	high	medium
k	medium	-	-	high
E	high	low	low	high
n	medium	high	medium	medium
μ	medium	-	-	high
Saturation curves	high	medium	high	high

Table 7.1: Summary of parametric study, ranging from no (-) to high effect.

7.3 The Frost Heave Cell Simulation

Although the simulations predicts the total heave well, the soft clay experiences plastic deformations. This effect is not captured in the linear elastic model. The frost heave cell simulations shows the limitations in a linearly elastic model, but some aspects are still close to the laboratory results. We know from the parameter study that strength and permeability greatly affect the pore pressure, and hence the effective stresses. The clay tested is soft and has low permeability, so it is reasonable to believe that the clay is difficult to model using a linearly elastic model.

7.4 Simulation of Seasonal Temperature Variation

The simulations shows a large difference in temperature development during the winter period, when simulating with and without latent heat. At the onset of winter, the two simula-

tions gives relatively similar result. This is important for large models, since the error from establishing the initial temperature without the phase change equations are limited. The simulations also show that when applying a sinus temperature function, the temperature profiles are close to the steady state solutions after only 2-3 years for the material used in the simulations. It is also clear from the calculations that the most difficult period to calculate is during the thawing phase. The temperature profiles are also highly comparable with the analytical solution.

7.5 Application of the THM-model in infrastructure projects

As with the frost heave cell, the real case simulations is limited by the linearly elastic material model. Despite the simple material model, the simulations do recreate some aspects of the case. The simulation illustrates the limitation in current model, but also shows the possibilities with further research.

7.6 Recommendations for Further Work

The linear elastic material model does seam to greatly limit the model. Expanding the model to more complex stress-strain relations may improve the model with respect to settlements similar to what observed in the frost cell and case study.

There is at the moment limited comparable laboratory data adjusted for the model. An investigation into the relationship between the different phase change parameter, can greatly reduce the uncertainty in the model parameters. For the model to be used, there also exist a need for specialised ground investigations. It is possible to determine the saturation curve, strength parameter and permeability parameter separately, or combined in a frost heave cell (as shown in this thesis).

The model does seam to have some difference in divergent properties, using different saturation curve parameters to estimate the same saturation curve. This might relate to the derivative of the saturation curves very close to zero, but there might be other factors creating this problem. It is regardless important to be able to pick a set of parameters with good convergence properties.

The model creates two sets (basis) of splines, where deformation is one polynomial degree higher than pore pressure and temperature. At the moment it is only possible to en-

force Neumann boundary conditions on a basis level for pore pressure and temperature. It is hence not possible to separate the thermal and water flux on a boundary, creating the problem observed in the fully coupled discontinuity model. The model should be able to apply the boundary condition on the component level, such as for a Dirichlet boundary.

A updated version of IFEM does support the possibility for automatic cut-back time stepping. It is then possible to set a limit for maximum and minimum time step size, IFEM will automatically adjust the time stepping and reset with a smaller step if the solution diverges. Implementing this feature in code will greatly ease the use of the program, and reduce the calculation time.

The integration scheme is hard coded to the backward Euler method. Although there are reasons to choose the backwards Euler, such as the critical time step (explained in: Vermeer and Verruijt (1981)), it is interesting, at least for research purposes to be able to adjust the integration scheme.

At the time of writing, it is possible to model snow or wind chill with Neumann boundary condition, using a representative constant temperature and heat conductivity. As snow cover and temperature vary through the year, it is of interest to allow temperature and heat conductivity to be treated as a function of time.

Bibliography

Aboustit, B., Advani, S., and Lee, J. (1985). Variational Principles and Finite Element Simulations for Thermo-Elastic Consolidation. *International journal for numerical and analytical methods in geomechanics*, 9(1):49–69.

Alonso, E. E., Gens, A., Josa, A., et al. (1990). Constitutive Model for Partially Saturated Soils. *Géotechnique*, 40(3):405–430.

Andersland, O. B. and Ladanyi, B. (2004). *Frozen Ground Engineering*. John Wiley & Sons.

Arts, R., Chadwick, A., Eiken, O., Thibeau, S., and Nooner, S. (2008). Ten Years' Experience of Monitoring CO_2 Injection in the Utsira Sand at Sleipner, Offshore Norway. *First break*, 26(1).

Bekele, Y., Kyokawa, H., Kvarving, A., Kvamsdal, T., and Nordal, S. (2016). Isogeometric Analysis of THM Coupled Processes in Ground Freezing. *Draft, planned published 2016/1017*.

Bell, K. (2013). *An Engineering Approach to Finite Element Analysis of Linear Structural Mechanics Problems*. Akademika Publ., Trondheim.

Borden, M. J., Scott, M. A., Evans, J. A., and Hughes, T. J. (2011). Isogeometric Finite Element Data Structures Based on Bézier Extraction of NURBS. *International Journal for Numerical Methods in Engineering*, 87(1-5):15–47.

Cottrell, J. A., Hughes, T. J., and Bazilevs, Y. (2009). *Isogeometric Analysis: Toward Integration of CAD and FEA*. John Wiley and Sons.

Emdal, A. (2013). Introduksjon til Geoteknikk.

Energy.gov (2016). Cited 23/02-16. http://energy.gov/eere/articles/geothermal-energy-glance-back-and-leap-forward.

Khoei, A., Moallemi, S., and Haghighat, E. (2012). Thermo-Hydro-Mechanical Modeling of Impermeable Discontinuity in Saturated Porous Media with X-FEM Technique. *Engineering Fracture Mechanics*, 96:701–723.

Konrad, J.-M. (1980). *Frost Heave Mechanics*.

Konrad, J.-M. and Seto, J. (1994). Frost Heave Characteristics of Undisturbed Sensitive Champlain Sea Clay. *Canadian Geotechnical Journal*, 31(2):285–298.

Lewis, R. and Schrefler, B. (1998). The Finite Element Method in the Static and Dynamic Deformation and Consolidation of Porous Media. *Meccanica*, 34(3):231–232.

NGI (1996). NSB Bane. Hovedkontoret Telehiv Vinteren 95/96. Report 960060-1, Lars Andresen.

NGI (2004). Drammen Kommune Stillerud. Data Report 20041131-1, Arne Kleven.

Nishimura, S., Gens, A., Olivella, S., and Jardine, R. (2009). THM-Coupled Finite Element Analysis of Frozen Soil: Formulation and Application. *Geotechnique*, 59(3):159.

continuummechanics.org (2016). cited 01/04-16. http://www.continuummechanics.org/cm/materialderivative.html.

eklima.met.no (2016). cited april/may-16. http://www.eklima.met.no.

Ingeniør Chr. F. Grøner AS (1979). Kloakkledning Hoxtvedt-Tveter. Report UB.110110, Amund Mowinkel-Amundsen.

Norwegian Road department (2012). Telehiv på nye norske veger,- hvorfor, og hva kan gjøres for å unngå dette?

NSB Engineeringavdeling (1988). Dobbeltsporanlegget Ski-Moss. Data Report UB.112212.

NSB Engineeringavdeling (1989). Dobbeltsporanlegget Ski-Moss. Data Report UB.112228.

NTNU Geotechnical Division (2014). Geotechnics Field and Laboratory Investigations.

Simmakers.com (2016). cited 23/02-16. http://simmakers.com/ground-freezing-in-tunnel.

Underground-energy.com (2016). cited 23/02-16. http://www.underground-energy.com/BTES.html.

Smith, M. and Tice, A. (1988). Measurement of the Unfrozen Water Content of Soils: a Comparison of NMR and TDR Methods. In *Proceedings of the 5th International Conference on Permafrost, Trondheim, Norway*, pages 473–477.

Vermeer, P. and Verruijt, A. (1981). An Accuracy Condition for Consolidation by Finite Elements. *International Journal for numerical and analytical methods in geomechanics*, 5(1):1–14.

Verruijt, A. (2014). Theory and Problems of Poroelasticity. *Delft University of Technology*.

Zhu, Y. and Carbee, D. L. (1984). Uniaxial Compressive Strength of Frozen Silt under Constant Deformation Rates. *Cold Regions Science and Technology*, 9(1):3–15.

Appendix A

Acronyms

B-Splines Benzier-splines

CAD Computer Aided Design

CPTu Cone Penetration Test with pore pressure(u) measurement

FEA Finite Element Analysis

FEM Finite Element Method

IGA IsoGoemetric Analysis

NURBS Non-Uniform Rational B-Splines

THM Thermo-Hydro-Mechanical

XFEM Extended Finite Element Method

Appendix B

Symbols

α Biot's coefficient

β Volumetric thermal expansion coefficient

β_{sw} Combined volumetric thermal expansion coefficient

χ Thermal conductivity

χ_{eff} Combined thermal conductivity

ϵ Total strain

ϵ_0 Initial strain

ϵ^T Temperature strain

η Strength model parameter

Γ Boundary in FEA

γ Unit weight

$\hat{S}$ Storativity

ν Poisson's ratio

Ω Element area/volume

ρ Density

ρ_i Ice density

ρ_s Solid density

ρ_w Water density

σ Total stress

σ' Effective stress

θ Integration scheme

Θ Knot vector

ξ Knots

C Heat capacity

c Specific heat capacity

C_p Control points in mesh/Similar to nodes

D_e Linear stiffness

D_T Non-linear stiffness

E Young's module

g Gravity(9.81m/s)

k Hydraulic conductivity

K_0 Bulk module of medium

K_f Bulk module of water

K_s Bulk module of solid

L_f Latent heat of fusion

m mass

m^p Permeability model parameter

n porosity

p Pore pressure

p^i Pore ice pressure

p^w Pore water pressure

q Water flow

q_F Heat flow

S_i Ice saturation

S_p Isothermal water capacity

S_T Non-isothermal water capacity

S_w Water saturation

S^α Saturation model parameter 1

S^β Saturation model parameter 2

S^γ Saturation model parameter 3

T Temperature

t Time

T_0 Freezing point(273.15 K)

u Deformation

v Velocity of water

w Velocity of solids

Appendix C

Frost Heave Cell

A schematic of the frost heave cell used in Konrad and Seto (1994) is shown in this appendix.

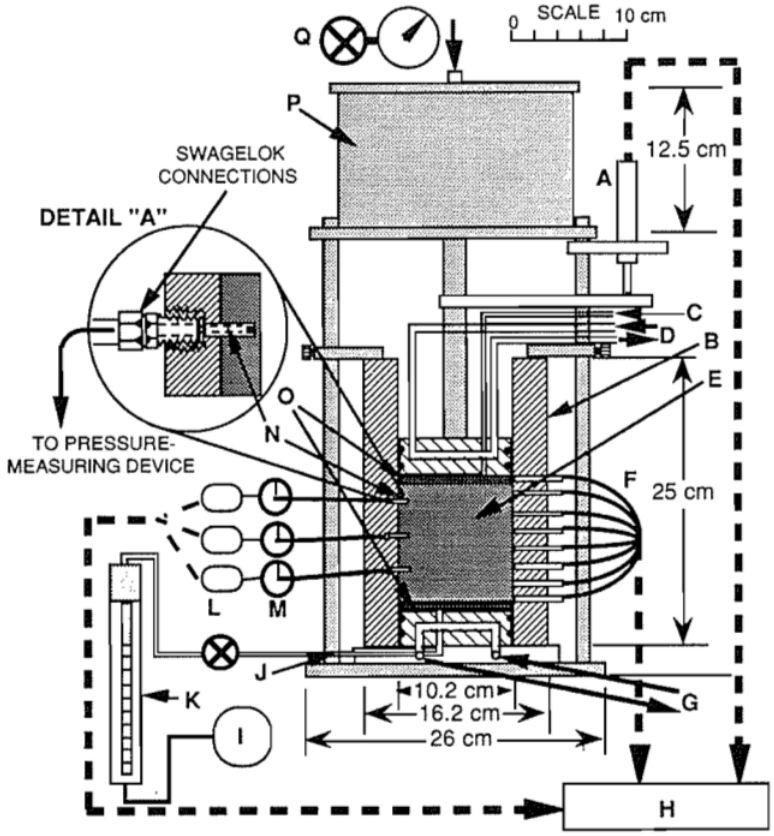

FIG. 3. Schematic diagram of frost heave cell. A, DCDT; B, PVC freezing cell; C, water outlet (top); D, cooling fluid (top); E, soil sample; F, thermistors; G, cooling fluid (bottom); H, data-acquisition system; I, mercury manometer; J, water outlet pressure system (bottom); K, volume-change indicator; L, pressure transducers; M, three-way valves; N, porous tips; O, porous plates; P, bellofram loading system; Q, air pressure gauge.

Figure C.1: Set up for the frost heave cell test calculated in the thesis

Appendix D

CPTu Interpretation

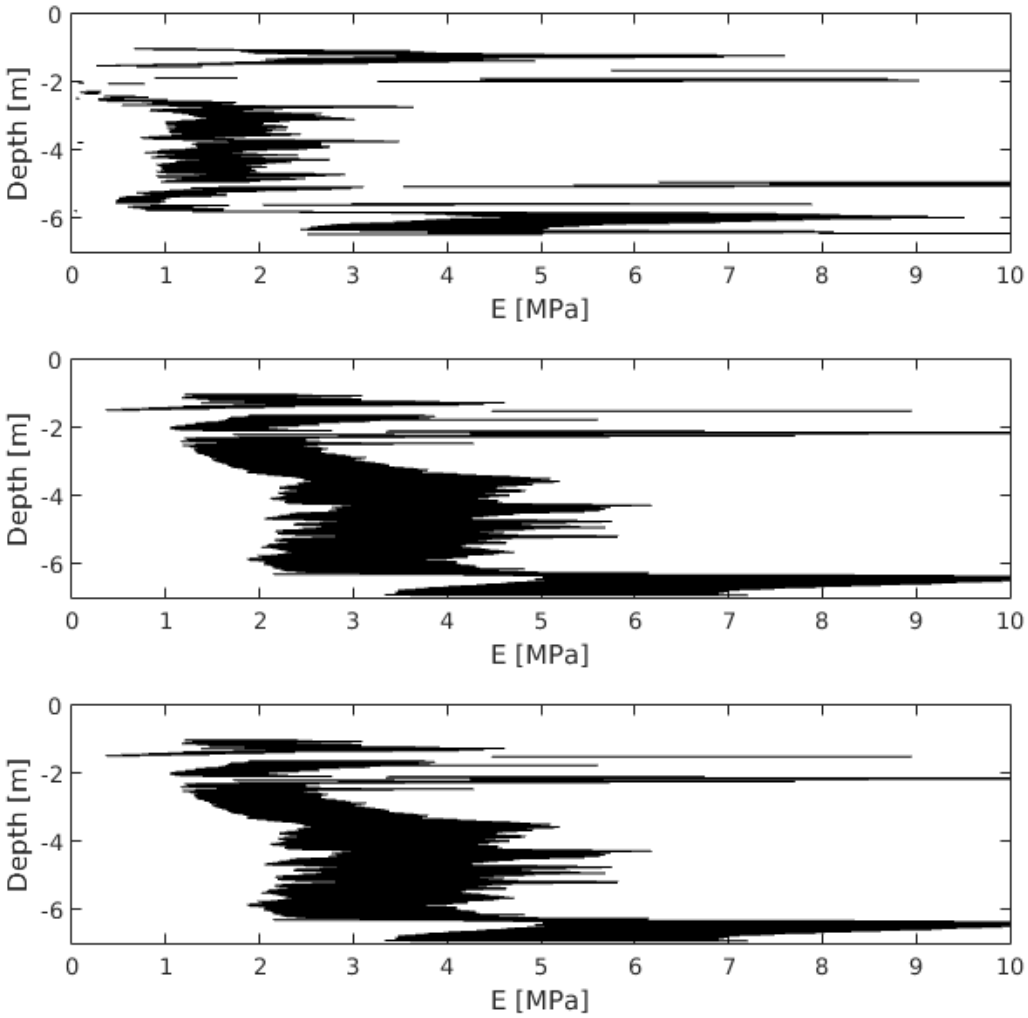

Figure D.1: Young's modulus from CPTU(μ=1/3)

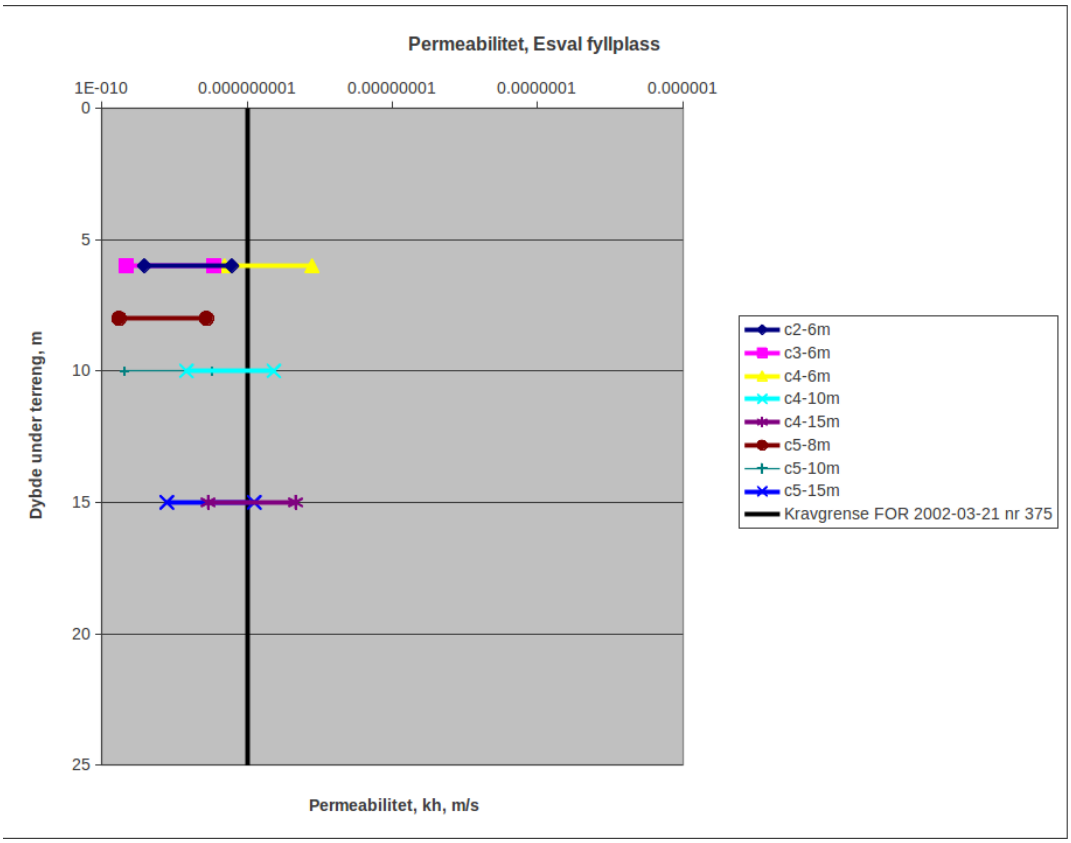

Figure D.2: Results from dissipation test

The CPT data is collected from NGI (2004), located close to the site near Drammen. The stiffness is interpreted as in NTNU Geotechnical Division (2014), and assuming μ=1/3. The shaded area represent the upper and lower approximation. The dissipation results is taken directly from the report.

Appendix E

Case Results

A selections of results from the case study is extracted from GLview, and shown in this appendix. Deformation is plotted in meters, pore pressure is plotted in Pascal, temperature is plotted in Kelvin and ice saturation is dimensionless.

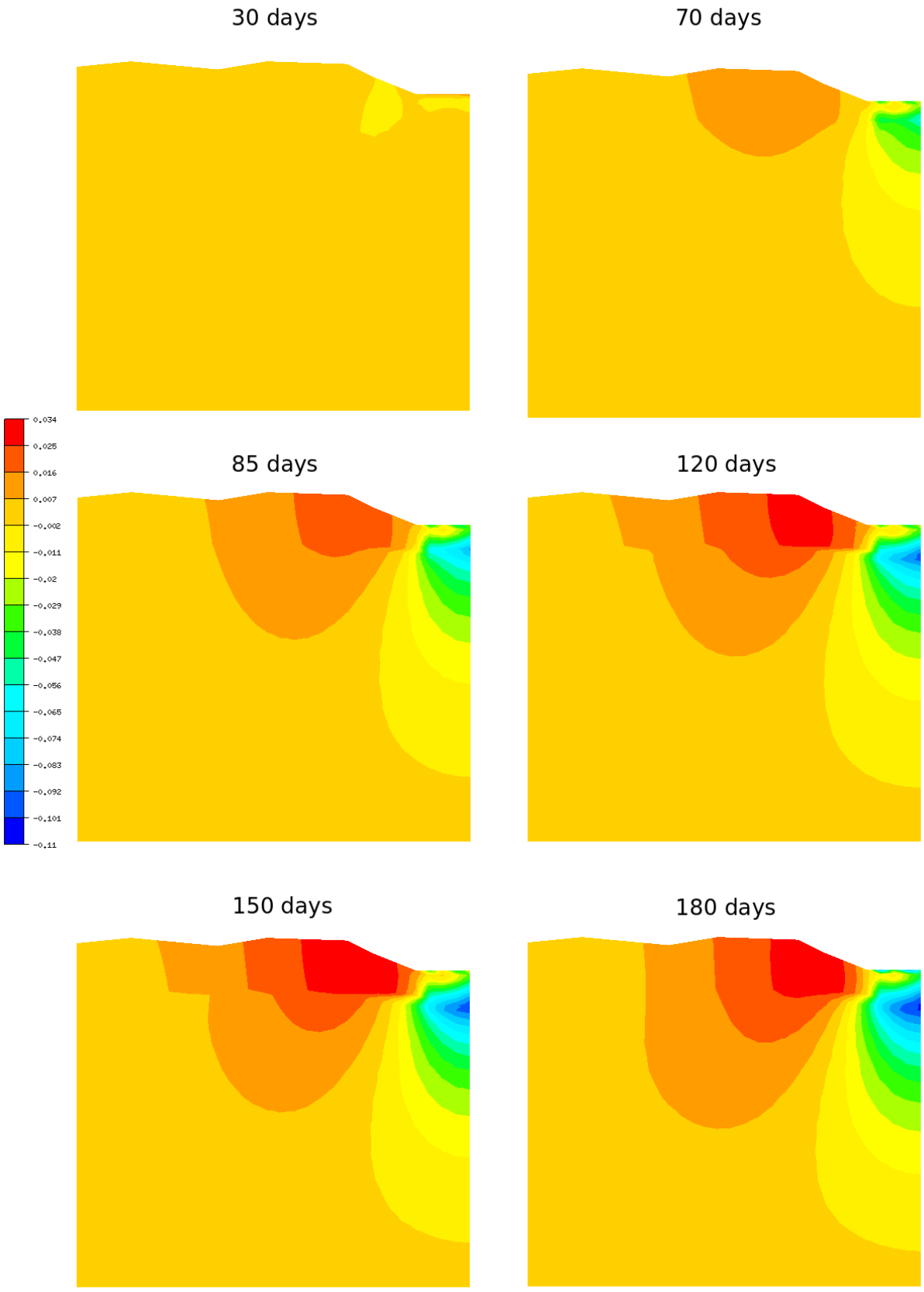

Figure E.1: Deformation in meters for the site near Drammen

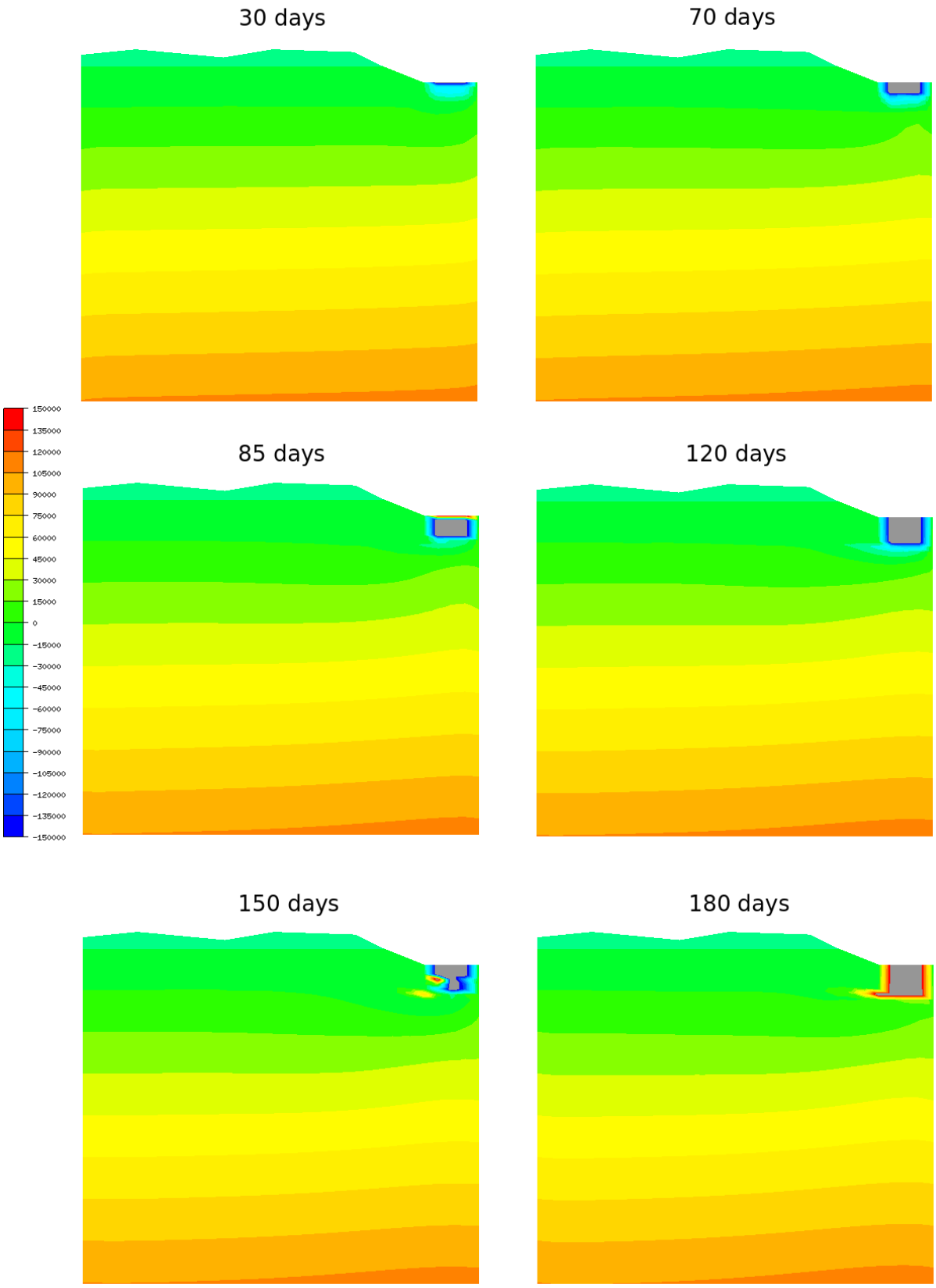

Figure E.2: Pore pressure in Pascal for the site near Drammen. For better visibility, pore pressure is only shown in the area -150kPa to 150kPa. Pore pressure outside this area is gray.

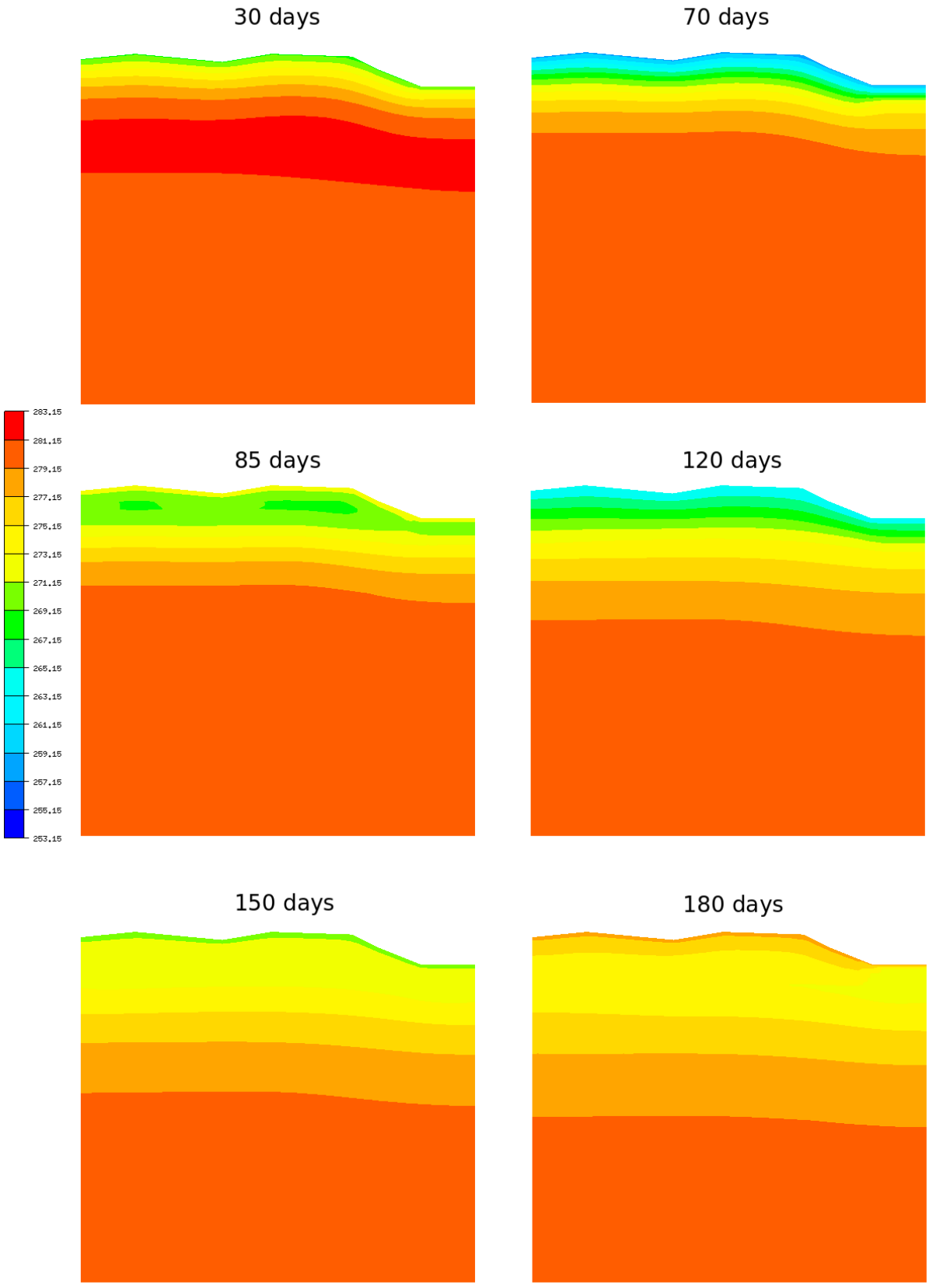

Figure E.3: Temperature in Kelvin for the site near Drammen. 0°C is 273.15K

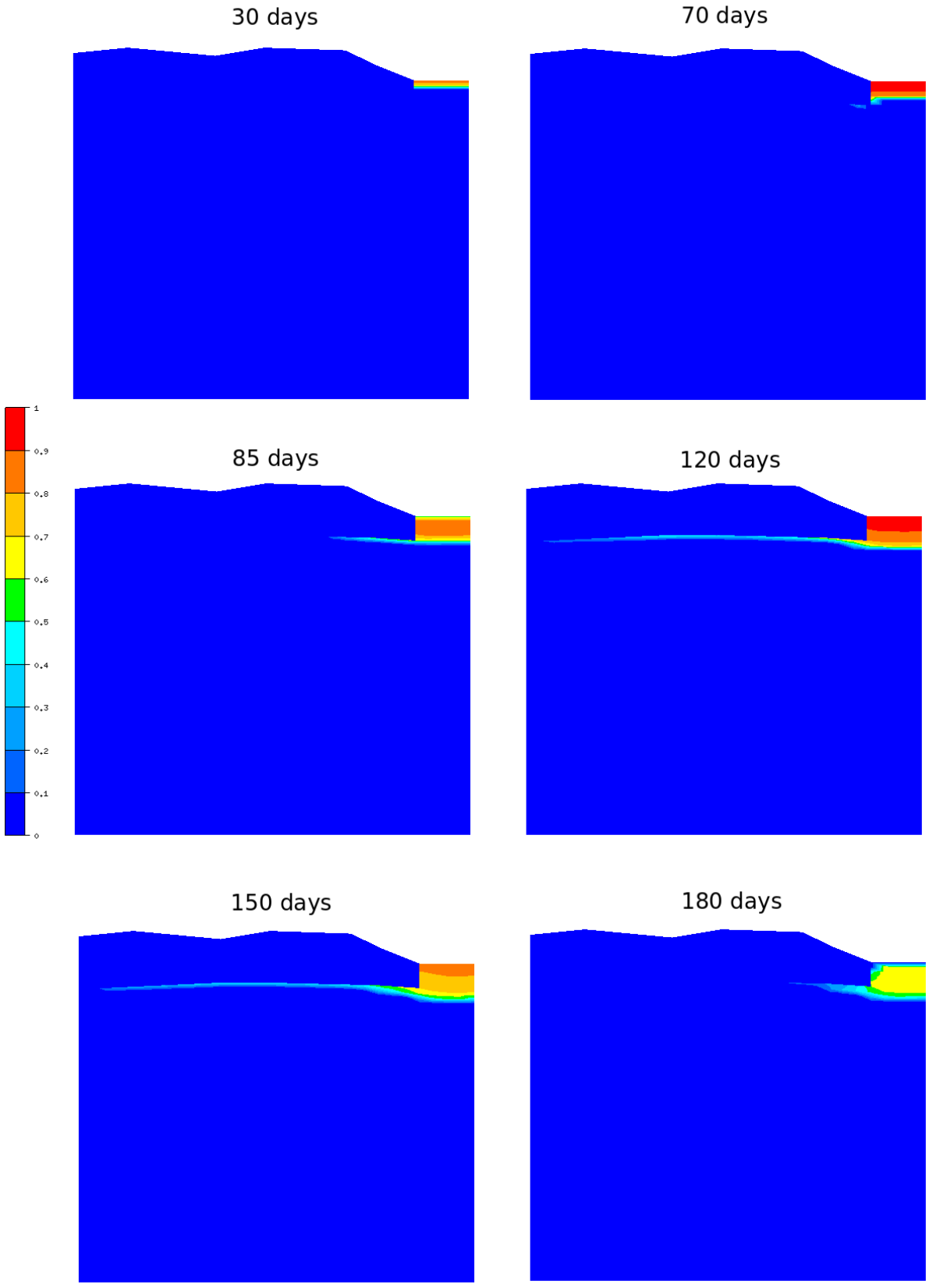

Figure E.4: Ice saturation for the site near Drammen

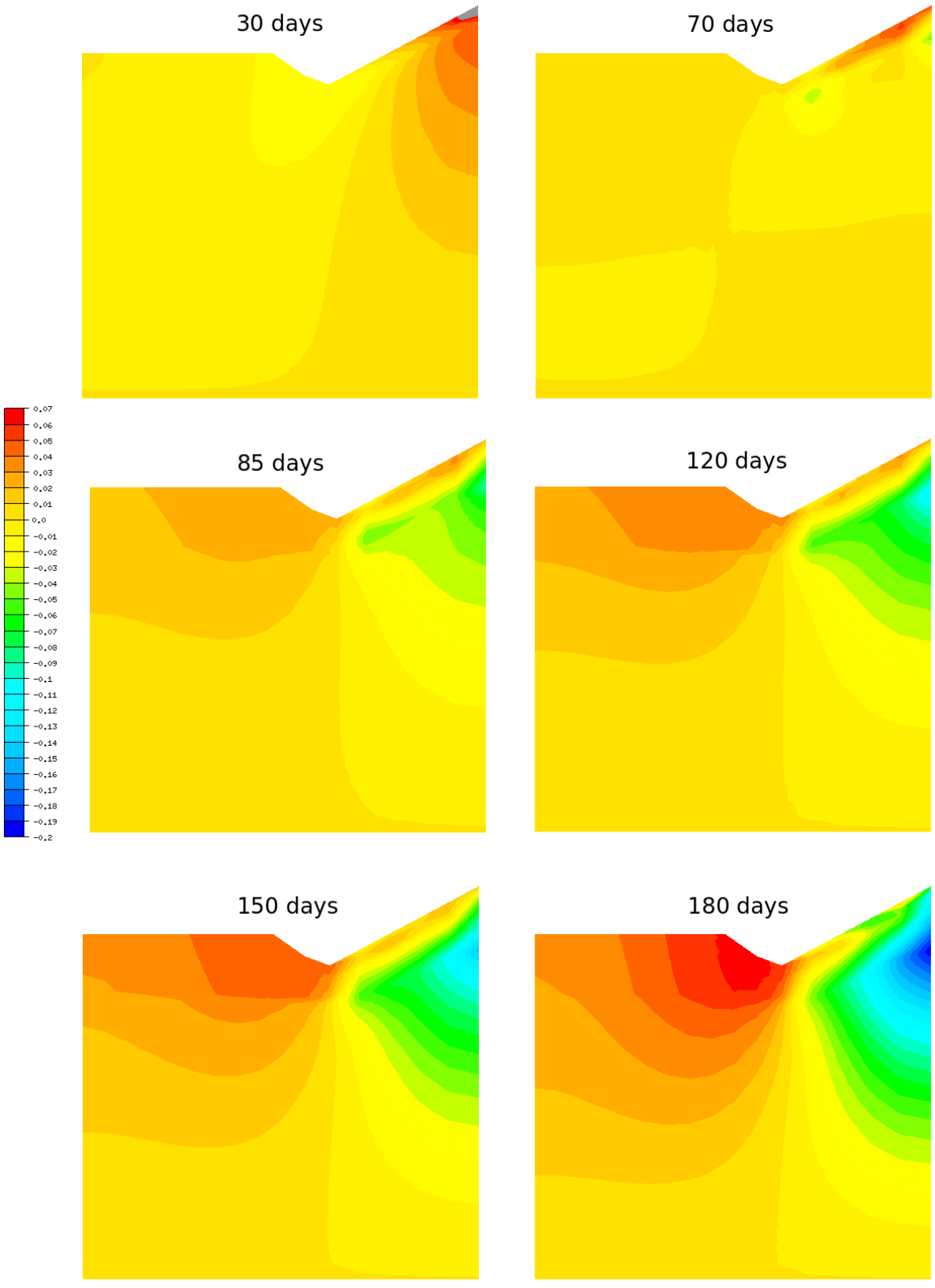

Figure E.5: Deformation in meters for the site near Ås

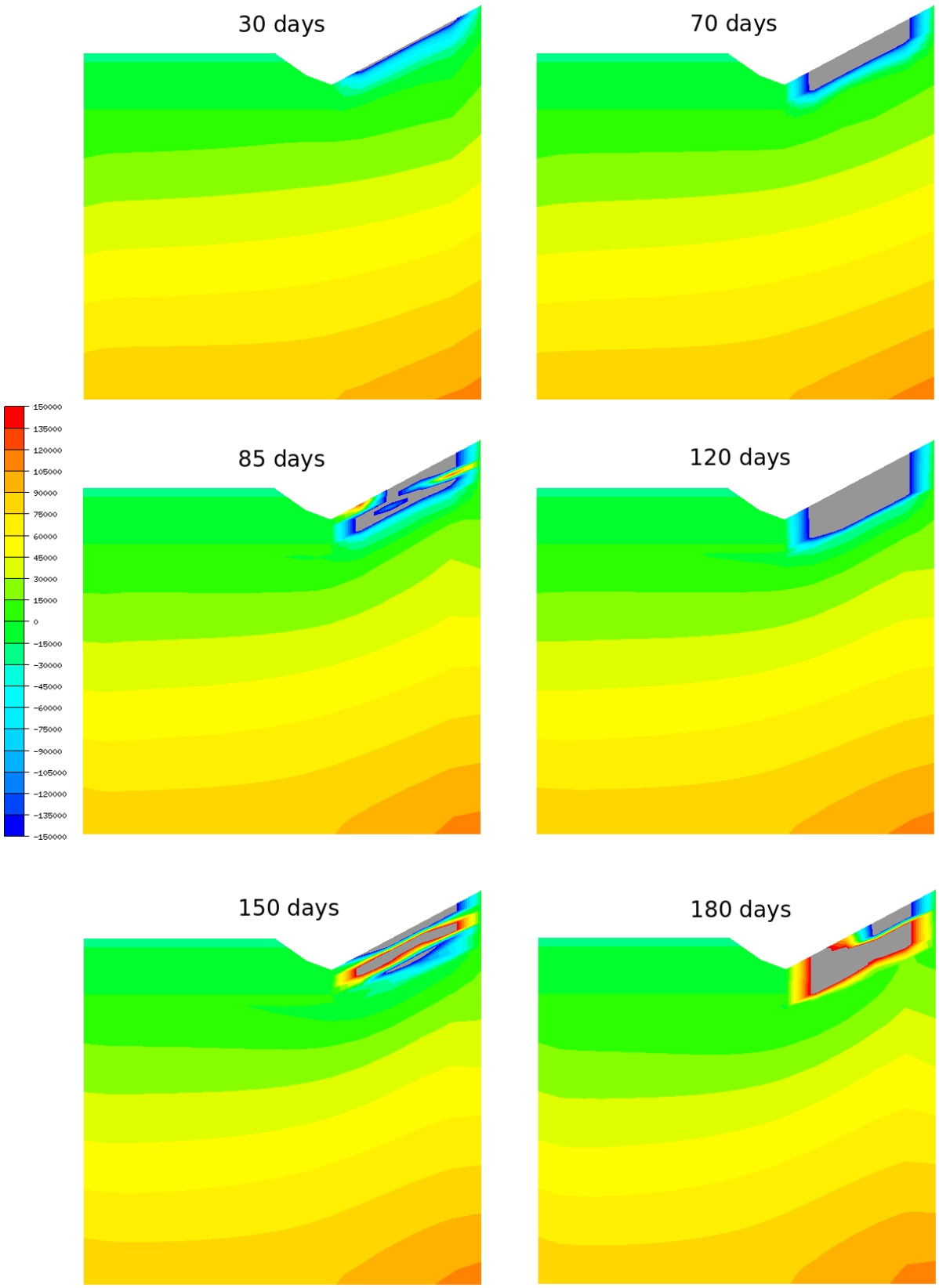

Figure E.6: Pore pressure in Pascal for the site near Ås. For better visibility, pore pressure is only shown in the area -150kPa to 150kPa. Pore pressure outside this area is gray.

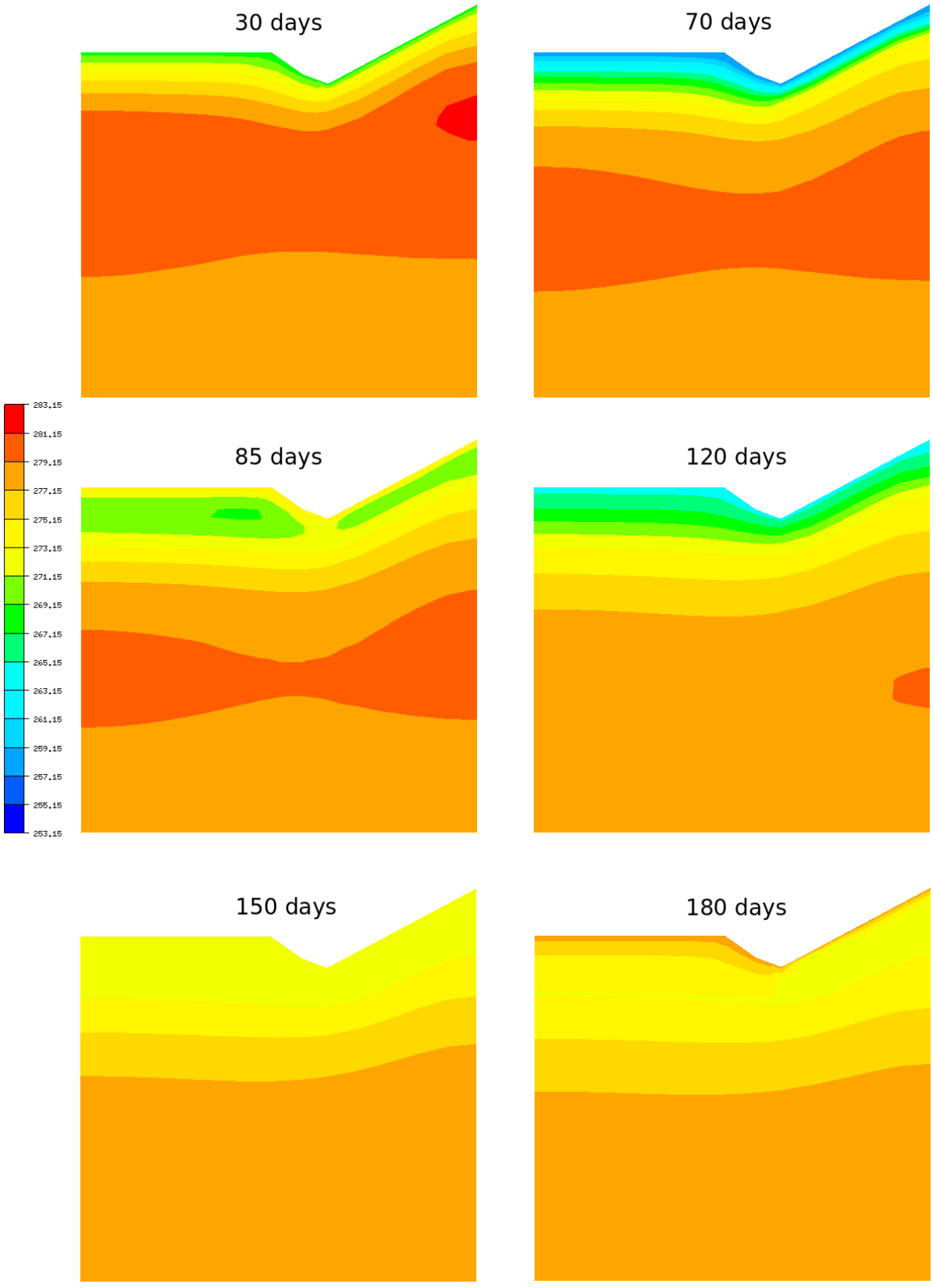

Figure E.7: Temperature in Kelvin for the site near Ås. 0°C is 273.15K

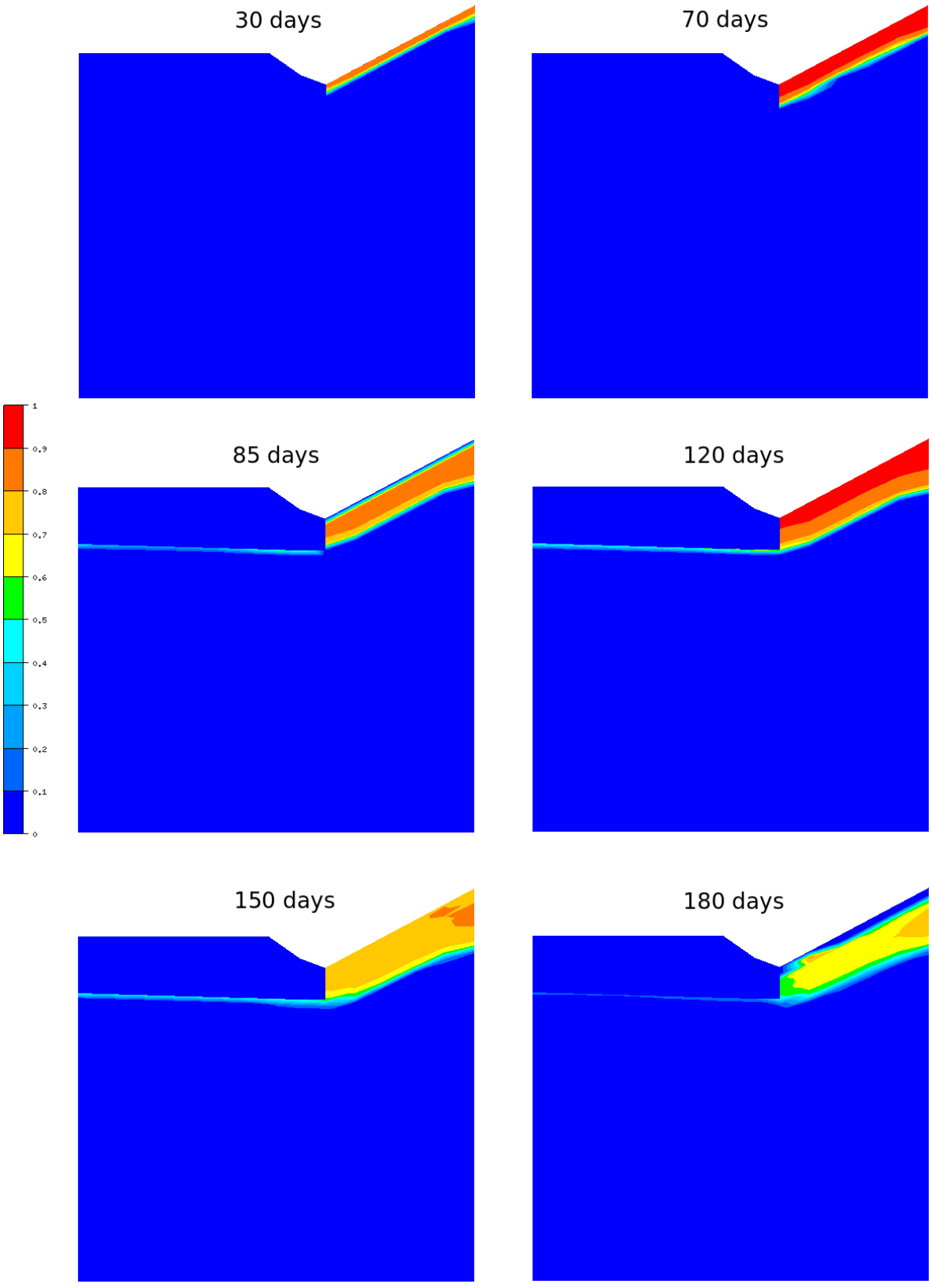

Figure E.8: Ice saturation for the site near Ås

Appendix F

Example set up: Ås

```
<?xml version="1.0" encoding="UTF-8" standalone="yes"?>
<simulation>
  <geometry>
    <patchfile type="bsplines">ASgeometry.g2</patchfile>
    <topology>
      <connection master="2" medge="2" slave="3" sedge="1"/>
      <connection master="2" medge="3" slave="4" sedge="4"/>
      <connection master="2" medge="4" slave="1" sedge="3"/>
      <connection master="5" medge="1" slave="4" sedge="2"/>
      <connection master="5" medge="2" slave="6" sedge="1"/>
      <connection master="5" medge="4" slave="3" sedge="3"/>
      <connection master="7" medge="1" slave="3" sedge="2"/>
      <connection master="7" medge="3" slave="6" sedge="4"/>
    </topology>
    <topologysets>
      <set name="Ballast" type="face">
      <item patch="1"/>
      </set>
      <set name="Frost" type="face">
      <item patch="2"/>
      <item patch="3"/>
      </set>
      <set name="Silt" type="face">
      <item patch="4"/>
      <item patch="5"/>
      <item patch="6"/>
      <item patch="7"/>
      </set>
      <set name="Left" type="edge">
      <item patch="1">1</item>
      <item patch="2">1</item>
      <item patch="4">1</item>
      </set>
      <set name="Bottom" type="edge">
```

```
      <item patch="4">3</item>
      <item patch="5">3</item>
      <item patch="6">3</item>
      </set>
      <set name="Top" type="edge">
      <item patch="1">4</item>
      <item patch="1">2</item>
      <item patch="3">4</item>
      <item patch="7">4</item>
      </set>
      <set name="Right" type="edge">
      <item patch="6">2</item>
      <item patch="7">2</item>
      </set>
      </topologysets>
    </geometry>

  <boundaryconditions>
    <dirichlet set="Left" basis="1" comp="1"/>
    <dirichlet set="Bottom" basis="1" comp="2"/>
    <dirichlet set="Bottom" basis="1" comp="1"/>
    <dirichlet set="Right" basis="1" comp="1"/>
    <dirichlet set="Right" basis="2" comp="1" type="expression">9810*(71.4−y)</dirichlet>
    <dirichlet set="Left" basis="2" comp="1" type="expression">9810*(69.1−y)</dirichlet>
    <dirichlet set="Bottom" basis="2" comp="2">278.681</dirichlet>
    <dirichlet set="Top" basis="2" comp="2" type="expression">if(below(t,2592000),0.00904*(t/86400)^2−0.8528*(t/86400)+12.49+273.15,
                                    if(below(t,5184000),−0.03268*(t/86400−30)^2+0.8864*(t/86400−30)−4.96+273.15,
                                    if(below(t,7344000),0.07953*(t/86400−60)^2−1.601*(t/86400−60)−7.782+273.15,
                                    if(below(t,10368000),0.0165*(t/86400−85)^2−0.8830*(t/86400−85)+1.909+273.15,
                                    if(below(t,12960000),−0.009362*(t/86400−120)^2+0.5263*(t/86400−120)−8.7783+273.15,
                                    if(below(t,15552000),0.009771*(t/86400−150)^2−0.08217*(t/86400−150)−1.417+273.15,4.912+273.15))))))</dirichlet>
  </boundaryconditions>

<thmcouplednl>
    <materialdata set="Silt" rhos="2650.0" rhow="1000.0" rhoi="910.0"
                  cs="750.0" cw="4190.0" ci="2095.0"
                  lambdas="3" lambdaw="0.6" lambdai="2.2"
                  Lf="334000.0" poro="0.44"
                  perm="1.0e−9 1.0e−9 0.0" mk="0.4"
                  Es="1.0e6" Ei="9.1e9" nus="0.3" nui="0.4" eta="3"
                  alpha="5e−6" beta="1" gamma=".7"
                  Tf="273.15"/>
    <materialdata set="Ballast" rhos="2000.0" rhow="1000.0" rhoi="910.0"
                  cs="920.0" cw="4190.0" ci="2095.0"
                  lambdas="1.5" lambdaw="0.6" lambdai="2.2"
                  Lf="334000.0" poro="0"
                  perm="1.0e−1 1.0e−1 0.0" mk="0.4"
                  Es="15e6" Ei="9.1e9" nus="0.2" nui="0.4" eta="2"
                  alpha="5e−6" beta="1" gamma=".7"
```

```
                Tf="200.15"/>
    <materialdata set="Frost" rhos="2000.0" rhow="1000.0" rhoi="910.0"
                cs="920.0" cw="4190.0" ci="2095.0"
                lambdas="1.45" lambdaw="0.6" lambdai="2.2"
                Lf="334000.0" poro="0"
                perm="1.0e-1 1.0e-1 0.0" mk="0.4"
                Es="15e6" Ei="9.1e9" nus="0.2" nui="0.4" eta="2"
                alpha="5e-6" beta="1" gamma=".7"
                Tf="200.15"/>
    <gravity>0.0 -9.81 0.0</gravity>
    <initialcondition field="vector" level="0" file="ASinitial"
                file_level="365" file_field="sig_xy" basis="2" component="1"/>
    <initialcondition field="vector" level="0" file="ASinitial"
                file_level="365" file_field="sig_xy" basis="2" component="2"/>
    <nonlinearsolver>
      <maxits>50</maxits>
      <rtol>5.0e-3</rtol>
    </nonlinearsolver>
    <scaling scl1="1.0e0" scl2="1.0e0"/>
  </thmcouplednl>

  <timestepping>
    <step start="0" end="1555200">72</step>
    <step start="1555200" end="15552000">30000</step>
  </timestepping>

</simulation>
```